NATIONAL TECHNICAL UNIVERSITY OF ATHENS
SCHOOL OF NAVAL ARCHITECTURE & MARINE ENGINEERING
DIVISION OF MARINE ENGINEERING

# DIPLOMA THESIS

# Computational and experimental study of journal bearings

KONTARAS GEORGIOS NEKTARIOS

**Thesis Committee:**

| | |
|---|---|
| **Supervisor:** | **C.I. Papadopoulos, Assistant Professor NTUA** |
| **Members:** | **L. Kaiktsis, Associate Professor NTUA** |
| | **G. Papalambrou, Assistant Professor NTUA** |

**Athens, February 2016**

**ΕΘΝΙΚΟ ΜΕΤΣΟΒΙΟ ΠΟΛΥΤΕΧΝΕΙΟ**
**ΣΧΟΛΗ ΝΑΥΠΗΓΩΝ ΜΗΧΑΝΟΛΟΓΩΝ ΜΗΧΑΝΙΚΩΝ**
**ΤΟΜΕΑΣ ΝΑΥΤΙΚΗΣ ΜΗΧΑΝΟΛΟΓΙΑΣ**

# ΔΙΠΛΩΜΑΤΙΚΗ ΕΡΓΑΣΙΑ

# Υπολογιστική και πειραματική μελέτη ακτινικών εδράνων ολίσθησης

**ΚΟΝΤΑΡΑΣ ΓΕΩΡΓΙΟΣ ΝΕΚΤΑΡΙΟΣ**

**Εξεταστική επιτροπή:**

| | |
|---|---|
| **Επιβλέπων:** | **Χ.Ι. Παπαδόπουλος, Επίκουρος Καθηγητής ΕΜΠ** |
| **Μέλη:** | **Λ. Καϊκτσής, Αναπληρωτής Καθηγητής ΕΜΠ** |
| | **Γ. Παπαλάμπρου, Επίκουρος Καθηγητής ΕΜΠ** |

**Αθήνα, Φεβρουάριος 2016**

# Table of Contents

## Acknowledgements

The present Diploma Thesis marks the completion of my studies in the School of Naval Architecture and Marine Engineering of N.T.U.A. At this point, I would like to express my gratitude to all the people who supported me during the preparation of this work.

First of all, I would like to sincerely thank my family, for all the efforts and support throughout my studies. I would also like to express my deepest gratitude to my supervisor, Assistant Professor Christos Papadopoulos for his critical help, advices and motivation that he provided during the preparation of my Thesis and finally for developing a very good collaboration environment.

Furthermore, I would like to thank Mr. Eleftherios Koukoulopoulos, Ph.D. candidate at N.T.U.A., for all his help from the first day of this Thesis, and for his decisive contributions in many different aspects of this work. Many special thanks are owed to Dr. Dimitrios Fouflias for his help in the technical aspects that came up during the design and construction of the experimental set up.

Finally, I would like to thank, Mr. Nikos Papadimitriou, owner of the Karathanos Bros & Co Machine Shop, for his help and support during the construction of the components of the journal bearing test rig, and Mr. Yiannis Ntaliapes, technician at the Laboratory of Marine Engineering, for his assistance in several technical issues that arose during the construction of the test rig.

# Σύνοψη

Η τριβή είναι μία από τις πιο σημαντικές αιτίες απώλειας ενέργειας και φθοράς μεταξύ επιφανειών που βρίσκονται σε σχετική κίνηση, και οδηγεί σε αλλοίωση της μηχανικής απόδοσης και, τελικά, σε αστοχία των αλληλεπιδρούντων τεμαχίων. Η μικρο/νανο τριβολογία αποτελεί ένα σχετικά νέο πεδίο επιστήμης, που ασχολείται με την επίδραση των μικρο/νανο τροποποιήσεων της επιφάνειας στην απόδοση των τριβολογικών επαφών. Τα ακτινικά έδρανα ολίσθησης είναι μηχανολογικά τεμάχια που χρησιμοποιούνται για την παραλαβή των ακτινικών φορτίων που καταπονούν περιστρεφόμενους άξονες. Κατά τη λειτουργία, ένα λεπτό φιλμ λιπαντικού δημιουργείται μεταξύ του άξονα και του εδράνου, ελαχιστοποιώντας την τριβή ολίσθησης και αποτρέποντας την επαφή μετάλλου με μετάλλο. Η απόδοση των ακτινικών εδράνων ολίσθησης, που συνήθως ποσοτικοποιείται μέσω του ελάχιστου πάχους του λιπαντικού και του συντελεστή τριβής, αλλάζει αισθητά σε διαφορετικές συνθήκες λειτουργίας (ακτινικό φορτίο, περιστροφική ταχύτητα άξονα, ιξώδες λιπαντικού).

Στην παρούσα εργασία, παρουσιάζεται μια υπολογιστική μελέτη της υδροδυναμικής λίπανσης σε ακτινικά έδρανα ολίσθησης, τα οποία φέρουν διαφορετικούς τύπους επιφανειακής κατεργασίας σε μέρος της επιφάνειας τους. Τα χαρακτηριστικά του ακτινικού εδράνου υπολογίζονται με επίλυση της εξίσωσης Reynolds, χρησιμοποιώντας έναν επιλύτη πεπερασμένων διαφορών που έχει αναπτυχθεί εντός του ΕΜΠ. Πέντε διαφορετικοί τύποι ακτινικών εδράνων συγκρίνονται με βάση την απόδοση τους υπό διαφορετικούς συνδυασμούς ακτινικού φορτίου και περιστροφικής ταχύτητας: (α) έδρανο με μία ενιαία ρηχή κοιλότητα στην περιοχή ανάπτυξης υδροδυναμικής πίεσης, (β) έδρανο με ρηχές περιφερειακές εγκοπές, (γ) έδρανο με ρηχές αξονικές εγκοπές, (δ) έδρανο με ορθογωνική επιφανειακή τραχύτητα, και (ε) έδρανο με υδροφοβικότητα. Προκειμένου να ευρεθεί η πιο αποτελεσματική σχεδίαση για κάθε τύπο εδράνου, ακολουθείται μια προσέγγιση πολυκριτηριακής βελτιστοποίησης, που βασίζεται σε γενετικό αλγόριθμο. Στόχο της βελτιστοποίησης αποτελεί η εύρεση των κύριων σχεδιαστικών παραμέτρων του ακτινικού εδράνου (βάθος εγκοπής, αξονικά/περιφερειακά όρια εγκοπών, μήκος ολίσθησης, αξονικά/περιφερειακά όρια υδροφοβικότητας), οι οποίες ελαχιστοποιούν τον συντελεστή τριβής και μεγιστοποιούν το πάχος του λιπαντικού ελαίου.

Τα αποτελέσματα της υπολογιστικής διαδικασίας επαληθεύτηκαν πειραματικά σε διάταξη πειραματικών δοκιμών για ακτινικά έδρανα, που σχεδιάστηκε και κατασκευάστηκε στο πλαίσιο της παρούσας διπλωματικής εργασίας. Η πειραματική διάταξη, που χαρακτηρίζεται από ρότορα (άξονα) διαμέτρου 30 mm, έχει σχεδιαστεί για να συνδέεται με το υπάρχον τριβόμετρο Bruker UMT-3SYS και είναι σε θέση να μετράει με ακρίβεια, το επιβαλλόμενο φορτίο στο ακτινικό έδρανο, τη ροπή τριβής, τη θέση ισορροπίας του άξονα (εκκεντρότητα, γωνία συμπεριφοράς), όπως επίσης και την αναπτυσσόμενη πίεση και θερμοκρασία σε αρκετές θέσεις του

ακτινικού εδράνου, κάτω από σταθερές και μεταβλητές στο χρόνο καταστάσεις φορτίου.

# Abstract

Friction is one of the most important causes of energy loss and wear between interacting surfaces in relative motion, leading to deterioration of mechanical performance and, eventually, to failure of the interacting components. Micro/Nano tribology constitutes a fairly new field of science, concerned with the effects of micro/nano surface modifications on the performance of tribological contacts. Journal bearings are mechanical components used to support the radial loads of rotating shafts. During operation, a thin lubricant film is maintained between the shaft and the bearing, minimizing sliding friction and aiding in preventing metal-to-metal contact. Performance of journal bearings, commonly quantified in terms of minimum lubricant thickness and friction coefficient, changes substantially at different operating conditions (radial load, shaft rotational speed, lubricant viscosity).

In the present study, a computational investigation of hydrodynamic lubrication in journal bearings exhibiting different types of surface treatment at part of the bearing surface is presented. Here, bearing performance is computed by solution of the Reynolds equation, utilizing an in-house finite difference solver. Five different types of journal bearings are cross-evaluated for operation at different combinations of radial load and rotational speed: (a) a pocket bearing, (b) a bearing with circumferential grooves, (c) a bearing with axial grooves, (d) a bearing with rectangular texturing, and (e) a hydrophobic bearing. To identify the most efficient designs for each bearing type, a multi-objective optimization approach is followed, based on genetic algorithms. The optimization goal is to identify the main bearing design parameters (texture depth, axial/circumferential texture extents, slip length, axial/circumferential hydrophobic extents) which simultaneously minimize friction coefficient and maximize minimum lubricant thickness.

The outcome of the numerical process is verified experimentally in a journal bearing test rig, designed and constructed in the framework of the present diploma thesis. The test rig, characterized by a rotor diameter of 30 mm, is designed to fit in an existing Bruker UMT-3SYS tribometer, and is capable of accurately measuring bearing load, friction torque, shaft equilibrium position (eccentricity, attitude angle), as well as pressure and temperature at several bearing locations, under both steady-state and transient bearing load conditions.

## Nomenclature

| | |
|---|---|
| $B$ | bearing width [m]: B=π·D |
| $b_s$ | slip length [m] |
| $c$ | bearing radial clearance [m]: c= $R_1$-$R_2$ |
| $c_p$ | thermal capacity of the lubricant [J/(kg·K)] |
| $D$ | bearing diameter [m]: D=2·R |
| *depth* | the depth of the texturing in both axis |
| *density_x* | density of the surface that contains the texturing along the x axis |
| *density_y* | density of the surface that contains the texturing along the y axis |
| $e$, $\varepsilon$ | eccentricity [m],<br>dimensionless eccentricity ratio: $\varepsilon = \frac{e}{c}$ |
| $E_p$ | power loss [W] |
| *end_x* | angle at which the texturing ends on the x axis |
| *end_y* | non-dimensional value of the bearing length at which texturing ends |
| $F$ | friction force [N] |
| $f$ | normalized friction coefficient: f=μ(R/c) |
| $h$ | lubricant film thickness [m] |
| $h_1$, $h_0$ ($h_{min}$) | maximum film thickness [m],<br>minimum film thickness [m] |
| $L$ | bearing length [m] |
| $N_s$ | shaft rotational speed [RPS] |
| $N$ | shaft rotational speed [RPM] |
| $N_x, N_y$ | number of dimples on the circumferential direction<br>number of dimples on the axial direction |
| $O_B$,$O_S$ | bush center [m],<br>shaft center [m] |
| $P_z$ | vertical external load [N] |
| $p_m$ | mean pressure in bearing $p_m = \frac{P}{LD}$ [Pa] |
| $p$, $p_{max}$,$p_{pump}$ | pressure [Pa],<br>maximum pressure [Pa]<br>oil pump pressure [Pa] |
| $Q_I$, $Q_L$ | inlet flow rate [$m^3$/s],<br>outlet flow rate [$m^3$/s] |
| $Q_x$, $Q_y$ | lubricant inlet flow rate per unit length [$m^2$/s],<br>lubricant outlet flow rate per unit width [$m^2$/s] |
| $R$ | bearing radius [m] |

| | |
|---|---|
| $R_1$, $R_2$ | bush radius [m],<br>shaft radius [m] |
| $S$ | sommerfeld number: $S = \frac{W}{LU\eta}\left(\frac{c}{R}\right)^2$ |
| *slip_start_angle* | angle at which the hydrophobicity starts on x axis [deg] |
| *slip_start_y* | non-dimensional value of the bearing length at which hydrophobicity starts |
| *slip_end_angle* | angle at which the hydrophobicity ends on x axis [deg] |
| *slip_end_y* | non-dimensional value of the bearing length at which hydrophobicity ends |
| *start_x* | angle at which the texturing starts on the x axis [deg] |
| *start_y* | non-dimensional value of the bearing length at which texturing ends |
| $T_z$ | friction torque [N·m] |
| $U$ | rotor linear velocity [m/s] |
| $U_1$, $U_2$ | x-axis stator speed [m/s],<br>x-axis rotor speed [m/s] |
| $u$ | x-axis fluid velocity [m] |
| $V_1$, $V_2$ | y-axis stator speed [m/s],<br>y-axis rotor speed [m/s] |
| $v$ | y-axis fluid velocity [m] |
| $W$ | load capacity [N] |
| $w$ | z-axis fluid velocity [m] |
| $w_0$ | vertical velocity of bottom surface [m/s] |
| $w_h$ | vertical velocity of top surface [m/s] |
| $x$ | x-axis coordinate [m] |
| $y$ | y-axis coordinate [m] |
| $z$ | z-axis coordinate [m] |
| $\Delta T$ | temperature rise [K] |
| $\eta$ | fluid dynamic viscosity [Pa·s] |
| $\theta_{cav}$ | cavitation angle [deg] |
| $\theta_{max}$ | maximum pressure angle [deg] |
| $\mu$ | friction coefficient: $\mu = F/W$ |
| $\rho$ | lubricant density [kg/m$^3$] |
| $\tau_c$ | critical shear stress [Pa] |
| $\tau_x$, $\tau_y$ | shear stress in x direction [Pa]<br>shear stress in y direction [Pa] |
| $\varphi$ | attitude angle [deg] |
| $\psi$ | $\Psi = \frac{c}{R}$ |
| $\omega$ | angular velocity [s$^{-1}$] |

## List of figures

## List of tables

# 1 Introduction

## 1.1 Overview- The significance of tribology

Tribology is a relatively new field of science, studying friction, wear and lubrication of mechanical interacting components. It is applicable to a wide range of applications, from household appliances to space structures. Due to its interdisciplinary nature it is directly linked to scientific domains, such as mathematics, physics and material technology [1]. Friction is a major cause of wear, which leads to material wastage and degradation of mechanical performance. The most common way to reduce wear is through the reduction of friction, which is achieved with the insertion of a thin lubricating film between the two interacting surfaces, being also the basic idea of hydrodynamic lubrication. Interacting surfaces can be found in almost all machinery with moving parts, such as gears, bearings and couplings. Therefore, design improvements, which will increase the expected lifetime and decrease operational costs of components, can have a significant impact on the contemporary standard of living.

As mentioned earlier, tribology mainly focuses on the study of the characteristics of the intervening film between contacting bodies, and the consequences of either film failure or absence of a film, which are usually manifested by severe friction and wear. Film formation between two sliding objects is a physical phenomenon that prevents the extremely high shear rates at their common interface. Therefore, the practical objective of tribology is to minimize the two main disadvantages of solid to solid contact, meaning friction and wear.

The field of marine engineering is no exception and comprises many applications where friction plays a decisive role in overall performance. In ships, important power losses are present in Diesel engines (in piston rings, crankshaft bearings and connecting rod bearings, which in total lead to power losses approximately 5-7.5% of engine BHP), at the shafting system (where losses of 1-2% of BHP in thrust bearing and journal bearings are found), as well as in the gear unit (with losses around 1-2% of BHP), if present. Energy cost due to friction and wear for a particular mechanical component may seem low compared to the total power of the device, but if they are examined under the scope of annual costs of a certain fleet of sea-going vessels, the power savings can reach a considerable value.

## 1.2 Historical-Literature review

Hydrodynamic lubrication is the most common way to reduce friction and wear. Stachowiak [1] mentions that hydrodynamic lubrication origins from the end of the 19$^{th}$ century, inspired by the Beachamp Tower experiments, and the field was further advanced by Osborne Reynolds and other theoreticians. At the beginning of the 20$^{th}$ century, hydrodynamic lubrication was successfully applied to thrust bearings, and it was used for the support of the ship propeller shaft. Hydrodynamic

lubrication is a phenomenon still studied to this day, and constantly being enriched with modern publications.

The mathematical equation governing this phenomenon was first expressed by Reynolds, and nowadays it is known as the Reynolds Equation. This equation can be derived by applying certain assumptions to the general Navier-Stokes fluid equations. In order for hydrodynamic lubrication to occur, there are two conditions, always to be met:

- Pressure is developed only along the lubricating film, two surfaces move relatively to each other,
- The two surfaces must be inclined at some angle to each other.

One of the typical applications of hydrodynamic lubrication are journal bearings, which are found in mechanical systems that utilize a rotating shaft to transfer torque. A typical journal bearing consists of a stationary bush, which houses the rotating shaft. The shaft and the bush are the two surfaces moving relatively to each other, so a load-carrying lubricating film is generated between these two. There are two main aspects of journal bearing analysis: The first aspect is related to design and performance, whereas the second is related to practical or operational problems, such as vibration, cavitation, and lubricant supply [1].

One of the first experiments on journal bearings was performed by Beauchamp Tower in the end of the 19$^{th}$ century. When he noticed that the oil in journal bearing always leaked out of the hole located beneath the load location, he plugged it with a cork only to find out that the cork was slowly forced out of the hole by the oil. He then realized that a yet unknown mechanism was responsible for pressurizing the oil. After measuring oil pressure, Tower realized that it was responsible for separating the two surfaces by developing a significant hydraulic force. Since then, the improvement in the design of journal bearings has been aided by corresponding developments on a theoretical and practical level. The analyses of hydrodynamic journal bearings was originally based on the solution of Reynolds equation for pressure distribution. A more detailed analysis of the geometric characteristics of the lubricating film in journal bearings is presented in [1]. Khonsari has presented a thorough numerical investigation of journal bearings with different geometric and operational characteristics. In particular, in [2], bearings with different length to diameter ratios, ranging from 1/8 to 2, and different combinations of load and rotational speed, have been investigated, and the main performance indices of the bearings have been reported. In his study, Khonsari solved the Reynolds equation with a Reynolds boundary condition, which assumes zero pressure and pressure gradients in the boundary between the active and the cavitating regions of the bearing.

Further understanding of the occurring tribological phenomena of journal bearing has led to new improvement potentials of the existing bearing designs. A method that has recently drawn significant attention is related to the implementation of appropriate roughness patterns on the face of the bearing surface. This process is

called artificial surface texturing, and is about the introduction of small, periodic irregularities of various shapes on a lubricated surface in order to reduce frictional losses and increase load carrying capacity. Both experimental [3]-[5] and numerical [6]-[9] studies have confirmed the effectiveness of such solutions: proper distribution, depth and shape of the various textures seem to generate additional hydrodynamic load capacity. A fair amount of the experimental studies is focused on the measurement of the friction torque, as it is one of the most important parameters of the bearing performance and a direct means of calculating mechanical losses of the bearing. Each research team has designed a specific experimental rig in order to measure friction torque [3], [5], [10]-[13], nonetheless most of them share some common features, which are directly related to journal bearing operation.

Although optimization of textured surfaces seems to have the potential to substantially improve bearing designs, many researchers have recently shifted their focus to the study of a much more promising surface treatment. In particular, many efforts have been oriented towards the idea of applying hydrophobic properties on sliding surfaces. Hydrophobic surfaces have wetting resistant characteristics, which drastically reduce the levels of friction during fluid flow. A series of experimental studies using several different methods has proven that, on hydrophobic surfaces, simple Newtonian liquids can slip over the solid boundary [14], [15]. Studies have shown that with a proper distribution of hydrophobicity over the surface, friction torque may exhibit a significant reduction.

Finally, some numerical studies examine the combination of textured and hydrophobic surfaces, using partially textured slip journal bearings, where hydrophobicity is applied at the bottom surface of the artificially crafted textures [16]. Through this modification both lower friction torque and higher load carrying capacity can be achieved and also protection of hydrophobicity from wear, under a practical scope.

## 1.3 Goals of the present study – Thesis outline

The goal of the present Thesis is the study, development and construction of an experimental setup that will enable the study of operational characteristics of plain journal bearings and of journal bearings that have undergone surface treatment modification in part of the stator, either artificial surface texturing or hydrophobicity. Hydrophobic surfaces are wetting resistant, exhibiting low friction during fluid flow, while artificial texturing refers to introducing small periodic dimples on the surfaces which, if applied properly, can lower the friction coefficient and increase load capacity.

In Chapter 2, the basic principles of the theory of hydrodynamic lubrication are presented, along with the formulation of the Reynolds equation for the plain journal bearing surface. In Chapter 3, numerical simulations of textured and hydrophobic bearings are presented and the results are compared to those corresponding to a conventional plain journal bearing. In Chapter 4, the design of the experimental setup is described, along with the already existing experimental equipment. In Chapter 5,

the experimental measurements are presented and are compared to the relative numerical results of Chapter 3. Finally, in Chapter 6 the basic conclusions are drawn and some ideas of future work are proposed.

# 2 Journal Bearings

## 2.1 Overview (based on [2], [16])

Journal bearings are used in a variety of engineering applications, so proper study of tribology has a major impact on their performance. A journal bearing consists of a cylindrical body around a rotating shaft, used either for supporting a radial load or simply as a guide for smooth transmission of torque. It involves a stationary sleeve (or bushing) with a complete 360 arc or various arrangements of a partial arc or arcs in a housing structure. The inner surface is commonly lined with a soft bearing material such as lead, tin, white metal and babbitt metal or even plastic.

Plain journal bearings are susceptible to a form of instability known as self-excited oil whirl. Over the years, a series of bearing designs have been developed for suppressing such vibration problems, such as bearings with tilting pad, elliptical, pressure dam, and offset split bearings.

Once the shaft is in steady state, it assumes a position within the bearing bush whose coordinates are eccentricity $e$ and attitude angle $\varphi$, as shown in Figure 1. Eccentricity is simply the displacement of the journal center $O_j$ from the bushing center $O_b$. Attitude angle is the angle between the load line and the line between these centers. Eccentricity decreases and attitude angle commonly increases with more vigorous oil-film pumping action by the journal at higher speeds and with increased lubricant viscosity.

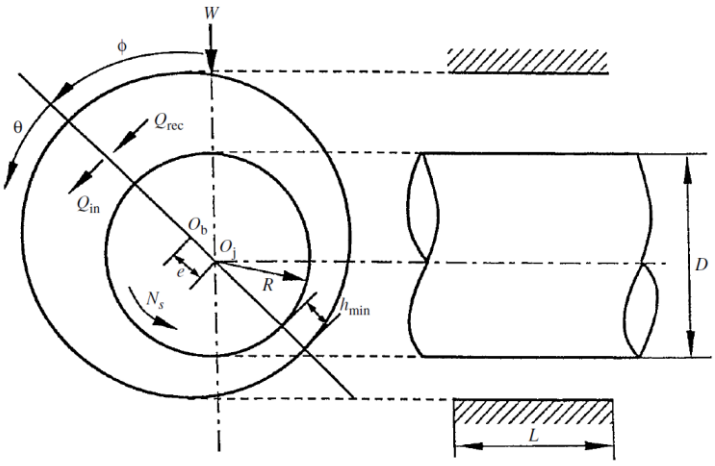


**Figure 1: Cross section of a journal bearing and its characteristic geometric parameters [2].**

In many applications, rotor weight and any external load are supported on two identical bearings located on either end of the shaft. A journal may also run centered in its bearing with zero eccentricity if its shaft is positioned vertically so that gravity does not contribute to the load. As in vertical pumps and motors, these lightly loaded bearings are particularly susceptible to troublesome oil whirl instability, as the unloaded journal tends to gyrate in the rotating oil film.

Kostopoulos [16] describes how the use of journal bearings comes with a series of advantages:

- They are often constructed in divided parts or as a whole body and their assembly is simple
- The small clearance renders them usable in high-accuracy constructions
- Because of the way they are build, dust cannot enter the lubricant area, protecting the surfaces of bushing and rotor
- A hydrodynamic lubricating film is formed between the working surfaces, therefore minimizing the wear of the working parts and maximizing the lifespan of the journal bearing
- They can withstand large applied loads

Their main disadvantages are the following:

- High friction coefficient during the startup process (transient conditions)
- Frequent maintenance
- A significant amount of lubricant and a lubricating system is necessary

In applications where the system starts up under an applied load, the hydrodynamic lubricating film is developed above a certain value of rotational speed. On the other hand, journal bearings are not performing efficiently at very high rotational speed values. That is happening because as rotor speed rises, the lubricating film becomes turbulent, increasing shear stress. This results in higher lubricant temperature and the subsequent thinning of the hydrodynamic film. Tangential rotational shaft speeds of 75 mm/s are considered high enough, but in certain applications rotational speeds of 150 mm/s have also been achieved. Journal bearings can become quite costly when a custom design is needed, and when produced in small amount. On the other hand, journal bearings that are massively produced are quite economical.

There are five different lubrication types of a journal bearing as shown below:

*Hydrodynamic lubrication*:

According to this type of lubrication, the surfaces of the bushing and the rotor are separated by a lubricating film in order to prevent metal to metal contact. A constant supply of lubricating oil is necessary, but is not dependent on inlet pressure of the lubricant. When the rotational speed surpasses a certain value, a pressure film is developed between the two surfaces, enabling it to withstand the applied load, while keeping the two surfaces apart.

*Hydrostatic lubrication*:

In this lubrication type the lubricating film, being either oil or water or air, is inserted between the shaft and the bearing bush under pressure, high enough to separate the bearing and rotor and to withstand the applied load. So, the fluid film is already pressurized, meaning that relative motion of the two surfaces is not required.

*Elasto-hydrodynamic-lubrication*:

In cases of high load, or soft materials, the bearing or the shaft undergo elastic deformations during operation. Those deformations affect the fluid-film geometry, which, in turn affects bearing performance. In such cases, the bearing is operating in elastohydrodynamic conditions; modeling should take into consideration this phenomenon for accurate calculations.

*Boundary lubrication*:

Boundary lubrication takes place when the thickness of the lubricant is inadequate, due to a variety of factors, such as small surface of the bearing, low rotational speed of the shaft, little amount of lubricant, high applied load. The transition from the hydrodynamic lubrication occurs gradually. In the intermediate stage hydrodynamic and boundary lubrication coexist, giving rise to the so-called mixed lubrication.

*Solid-film lubrication:*

In this lubrication, a solid type of lubricant, such as grease or graphite is used in applications where mineral oils cannot be used, or in cases where excessive heating of the interacting components is present.

The most commonly used type of lubrication for journal bearings is the hydrodynamic lubrication, and it will be presented in detail in section 2.2. It is also the type of lubrication that is used in the experiments of the present Thesis.

## 2.2 Hydrodynamic Lubrication

### 2.2.1 Hydrodynamic lubrication theory (based on [1])

Hydrodynamic lubrication is the phenomenon in which two relatively moving non-parallel surfaces are separated by a pressurized thin lubricating fluid film. A simple converging slider is presented in Figure 2. The top surface (stator) is inclined at a certain angle relatively to the bottom surface (runner). The space between the two surfaces is filled with lubricant and moves with a certain velocity. During this motion, a pressure field is generated in the fluid domain and the pressure gradient causes the fluid velocity profile to bend inwards at the entrance of the wedge and outwards at the exit. The generated pressure field has the ability to support a certain load applied to the slider. The whole process of hydrodynamic lubrication can be described mathematically, by making certain assumptions to the general Navier-Stokes fluid equations.

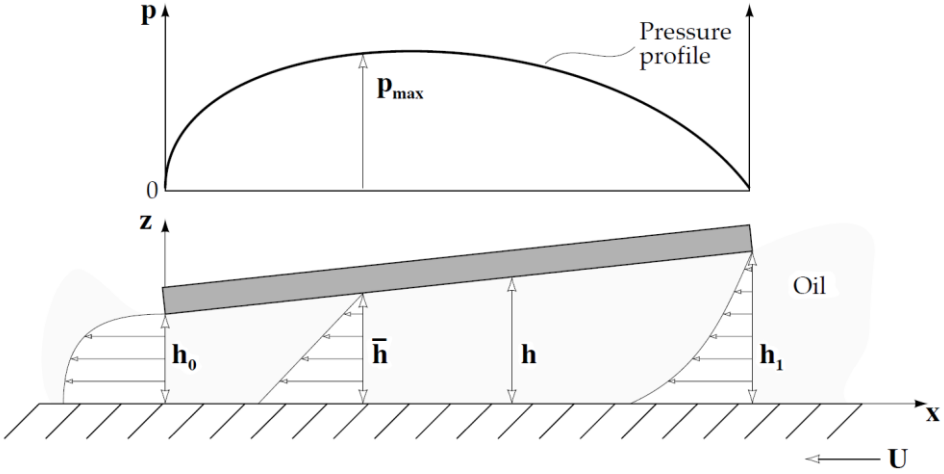


**Figure 2: Principle of hydrodynamic lubrication [1].**

### 2.2.2 Mathematical approach-Reynolds approximation (based on [1])

*Simplifying assumptions*

As Stachowiak mentions [1], because of their complexity, the physical processes in most engineering applications cannot easily be described by exact mathematical equations. This is a result of the many interacting factors and variables in real environments. Therefore, in order to derive the Reynolds equation a series of simplifying assumptions of the equations have been introduced and are shown as follows:

- Body forces are neglected
- Pressure is constant through the film thickness
- No slip is assumed at the fluid-solid interfaces
- Lubricant behaves as a Newtonian fluid
- Flow is laminar
- Fluid inertia is neglected
- Fluid density is constant
- Viscosity is constant throughout fluid domain

The Reynolds equation is derived by considering the equilibrium of a small element of fluid within hydrodynamic film and continuity of flow in a column.

*Element equilibrium*

The fluid element is in equilibrium, so the forces acting on both directions balance each other, as shown in Figure 3. As a result, the following equation is valid for the x-direction:

$$pdydz + \left(\tau_x + \frac{\partial \tau_x}{\partial z} dz\right) dxdy = \left(p + \frac{\partial p}{\partial x} dx\right) dydz + \tau_x dxdy \qquad (1)$$

which is equivalent to:

$$\frac{\partial \tau_x}{\partial z} dxdydz = \frac{\partial p}{\partial x} dxdydz \tag{2}$$

The element of fluid under consideration is not of zero volume, so both sides of equation (2) can be divided by the value dxdydz and the equilibrium is expressed by the following equation:

$$\frac{\partial \tau_x}{\partial z} = \frac{\partial p}{\partial x} \tag{3}$$

The second equilibrium condition can be derived by applying all the above for the y-direction. The equilibrium equation for the y axis is:

$$\frac{\partial \tau_y}{\partial z} = \frac{\partial p}{\partial y} \tag{4}$$

Z-axis corresponds to the film thickness direction. Therefore, pressure is assumed constant in the film direction, which yileds:

$$\frac{\partial p}{\partial z} = 0 \tag{5}$$

The expression for the shear stress $\tau_x$ is:

$$\tau_x = \eta \frac{u}{h} = \eta \frac{\vartheta u}{\vartheta z} \tag{6}$$

where:

$\tau_x$ is the shear stress acting on the x direction [Pa];

$u$ is the velocity along the x axis [m/s]

η is the dynamic viscosity, [Pa·s]

The expression for the shear stress $\tau_y$ is:

$$\tau_y = \eta \frac{v}{h} = \eta \frac{\vartheta v}{\vartheta z} \tag{7}$$

where:

$\tau_y$ is the shear stress acting on the y direction (Pa);

$v$ is the sliding velocity along the y axis (m/s)

By substituting the above equations for the shear stresses $\tau_x$ and $\tau_y$ in the equilibrium equations we get:

$$\frac{\partial p}{\partial x} = \frac{\vartheta}{\vartheta z} (\eta \frac{\vartheta u}{\vartheta z}) \tag{8}$$

$$\frac{\partial p}{\partial y} = \frac{\vartheta}{\vartheta z}(\eta \frac{\vartheta v}{\vartheta z}) \tag{9}$$

Considering a constant viscosity value throughout the fluid domain, the above equations can be integrated twice, as the viscosity is not a function of z:

$$\frac{\vartheta p}{\vartheta x}\frac{z^2}{2} + C_1 z + C_2 = \eta u \tag{10}$$

As for the boundary conditions, an assumption of no slip at the solid boundaries is made:

$$u = U_2 \; at \; z = 0$$

$$u = U_1 \; at \; z = h$$

Using the boundary conditions the constants $C_1$and $C_2$ can be calculated, by the following expressions:

$$C_1 = (U_1 - U_2)\frac{\eta}{h} - \frac{\vartheta p}{\vartheta x}\frac{h}{2} \tag{11}$$

$$C_2 = \eta U_2 \tag{12}$$

Substituting $C_1$and $C_2$ yields:

$$\frac{\vartheta p}{\vartheta x}\frac{z^2}{2} + (U_1 - U_2)\frac{\eta z}{h} - \frac{\vartheta p}{\vartheta x}\frac{hz}{2} + \eta U_2 = \eta u \tag{13}$$

The expression for the velocity *u* in the x direction is:

$$u = \left(\frac{z^2 - zh}{2\eta}\right)\frac{\vartheta p}{\vartheta x} + (U_1 - U_2)\frac{z}{h} + U_2 \tag{14}$$

Similarly, the expression for the velocity *v* is obtained by the following expression:

$$v = \left(\frac{z^2 - zh}{2\eta}\right)\frac{\vartheta p}{\vartheta x} + (V_1 - V_2)\frac{z}{h} + V_2 \tag{15}$$

Each one of the three separate terms in the velocity equations represent the velocity profiles across the fluid film.

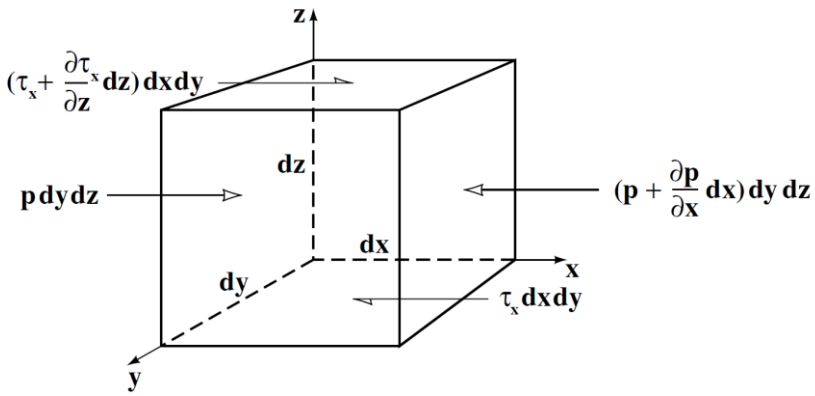


**Figure 3: Fluid element equilibrium [1].**

*Continuity of flow in a column*

The lubricant flows into the column horizontally at rates $q_x$ *and* $q_y$ and out of the column at rates of $(q_x + \frac{\vartheta q_x}{\vartheta x} dx)$ and $(q_y + \frac{\vartheta q_y}{\vartheta y} dy)$ per unit length and width respectively. The above expressions are for the horizontal direction of the flow of lubricant.

For the vertical direction of the flow, the flow rate of the lubricant into the column is expressed as $w_0 dxdy$ and out of the column as $w_h dxdy$ , where:

- $w_0$ is the velocity at which the bottom of the column moves up and
- $w_h$ is the velocity at which the top of the column moves up

Following the principle of continuity of flow the influx of a liquid must equal its efflux, then the following equation is valid:

$$q_x dy + q_y dx + w_0 dxdy = \left(q_x + \frac{\vartheta q_x}{\vartheta x} dx\right) dy + \left(q_y + \frac{\vartheta q_y}{\vartheta y} dy\right) dx + w_h dxdy \qquad (16)$$

Since dxdy≠ 0 the above equation can be rewritten as:

$$\frac{\vartheta q_x}{\vartheta x} + \frac{\vartheta q_y}{\vartheta y} + (w_h - w_0) = 0 \qquad (17)$$

which is the equation of continuity of flow in a column.

In order to calculate the flow rates $q_x$ *and* $q_y$ per unit length, an integration of the lubricant velocity over the film thickness is required. The flow rate in the x direction is equal to:

$$q_x = -\frac{h^3}{12\eta}\frac{\vartheta p}{\vartheta x} + (U_1 - U_2)\frac{h}{2} \qquad (18)$$

Similarly the flow rate in the y direction equals to:

$$q_y = -\frac{h^3}{12\eta}\frac{\vartheta p}{\vartheta y} + (V_1 - V_2)\frac{h}{2} \tag{19}$$

Under the assumption that there is no local variation in surface velocity in the x and y directions we get the full form of the Reynolds equation in three dimensions:

$$\frac{\vartheta}{\vartheta x}\left(\frac{h^3}{\eta}\frac{\vartheta p}{\vartheta x}\right) + \frac{\vartheta}{\vartheta y}\left(\frac{h^3}{\eta}\frac{\vartheta p}{\vartheta y}\right) = 6\left(U\frac{dh}{dx} + V\frac{dh}{dy}\right) + 12(w_h - w_0) \tag{20}$$

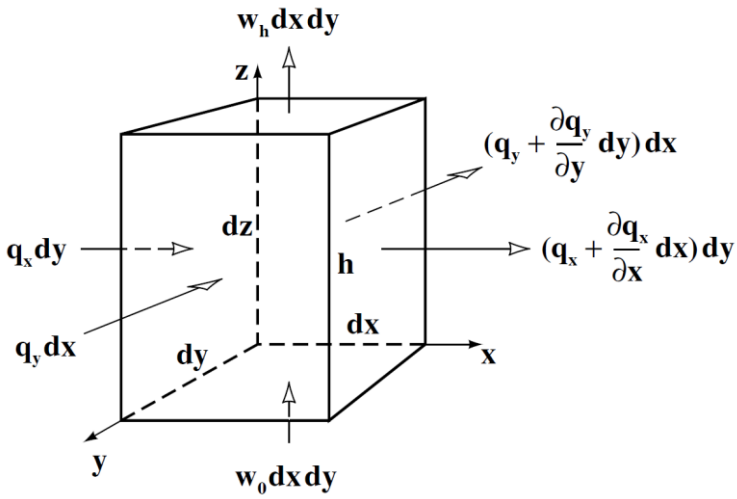


**Figure 4: Continuity of flow in a column [1].**

Solving Reynolds equation for pressure distribution, most of the critical bearing design parameters can be evaluated by a simple integration, as shown below.

*Pressure Distribution*

The pressure distribution can now be derived by integrating the Reynolds equation over a specific film shape. The film shape can be described by some function *h=f(x,y)*.

*Load Capacity*

Load capacity can be calculated by integrating the pressure distribution over a certain bearing area:

$$W = \int_0^L \int_0^B p dx dy \tag{21}$$

*Friction Force*

In order to calculate the total friction force operating across the hydrodynamic film, it is necessary to integrate shear stress τ over the bearing area, as follows:

$$F = \int_0^L \int_0^B \tau dx dy \tag{22}$$

$$\tau = \eta \frac{du}{dz} \tag{23}$$

After substituting $\tau$ in (22) and integrating the formula is set as:

$$\frac{F}{L} = \pm \int_0^B \frac{h}{2}\frac{dp}{dx}dx - \int_0^B \frac{U\eta}{h}dx \tag{24}$$

Where (+) refers to the upper surface and (–) refers to the lower one.

*Coefficient of Friction*

Coefficient of friction is calculated as the ratio of the friction force to load capacity:

$$\mu = \frac{F}{W} = \frac{\int_0^L \int_0^B \tau dxdy}{\int_0^L \int_0^B pdxdy} \tag{25}$$

*Lubricant flow*

Lubricant flow can be calculated by integrating the flow expressions $q_x$ $and$ $q_y$ over the two edges of the bearing:

$$Q_x = \int_0^L q_x dy \tag{26}$$

$$Q_y = \int_0^B q_y dx \tag{27}$$

Simplifications to the Reynolds equations

The original form of Reynolds equation is quite complex to be used in practical engineering applications, so several simplifying assumptions can be made, suitable for each different problem.

*Unidirectional Velocity Approximation*

In most engineering systems, journal bearings work in a way, that it can be assumed that the velocity on one of the axes equals to zero, i.e. V=0. By assuming V=0 the Reynolds equation equals to:

$$\frac{\vartheta}{\vartheta x}\left(\frac{h^3}{\eta}\frac{\vartheta p}{\vartheta x}\right) + \frac{\vartheta}{\vartheta y}\left(\frac{h^3}{\eta}\frac{\vartheta p}{\vartheta y}\right) = 6U\frac{dh}{dx} + 12(w_h - w_0) \tag{28}$$

*Steady film thickness approximation*

Another simplifying assumption is to assume that the distance between the two surfaces remains constant through the operation, so that there is no vertical flow across the film, i.e. $w_h - w_0 = 0$. This is a quite inaccurate assumption as in most bearings the vibration that is developed, make the distance of the operating surfaces to vary. Despite that fact, assuming that the vertical flow equals to zero gets:

$$\frac{\vartheta}{\vartheta x}\left(\frac{h^3}{\eta}\frac{\vartheta p}{\vartheta x}\right) + \frac{\vartheta}{\vartheta y}\left(\frac{h^3}{\eta}\frac{\vartheta p}{\vartheta y}\right) = 6U\frac{dh}{dx} \tag{29}$$

*Isoviscous approximation*

In this assumption the lubricant viscosity is considered to be constant over the film, so that the thermal effects are neglected. So assuming that η=constant the Reynolds equation equals to:

$$\frac{\vartheta}{\vartheta x}\left(h^3\frac{\vartheta p}{\vartheta x}\right) + \frac{\vartheta}{\vartheta y}\left(h^3\frac{\vartheta p}{\vartheta y}\right) = 6U\eta\frac{dh}{dx} \tag{30}$$

*Infinitely long bearing approximation*

In order to further simplify the Reynolds it is assumed that the pressure gradient along the y axis can be neglected, i.e. ${}^{\vartheta p}/_{\vartheta y} = 0$ and $h \neq f(y)$. In order to do so it is assumed that the bearing is infinitely long in the y axis direction. This assumption reduces the Reynolds equation to a one dimensional form:

$$\frac{\vartheta}{\vartheta x}\left(h^3\frac{\vartheta p}{\vartheta x}\right) = 6U\eta\frac{dh}{dx} \tag{31}$$

Integrating the above equation gives:

$$h^3\frac{dp}{dx} = 6U\eta h + C \tag{32}$$

In order to solve equation (32) a boundary condition is needed. So, it is estimated that there is maximum pressure at some point along the lubricating film, and therefore the pressure gradient there equals to zero, i.e. ${}^{dp}/_{dx} = 0$ and the corresponding film thickness is denoted as $\bar{h}$. Now the boundary condition is:

$\frac{dp}{dx} = 0 \; at \; h = \bar{h}$, and is shown in Figure 5.

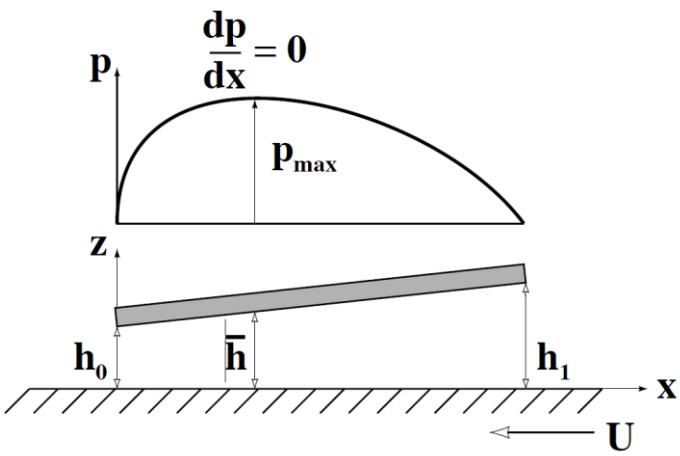


**Figure 5: Boundary condition in the infinitely long bearing approximation [1].**

Substituting the boundary condition to the equation (32) gives:

$$C = -6U\eta\bar{h} \tag{33}$$

So the final form of the Reynolds equation for the infinitely long bearing approximation equals to:

$$\frac{dp}{dx} = 6U\frac{h-\bar{h}}{h^3} \tag{34}$$

The pressure distribution for the infinitely long bearing approximation is shown in Figure 6.

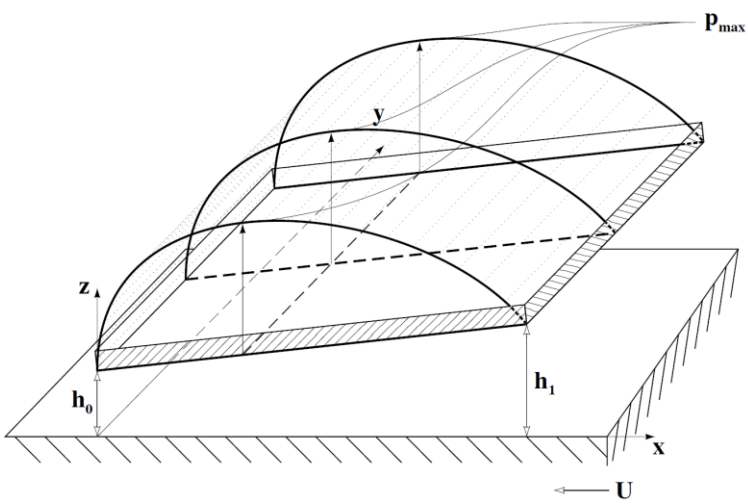


**Figure 6: Pressure distribution in the infinitely long bearing approximation [1].**

*Narrow bearing approximation*

This approximation is the opposite of the infinitely long bearing approximation. In this approximation it is assumed that the pressure gradient along the x axis is much smaller than the y axis i.e. ${}^{\vartheta p}/_{\vartheta x} \ll {}^{\vartheta p}/_{\vartheta y}$ and $h \neq f(y)$, as shown in Figure 7. This approximation came in use as new short bearings were introduced for use into internal combustion engines.

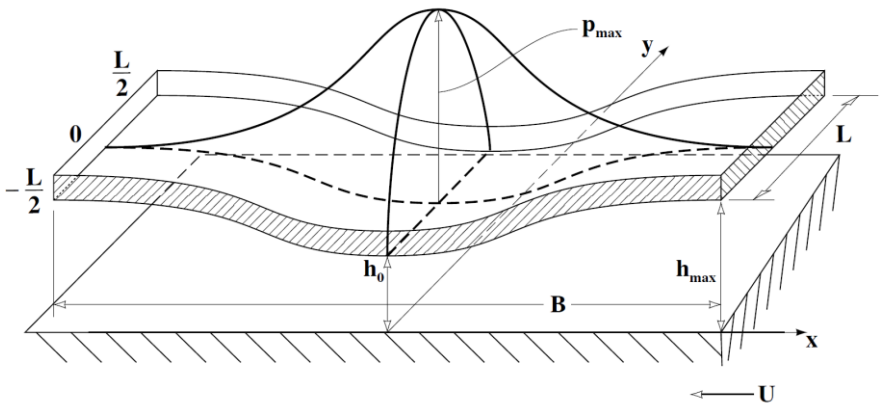


**Figure 7: Pressure distribution in the narrow bearing approximation [1].**

For the narrow bearing approximation L≪B and ${}^{\vartheta p}/_{\vartheta x} \ll {}^{\vartheta p}/_{\vartheta y}$, so the first term of the Reynolds can be neglected and the equation equals to:

$$\frac{\vartheta}{\vartheta y}\left(h^3 \frac{\vartheta p}{\vartheta y}\right) = 6U\eta \frac{dh}{dx} \tag{35}$$

Since $h \neq f(y)$:

$$\frac{d^2p}{dy^2} = \frac{6U\eta}{h^3}\frac{dh}{dx} \tag{36}$$

Integrating (36) results in:

$$\frac{dp}{dy} = \frac{6U\eta}{h^3}\frac{dh}{dx}y + C_1 \tag{37}$$

Integrating (37) gives:

$$p = \frac{6U\eta}{h^3}\frac{dh}{dx}\frac{y^2}{2} + C_1 y + C_2 \tag{38}$$

The boundary conditions for this case are:

$p = 0 \; at \; y = \pm\frac{L}{2}$ and $\frac{dp}{dy} = 0 \; at \; y = 0$

Substituting the boundary conditions into (37) and (38) results in:

$$C_1 = 0 \tag{39}$$

$$C_2 = \frac{-3U\eta}{h^3}\frac{dh}{dx}\frac{L^2}{4} \tag{40}$$

So, the pressure distribution equals to:

$$p = \frac{3U\eta}{h^3}\frac{dh}{dx}(y^2 - \frac{L^2}{4}) \tag{41}$$

At this point it should be noted that the infinitely long bearing approximation is used for bearings with L/D>3, while the narrow bearing approximation is used for bearings with L/D<1/3. For intermediate ratios of 1/3<L/B<3, the solutions that are applied are the computed ones for finite bearings.

## 2.3 Journal bearing calculation

### 2.3.1 Overview (based on [1])

The Reynolds equation that is used for the journal calculation is the isoviscous approximation, found in equation (30):

$$\frac{\vartheta}{\vartheta x}\left(h^3\frac{\vartheta p}{\vartheta x}\right) + \frac{\vartheta}{\vartheta y}\left(h^3\frac{\vartheta p}{\vartheta y}\right) = 6U\eta\frac{dh}{dx}$$

In order to solve equation (30) some boundary conditions are needed to be applied. For the better understanding of the boundary conditions a depiction of an unwrapped journal bearing is shown in Figure 8.

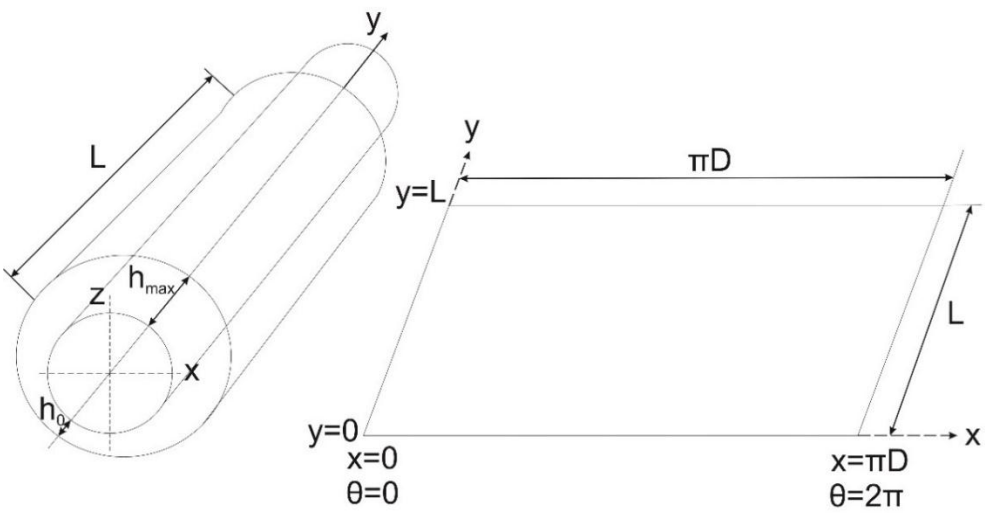


**Figure 8: Depiction of an unwrapped journal bearing [20].**

The three most common boundary conditions are:

*Full-Sommerfeld boundary condition*: It is the simplest of the boundary conditions, by assuming that the pressure equals to zero at the edges of the wedge. Full-Sommerfeld condition cannot be applied in real life, as the predicted load capacity is zero, because of the opposing negative and positive pressures that are developed in the hydrodynamic film region.

*Half-Sommerfeld boundary condition*: In the Half-Sommerfeld boundary condition negative pressures in the fluid domain are neglected (set to zero). So in this case, pressure remains constant (zero) in the diverging region of the hydrodynamic film.

*Reynolds boundary condition*: In order for the estimation of load capacity, bearing friction and lubricant flow rate to be accurate, the Reynolds boundary condition is commonly used. Reynolds suggested that negative fluid pressure should be set to zero, and at the boundary between zero and non-zero pressure, pressure gradient $dp/dx$ should also be zero. The corresponding pressure distribution is shown in Figure 9.

The Reynolds boundary condition is the one that is used in the present work, having been used in the numerical approach of the journal bearing.

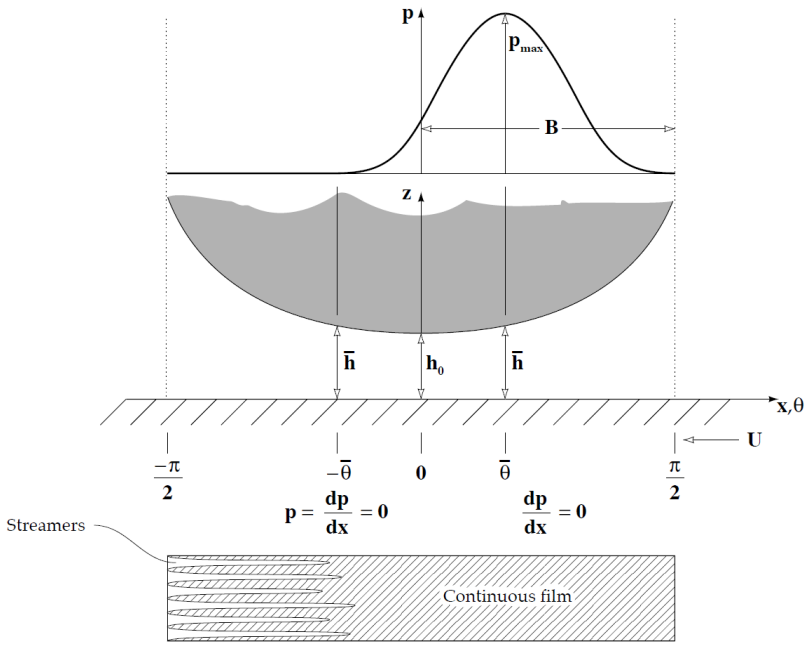


**Figure 9: Reynolds boundary condition and pressure distribution [1].**

### 2.3.2 Journal bearing geometry (based on [1],[2],[17])

In order to mathematically approach the journal bearing operation, it is initially essential to understand its geometry. The journal bearing has a radius $R_1$, while the journal (shaft) has a radius $R_2$, as shown in Figure 10.

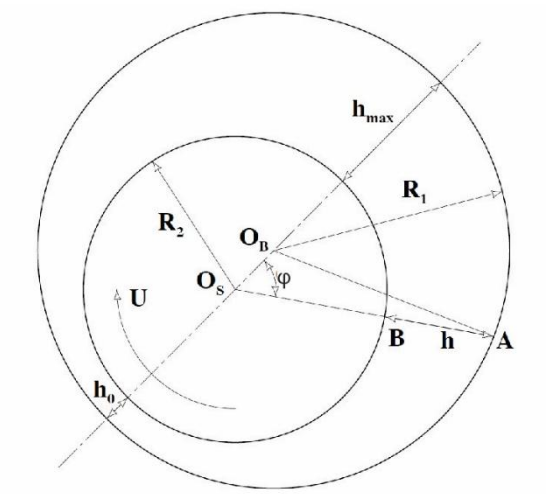


**Figure 10: Bearing geometry [1].**

In Figure 10 $O_B$ is the center of the bearing. Due to the radial load, the shaft is eccentric with respect to the bearing, with its center lying on $O_S$. The journal rotates with a tangential velocity *U*. The film thickness around the shaft is symbolled as *h*; at some point *h* exhibits its minimum value $h_{min}$. The relative position of the shaft to the bearing is defined by distance $O_B\ O_S$, which is called eccentricity *e* and by angle *φ*, which is called attitude angle, and is the angle between the y-axis and the line of centers $O_B$ and $O_S$. To calculate the variation of film thickness the triangle $O_B\ O_S A$, of Figure 10 is shown in detail in Figure 11.

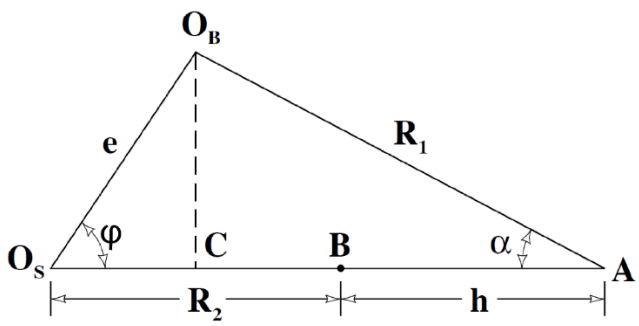


**Figure 11: Details of geometry for the evaluation of film shape in journal bearings [1].**

Observing Figure 11, the following geometric expressions can be derived:

$$O_S A = O_S C + CA = O_S B + BA \tag{43}$$

Or

$$O_S A = e\cos\theta + R_1\cos\alpha = R_2 + h \tag{44}$$

Thus:

$$h=e\cos\theta+R_1\cos\alpha-R_2 \tag{45}$$

Applying the sine rule to (45) gives:

$$\frac{e}{\sin a}=\frac{R_1}{\sin\theta}\Rightarrow\sin\alpha=\frac{e}{R_1}\sin\theta \tag{46}$$

Knowing that $\cos\alpha=\sqrt{1-\sin^2\alpha}=\sqrt{1-(\frac{e}{R_1})^2\sin^2\theta}$ and $\frac{e}{R_1}\ll 1\Rightarrow\cos\alpha\cong 1$, then:

$$h=\varepsilon\cdot\cos(\theta)+R_1-R_2=e\cdot\cos(\theta)+c \tag{47}$$

where:

$c$ is the clearance, i.e. the difference between the radii of bush and shaft ($R_1-R_2$), or:

$$h=c\cdot(1+\varepsilon\cdot\cos(\theta)) \tag{48}$$

where:

$\varepsilon$ is the eccentricity ratio, i.e. the ratio of eccentricity to clearance (*e/c*). The above equation describes the film geometry in journal bearings with an accuracy within 0.1%.

### 2.3.3 Journal bearing calculation using Khonsari equations (based on [1],[17])

For an initial estimation of journal bearing operation, the Khonsari method is a staple choice. Based on the results of Table 1 the Sommerfeld number *S*, the leakage and inlet flow rate $Q_L and\ Q_i$, the minimum film thickness $h_{min}$, the friction force *F*, the power loss $E_p$, and the temperature rise $\Delta T$ can be calculated for given eccentricity of the bearing. Table 1 presents non-dimensional values. The dimensional values for a real application can be calculated using eq. (49)-(55).

**Table 1: Performance parameters for journal bearing with *L/D*=1**

| $\varepsilon$ | $S$ | $\bar{Q}_l$ | $\bar{Q}_i$ | $(R/C)f$ | $\bar{p}_{max}$ | $\theta_{max}$ | $\varphi$ | $\theta_{cav}$ |
|---|---|---|---|---|---|---|---|---|
| 0.05 | 2.7019 | 0.0807 | 1.0375 | 53.4294 | 0.6823 | 99 | 82.18 | 213 |
| 0.1 | 1.3302 | 0.1608 | 1.0739 | 26.4433 | 1.3923 | 105 | 79.40 | 213 |
| 0.15 | 0.8674 | 0.2405 | 1.1092 | 17.3945 | 2.1543 | 111 | 76.63 | 213 |
| 0.2 | 0.6319 | 0.3196 | 1.1434 | 12.8298 | 2.9958 | 117 | 73.86 | 213 |
| 0.25 | 0.4876 | 0.3981 | 1.1766 | 10.0627 | 3.9506 | 120 | 71.06 | 210 |
| 0.3 | 0.3889 | 0.4763 | 1.2087 | 8.1896 | 5.0587 | 126 | 68.25 | 210 |
| 0.35 | 0.3164 | 0.5540 | 1.2396 | 6.8293 | 6.3708 | 129 | 65.42 | 210 |
| 0.4 | 0.2604 | 0.6312 | 1.2696 | 5.7900 | 7.9610 | 135 | 62.56 | 207 |
| 0.45 | 0.2156 | 0.7080 | 1.2985 | 4.9619 | 9.9301 | 138 | 59.65 | 207 |
| 0.5 | 0.1786 | 0.7847 | 1.3262 | 4.2824 | 12.4168 | 141 | 56.69 | 207 |
| 0.55 | 0.1475 | 0.8608 | 1.3529 | 3.7103 | 15.6406 | 144 | 53.65 | 204 |
| 0.6 | 0.1209 | 0.9368 | 1.3785 | 3.2167 | 19.9477 | 147 | 50.52 | 204 |
| 0.65 | 0.0979 | 1.0123 | 1.4030 | 2.7829 | 25.9119 | 150 | 47.27 | 204 |
| 0.7 | 0.0778 | 1.0877 | 1.4264 | 2.3933 | 34.5708 | 156 | 43.83 | 201 |
| 0.75 | 0.0601 | 1.1628 | 1.4487 | 2.0370 | 47.8929 | 159 | 40.19 | 198 |
| 0.8 | 0.0445 | 1.2377 | 1.4697 | 1.7017 | 70.2402 | 162 | 36.20 | 198 |
| 0.85 | 0.0308 | 1.3126 | 1.4893 | 1.3785 | 112.9514 | 165 | 31.72 | 195 |
| 0.9 | 0.0188 | 1.3864 | 1.5100 | 1.0511 | 215.5045 | 168 | 26.40 | 192 |
| 0.95 | 0.0084 | 1.4598 | 1.5277 | 0.6896 | 627.8011 | 171 | 19.32 | 189 |

*Sommerfeld number*

Sommerfeld number is a dimensionless parameter, characterizing bearing performance. It can be calculated using the following equation:

$$S = \frac{\eta N_s D L}{W} (\frac{R}{c})^2 \tag{49}$$

where:

- $\eta$ is the lubricant viscosity (Pa· s)
- $N_s$ is the rotor angular velocity (RPS)
- $D$ is the bearing diameter (m)
- $L$ is the bearing length (m)
- $W$ is the applied load (N)
- $R$ is the bearing radius (m)
- $c$ is the bearing clearance (m)

With the Sommerfeld number and the bearing geometrical characteristics known, eccentricity ratio can be evaluated from Table 1 that contains the numerical solutions for plain $360^o$journal bearings, characterized from L/D=1. Results for different values of L/D can be found in [2].

*Leakage flow rate*

Knowing the dimensionless parameter $\bar{Q}_L$ from Table 1, the leakage flow rate of the lubricant can be calculated using the following equation:

$$Q_L = \bar{Q}_L(\frac{\pi}{2})N_s DLc \tag{50}$$

*Inlet flow rate*

Knowing the dimensionless parameter $\bar{Q}_L$ from Table 1, the inlet flow rate of the lubricant can be calculated using the following equation:

$$Q_i = \bar{Q}_i(\frac{\pi}{2})N_s DLc \tag{51}$$

*Minimum film thickness*

Minimum film thickness can be calculated by the following equation:

$$h_{min} = c(1 - \varepsilon) \tag{52}$$

Minimum film thickness is a crucial performance parameter of the bearing, as it determines the proper functionality of the bearing. This can be done, by checking the minimum film thickness with the minimum allowable film thickness based on a specified surface finish.

*Friction force*

By knowing the dimensionless parameter *(R/c)f* from Table 1, friction coefficient $\mu$ can be calculated. At a next step friction force can be calculated using the following equation:

$$F = \mu W \tag{53}$$

*Power loss*

Power loss (*W*) of the bearing can be evaluated as:

$$E_p = F2\pi RN_s \tag{54}$$

*Temperature rise*

The temperature rise of the lubricant during operation of the bearing can be calculated from the following equation:

$$\Delta T = \frac{E_p}{\rho c_p Q_L} \tag{55}$$

where:

- $c_p$ is the thermal capacity of the lubricant (J/(kg·K))
- $\rho$ is the density (kg/m³)

From Table 1, additional bearing performance parameters can be evaluated, such as angle $\theta_{max}$ at which the maximum pressure occurs, angle $\theta_{cav}$ where cavitation starts and dimensionless maximum pressure $\bar{p}_{max}$.

## 2.4 Surface treatment methods for friction reduction

### 2.4.1 Hydrophobicity (based on [18], [19])

The characteristics attribute of hydrophobic surfaces is their physical property of repelling water, because the molecules of these surfaces tend to be non-polar and as a result they prefer other neutral molecules. This physical property results in very low friction between the liquid and a hydrophobic surface, thus allowing the liquid to slip over the surface. One of the principal parameters that characterizes surface hydrophobicity is the high contact angle, that water droplets exhibit on hydrophobic surfaces, as shown in Figure 12.

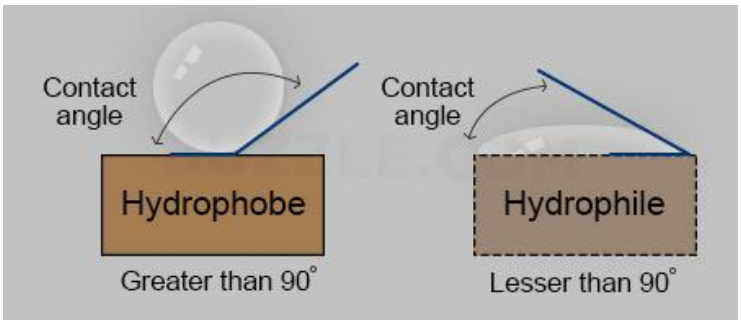


**Figure 12: Contact angle in hydrophobic and hydrophilic surfaces.**

Today, it is possible to construct hydrophobic surfaces in laboratory environments. These surfaces have found use in many industrial applications. As stated earlier, hydrophobicity of a surface can be measured by the shape of a droplet when placed on it. The corresponding parameter is the contact angle between the droplet and the surface.

Reynolds equation assumes non-slip conditions on the fluid-solid boundary, meaning that the fluid velocity next to the wall boundary is equal to the wall velocity. On the other hand, concerning hydrophobic surfaces, proper slip condition in the fluid-soild interface must be considered, taking into consideration that the fluid next to the wall boundary has a different velocity than that of the wall. Fluid velocity at the interface with a hydrophobic boundary depends on a property of the hydrophobic surface, called slip length and it can be calculated using the equation below:

$$u_s = (\tau - \tau_c)\frac{b_s}{h} \tag{56}$$

where,

- $\tau$: the shear stress of the fluid on the fluid-solid interface
- $\tau_c$: the critical shear stress, above which slip occurs
- $\eta$: fluid dynamic viscosity
- $b_s$: slip length

As mentioned earlier, to define how much slippery a surface is when interacting with a certain fluid, the slip length should be evaluated. Slip length is defined as the imaginary length under the surface where fluid velocity would extrapolate to zero. Sometimes, it is more convenient to use the non-dimensional slip length, $b^*$, which is defined as follows:

$$b_s = b^* \cdot H_{ref} \tag{57}$$

From Eq. (57) it derives that, $b^*$, is defined in terms of a constant characteristic geometry parameter of the bearing, $H_{ref}$. For the journal bearing case this parameter is the radial clearance, $c$. So by substituting in (57):

$$b^* = b_s/c \tag{58}$$

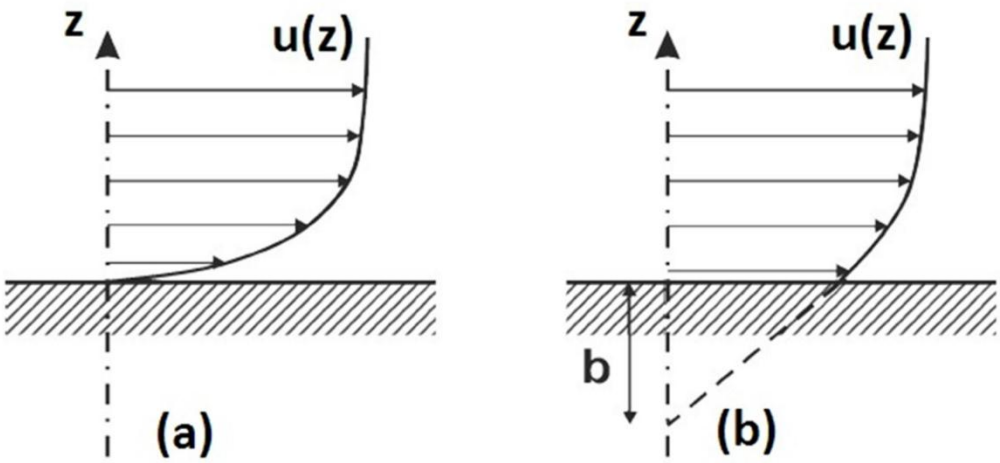


**Figure 13: Velocity profile near the fluid-wall boundary with (a) no-slip condition and (b) slip condition with slip length b [20].**

### 2.4.2 Artificial surface texturing (based on [18], [19], [20], [21])

The term artificial texturing refers to the introduction of deterministic surface micro-structure in the form of microscopic surface features. These features have a repeatable pattern and a regular geometry, coming in the form of rectangular, trapezoidal, cylindrical or spherical shapes, and are used in tribology in order to improve the performance characteristics of lubricated contacts. This happens if artificial texturing is applied properly, as it can have a beneficial effect by increasing the boundaries of hydrodynamic lubrication and by increasing the hydrodynamically generated pressure. Particularly, it contributes in two ways; firstly, it can trap debris that can damage the surfaces in contact, and secondly by acting as a lubricant reservoir, providing oil, especially in mixed lubrication conditions.

In order to evaluate the effects of surface texturing on hydrodynamic lubrication two different approaches can be used. The first consists in solving the Reynolds equation, which is simple and less time-consuming, whereas the second is

concerned with the use of the Navier-Stokes equations; this approach is more accurate, but requires extended computational resources.

Modern such as laser micro patterning advances have enabled more accurate manufacturing of texture patterns, finding use in journal bearings among others. The concept of texturing is illustrated in Figure 14, representing an example of a surface textured with rectangular dimples.

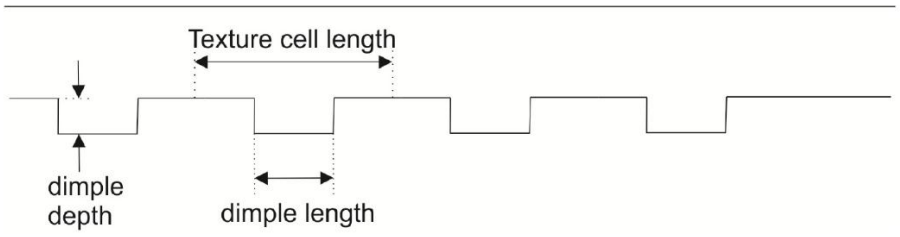


**Figure 14: Sketch of a two dimensional geometry of a parallel slider with artificial surface texturing.**

# 3 Numerical simulations – Optimization of bearing performance

## 3.1 Bearing calculations (based on [2])

An example will be used, to show the process with which the journal bearing performance parameters are evaluated. All the equations used below have already been presented in chapter 2.

**Table 2: Main dimensions of the studied bearing**

| Length (mm) | Diameter (mm) | Radial clearance (mm) |
|---|---|---|
| 30 | 30 | 0.050 |

The main geometric parameters of the bearing are presented in Table 2. The rotor is running at 1000 RPM (=16.667 RPS) and the external vertical load is 1000 N. Bearing clearance has been selected as 50 μm, following the steps below:

First, the mean pressure of the bearing is calculated:

$$p_m = \frac{P_z}{L \cdot D} = \frac{1000N}{30mm \cdot 30mm} = 1.11N/mm^2 = 1.11MPa$$

**From**

Table 3, for $p_m = 1.11\ MPa$ and *N*=1000 RPM, the value for the $\frac{c}{D}$ is 1.4. So for *D*=30 mm, the clearance is estimated as 0.042 mm. For manufacturing reasons radial clearance is selected to be 0.050 mm, so $\Psi = \frac{c}{R} = \frac{0.050}{15} = 0.0033$.

**Table 3: Selection of radial clearance (c/d x1000)**

| Conditions | Rotational speed | | |
|---|---|---|---|
| | Low | Medium | High |
| $p_m$ low | 0.7-1.2 | 1.4-2.0 | 2-3 |
| $p_m$ high | 0.3-0.6 | 0.8-1.4 | 1.5-2.5 |

Sommerfeld number can be now evaluated. For the purposes of this example, the lubricating oil is considered to be Makita Hochleistung-Zweitakt-Motoröl 50:1with inlet temperature 40 $^oC$ (313 K) and a dynamic viscosity of 0.026 Pa·s (or else 26 cps), as shown in Table 6. So, the Sommerfeld number according to Eq. (49) equals to:

$$S = \frac{\eta N_s DL}{W}\left(\frac{R}{c}\right)^2 = \frac{0.026 \cdot 16.66 \cdot 30 \cdot 30}{1000}\left(\frac{15}{0.05}\right)^2 = 0.3510$$

From Table 1 using linear interpolation, the following values can be calculated:

**Table 4: Khonsari parameters for linear interpolation**

| $S$ | ε | $\bar{Q}_l$ | $\bar{Q}_i$ | $(R/c)f$ | $\bar{p}_{max}$ | $\theta_{max}$ | $\varphi$ | $\theta_{cav}$ |
|---|---|---|---|---|---|---|---|---|
| 0.0445 | 0.8 | 1.2377 | 1.4697 | 1.7017 | 70.2402 | 162 | 36.2 | 198 |
| ***0.0351*** | ***0.834*** | ***1.29*** | ***1.48*** | ***1.48*** | ***99.55*** | ***164.06*** | ***33.13*** | ***195.94*** |
| 0.0308 | 0.85 | 1.3126 | 1.4893 | 1.3785 | 112.9514 | 165 | 31.72 | 195 |

The remaining bearing performance parameters can be evaluated, as follows. Minimum film thickness can be calculated using Eq. (48):

$$h_{min} = 0.050\,mm \cdot (1 - 0.834) = 0.00828\,mm = 8.28\,\mu m.$$

According to Table 2 the necessary surface finish for the journal bearing is either 0.1-0.2 µm or 0.2-0.4 µm.

**Table 5: Allowable minimum film thickness [2]**

| Surface finish[a] (*center line avg.* $R_a$) µm | µin. | Description of surface | Examples of manufacturing methods | Allowable minimum *film thickness* µm | µin. |
|---|---|---|---|---|---|
| 0.1–0.2 | 4–8 | Mirror-like surface without toolmarks | Grind, lap, superfinish | 2.5 | 100 |
| 0.2–0.4 | 8–16 | Smooth surface without scratches, close tolerances | Grind and lap | 6.2 | 250 |
| 0.4–0.8 | 16–32 | Smooth surface, close tolerances | Grind and lap | 12.5 | 500 |
| 0.8–1.6 | 32–63 | Accurate bearing surface without toolmarks | Grind, precision mill, and fine tuning | 25 | 1000 |
| 1.6–3.2 | 63–125 | Smooth surface without objectionable toolmarks, moderate tolerances | Shape, mill, grind, and turn | 50 | 2000 |

[a] *Average* Combined conjunction roughness $R_a = 0.5\left(R_{a,\ \text{shaft}}^2 + R_{a,\ \text{bearing}}^2\right)$ (see Chapter 3).
*Source*: ESDU (1967), Hamrock (1994).

As far as the lubricant supply arrangement is concerned, various methods for distributing lubricant within a journal bearing exist, from a supply hole at the inlet to a variety of grooves cut into the bearing internal surface. In the present example the supply hole is placed inside an inlet port at the bearing midplane, opposite to the load line ($\vartheta = -\varphi$), as shown in Figure 15.

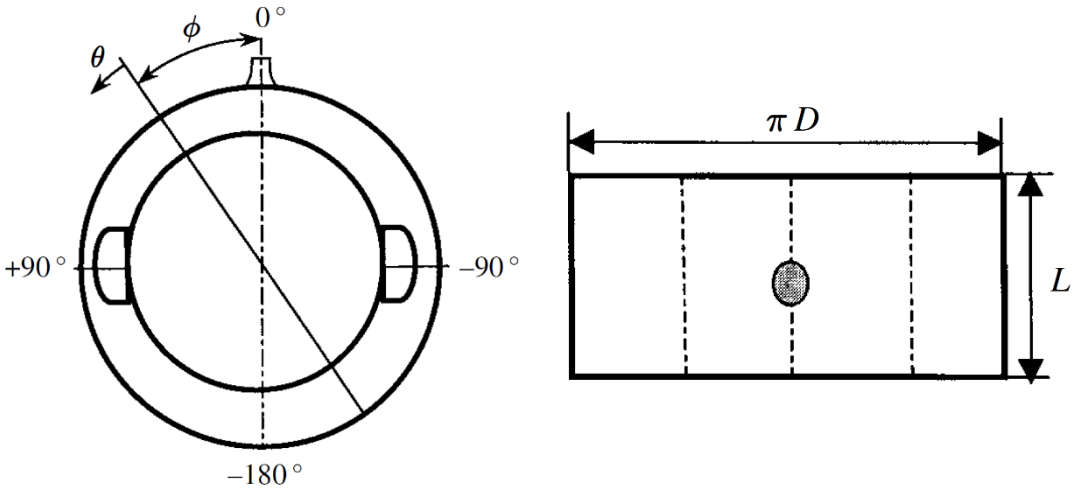


**Figure 15: Supply hole position at $\theta$=-$\varphi$ [2].**

Leakage flow rate $Q_l$ and inlet flow Rate $Q_i$ can be calculated using Eqs (50) and (51):

$Q_L$=1517.905 $mm^3$/s=1.283 gr/s

$Q_i$=1746.4 $mm^3$/s =1.47gr/s.

These values are rough estimates; more accurate values can be calculated following the problem below:

$f_L = 0.834 \cdot 0.7807 = 0.6514$

Following Khonsari ([2], section 8.15, p. 235), leakage flow can be calculated as $Q_L = f_L \cdot \pi \cdot L \cdot D \cdot N_s \cdot c$, where $f_L$ is a correction factor. In the present example, the oil hole is positioned in the unloaded section of the bearing, opposite to the load line so:

$f_L = \varepsilon \cdot f_1$,

where $f_1 = 1 - 0.22 \cdot (L/D)^{1.9} \cdot 0.834^{0.02} = 1 - 0.22 \cdot \frac{30^{1.9}}{30} \cdot 0.843^{0.02} = 0.7807$

Therefore $f_L = 0.834 \cdot 0.7807 = 0.6514$.

$Q_L = 0.6514 \cdot \pi \cdot 30 \cdot 30 \cdot 16.667 \cdot 0.050 = 1534.1 \ mm^3/s$

In order to determine the pressure-induced flow $Q_P$, specification of the position, geometry, and supply pressure at the inlet port is required. The used equation in this case is the following:

$Q_p = f_g \cdot (\frac{h_g}{c})^3 \cdot \frac{P_s \cdot c^3}{\mu_i}$, where $P_s$ is the supply pressure, which in our case is set to 2 bar, and $\mu_i$ is the lubricant viscosity at the inlet temperature. Parameter $f_g$ is a function

of the oil hole and $\frac{h_g}{c}$ is the non-dimensional film thickness at the inlet port. The parameter $f_g$ can be determined as follows:

$$f_g = 0.0675 \cdot (\frac{D_H}{L} + 0.4)^{1.75},$$

where $D_H$ is the diameter of the inlet hole and is set at 4mm.

Therefore, $f_g = 0.0675 \cdot (\frac{4}{30} + 0.4)^{1.75} = 0.22467$

Film thickness parameter $(\frac{h_g}{c})$ equals to $(\frac{h_g}{c})^3 = \left(1 + \varepsilon \cdot cos\varphi^3\right) = \left(1 + 0.843 \cdot cos\left(33.13\right)^3\right) = 0.373$

.

The supply pressure is set at 2 bar=200000 Pa, therefore, pressure-induced flow equals to:

$$Q_p = 0.2247 \cdot 0.373 \cdot \frac{200000 \cdot 0.050^3}{0.026} = 81.58 \ \ mm^3 / s$$

Total leakage can be calculated using the following equation: $Q_m = Q_L + Q_P - 0.3\sqrt{Q_P \cdot Q_L} = 1509.55 \ \ mm^3 / s$

For an oil hole positioned in the unloaded section of the bearing, opposite to the load line:

$Q_{L,total} = Q_m^S \cdot Q_P^{1-S}$, where S'=0.6 for an oil hole of diameter $D_H$=4 *mm* and for $D_H / L = 0.1 - 0.25$ (in our example $D_H$/L=0.133). So the corrected total leakage equals to:

$$Q_{L,total} = 469.85 mm^3 / s = 28191.2 mm^3 / \min = 28.91 ml / \min \ .$$

The density of the lubricant is known at 40 $^oC$ (313 K) and is ρ=0.8454 gr/$cm^3$.

The above calculations were used to estimate total oil leakage. In our example, we assumed that oil was to be fed at a pressure of 2 bar.

Friction coefficient is estimated from Table 1. For ε=0.843 we have $(\frac{R}{c}) f = 1.48$, therefore $f = 1.48 \cdot \frac{c}{R} = 1.48 \cdot \frac{0.050}{15} = 0.004933$. Power loss is evaluated using the following expression:

$$E_P = FU = f \cdot W \cdot \left(2\pi \cdot R \cdot N_S\right) = 7.745W \ .$$

From the definition of thermal diffusivity we have $pc_P = k / a_i = 1.28 Ws / (m^3 K)$ .Therefore, oil temperature rise is estimated to be

$$\Delta \mathrm{T} = \frac{E_P}{(p \cdot c_p \cdot Q_{L,total})} = 12.8 \text{ K} \cdot$$

## 3.2 Multiobjective optimization and Pareto front (based on [22], [23], [24],[26])

Genetic algorithms are numerical search tools that are to find the global maximum or minimum of an objective function. The objective function may be of one or more variables and subject to various constraints. Genetic algorithms mimic the process of natural selection, during their solving process, by using a set of binary digits, 1 and 0, called chromosomes. For every argument of the objective function, each string is divided in various substrings that have a certain length. In a relevant manner chromosomes are divided into genes. The total number of genes form the genotype of the chromosome.

In order for the genetic algorithm to start the solving process an initial population of chromosomes is created by randomly allocating the bits of all the strings. After that the genetic algorithm uses the chromosomes to create an arrangement of populations. The individuals of the current generation are the parents, and after undergoing certain operations they produce the individuals of the next generation, called the children. It must be noted that some parents are moved to the next generations intact. The solving sequence of the genetic algorithm is that at every step, the previous population uses its strings in order to create a new population that would probably have a better mean fitness value and it continues until a termination criterion is reached. The string manipulation depends on selecting various pairs of chromosomes and then mating them in order to use the newly created chromosomes for the formation of the next population. This selecting and mating process of the chromosomes is based on four fundamental operations: reproduction, crossover, replacement and mutation. All of the mentioned operations are based on random sampling.

*Crossover* is the operation that exchanges genes between the chromosomes of the two parents, usually in a random manner. Thus, the produced child can have genes from both parents; the basic concept of crossover can be visualized in Figure 16.

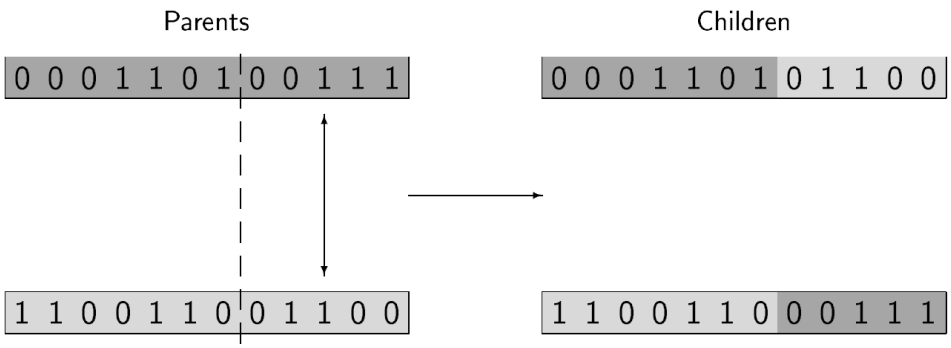


**Figure 16: Crossover operation [26][25].**

*Mutation* operation offers the advantage of preserving genetic diversity, resulting in surpassing local maxima. It is achieved by randomly altering the bit strings with a certain probability. The basic concept of mutation can be seen in Figure 17.

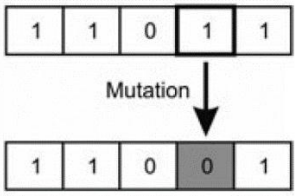


**Figure 17: Mutation operation [26].**

A genetic algorithm is used because it offers certain advantages over other optimization methods. One of these advantages is that genetic algorithms do not manipulate the parameters of the optimization problem themselves, but instead they use coded versions of the problem parameters. A second advantage is that while other methods use a single point to search, genetic algorithms always search on a whole population of points. This search technique minimizes the risk of the genetic algorithm to be trapped in a local stationary point, thus improving the chance of finding the global optimum. To this end, a higher value of mutation probability could further increase that chance, but not a too high one, because the good characteristics of the generations would be eventually lost. A third advantage that genetic algorithms provide is that they can be applied to almost every kind of continuous or discrete optimization problem.

To continue with the analysis of genetic algorithms, many modern problems come with two or more objectives that require optimization. These multiple objectives may be contradicting but at the same time they have to be optimized simultaneously. In this case, the concept of multiobjective optimization is used. While in single objective optimization problems the search space is well defined, in multiobjective optimization problems the search space is partially ordered, since instead of a single optimal solution, there is a group of possible ones, and the final solution will be obtained by eventually choosing one of them, depending on the external constraints of each problem.

In multi-objective optimization problems, a vector of design variables $\vec{x}$ is sought, which satisfies *m* constraints (included in a vector $\vec{g}$) and minimizes a vector $\vec{f}$, with *k* objective functions. An optimization problem can thus be formulated as follows:

$$\begin{Bmatrix} \min \vec{f}(\vec{x}) = (\vec{f_1}(\vec{x}), \vec{f_2}(\vec{x}), \dots, \vec{f_k}(\vec{x}))^T \\ \vec{x} \in X = \{\vec{x} \in \Re^n\} \\ g_j(\vec{x}) \leq 0, j = 1, \dots, m \end{Bmatrix}$$

Objective and constraints functions are functions of the design variables:

$$\begin{Bmatrix} f_i(\vec{x}) = f_i(x_1, x_2, \dots, x_n), i = 1, \dots, k \\ g_j(\vec{x}) = g_j(x_1, x_2, \dots, x_n), j = 1, \dots, m \end{Bmatrix}$$

In multi-objective minimization methodologies, we commonly seek *Pareto optimal (or dominant) solutions*, as shown in Figure 18. A solution $\vec{x}_1$ is defined as *dominant* over $\vec{x}_2$ when:

$$f_i(\vec{x}_1) \leq f_i(\vec{x}_2)\ \forall i = 1, \dots, k\ and$$

$$f_i(\vec{x}_1) < f_i(\vec{x}_2)\ \exists i = 1, \dots, k$$

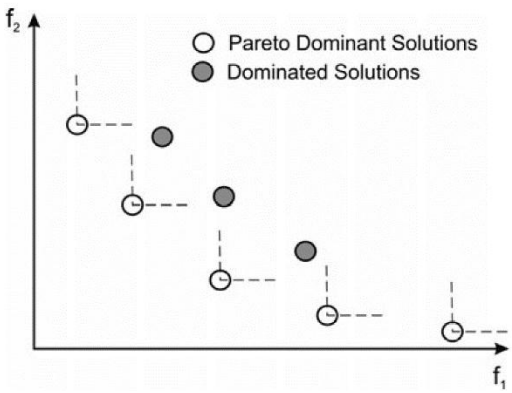


**Figure 18: Sketch of Pareto front for a case with two objective functions.**

The collection of all non-dominated solutions is the *Pareto front,* shown in Figure 18 for the case of two objective functions (k=2).

## 3.3 Numerical approach-reference case (based on [25], [26], [27] , [28])

For the numerical purposes of the present study, an in-house code was used, developed in [20]. The code is used to evaluate the performance indices of a journal bearing under steady-state or transient loading. In order to run a certain simulation, the following input information must be filled in in the appropriate *input.txt* file.

- Journal bearing dimensions: length *L*, diameter *D*, radial clearance *c*
- Rotational speed: *N*
- Lubricant viscosity: *η*
- Vertical / Horizontal load: $P_z, P_x$
- Grid size: $D_{div}/L_{div}$

There are also several options concerning the selection of the appropriate solver for each different problem. More specifically, an option exists to replace the classic Reynolds equation solver with the Reynolds solver appropriately modified to account for slip-wall boundary conditions.

The output results for a typical steady-state solution are as follows:

- Sommerfeld Number, *S*
- Dimensionless eccentricity ratio, *ε*
- Attitude angle, *φ*
- Non-dimensional Load Capacity
- Normalized friction Coefficient, *f*
- Vertical Load [N]
- Horizontal Load [N]
- Maximum Pressure [Pa], $P_{\max}$
- Minimum film thickness [m], $h_{min}$
- Inlet Flow rate, [lt/min], Non-dimensional value, $Q_i$
- Side Flow rate leakage, [lt/min], Non-dimensional value, $Q_l$
- Power loss [kW], *E*
- Friction torque $[\mathrm{kN\cdot m}]$

Here the bearing geometric characteristics are that of Table 2. The numerical approach took place for 3 separate steady loads, namely 200 N, 500 N and 1000 N. The rotating speed of the shaft was considered constant; two different values namely 500 RPM and 1000 RPM have been considered.

For the lubrication of the bearing the lubricant oil that was taken into consideration is the Makita Hochleistung-Zweitakt Motoröl 50:1, and is the lubricant that is used in the experimental measurements. The lubricant temperature is set to $40^{o}C$ with a density of $0.8454 g/cm^3$. All of its properties are shown in Table 6.

The bearing used for the numerical simulations had its main dimensions set as close to the real bearing as possible. Also the combination of the applied loads and rotational speeds were set to be as close as possible to the relative combinations that would take place during the experiments.

**Table 6: Lubricating oil Makita Hochleistung-Zweitakt-Motoröl 50:1. Dynamic viscosity, kinematic viscosity and density at $20^{o}C$, $30^{o}C$, $40^{o}C$ and $100^{o}C$**

| Temperature ($^{o}$C) | Dynamic viscosity (mPa·s) | Kinematic viscosity (mm$^2$/s) | Density (g/cm$^3$) |
|---|---|---|---|
| 100 | 5.3015 | - | - |
| 40 | 25.765 | 30.476 | 0.8454 |
| 30 | 48.095 | 40.975 | 0.8520 |
| 20 | 81.374 | 69.808 | 0.85 |

### 3.3.1 Mesh study

A mesh study is conducted in order to decide the number of the numerical grid points along the x (circumferential) and y (axial) directions. A variation of different grid sizes has been examined, and the computed dimensionless eccentricity ratio and normalized friction coefficient are compared to those corresponding to a very fine grid, here being 301x301 grid. The chosen grid sizes are: 11x11, 21x21, 51x51, 101x101 and 201x201.

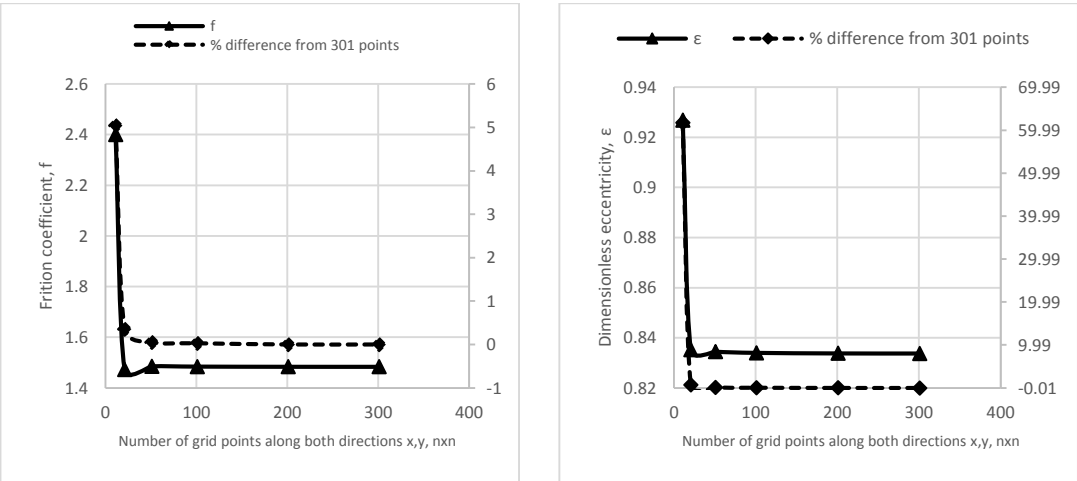


**Figure 19: Mesh study of the plain journal bearing at 1000 N load and rotational speed of the shaft at 1000 RPM. The parameters evaluated are: normalized friction coefficient '$f$', dimensionless eccentricity '$\varepsilon$' and their percentage difference from those corresponding to the maximum grid size.**

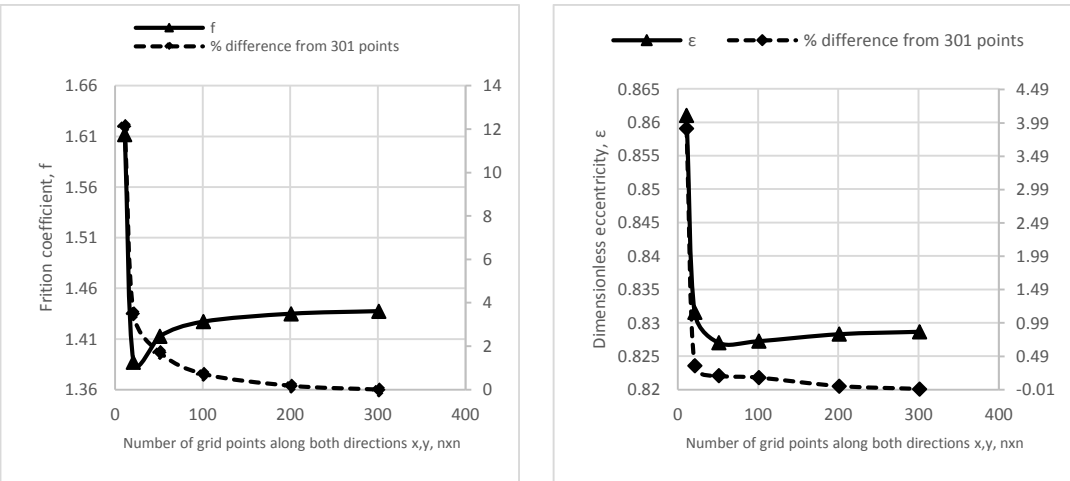


**Figure 20: Mesh study of the hydrophobic journal bearing at 1000 N load and rotational speed of the shaft at 1000 RPM The parameters evaluated are: normalized friction coefficient '$f$', dimensionless eccentricity '$\varepsilon$' and their percentage difference from those corresponding to the maximum grid size.**

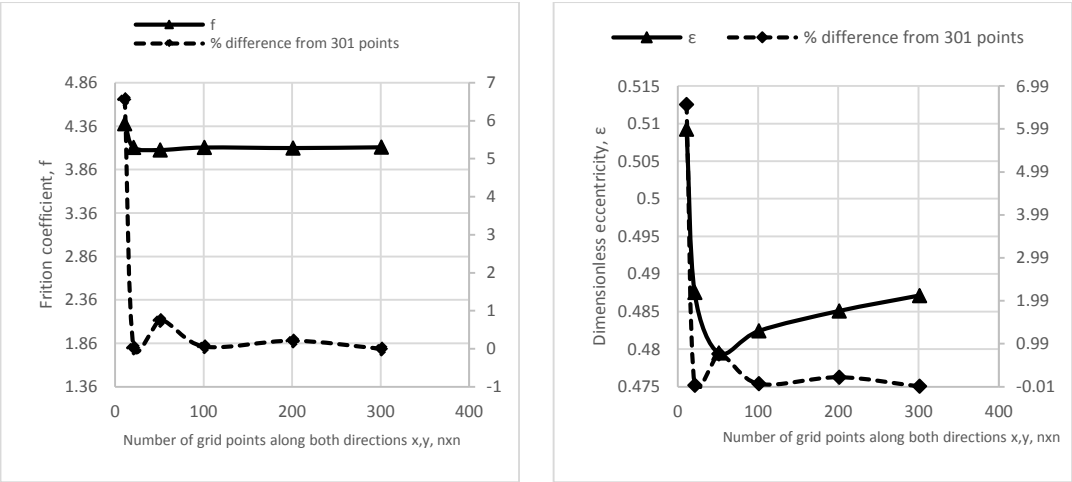


**Figure 21: Mesh study of the textured journal bearing at 200 N load and rotational speed of the shaft at 1000 RPM. The parameters evaluated are: normalized friction coefficient '$f$', dimensionless eccentricity '$\varepsilon$' and their percentage difference from those corresponding to the maximum grid size.**

From Figure 19-Figure 21 it is clear that grids larger than 101x101 points generate an infinitesimally different result, so the grid size of 101x101 points along both directions is selected, without adding any significant error and at the same time greatly reducing the computational time.

### 3.3.2 Steady state

The bearing with plain (conventional) and textured surfaces was tested for different applied loads (200 N, 500 N, 1000 N). The plain bearing cases were used as a reference case, for optimizing the bearing surface texturing. The bearing performance indices that are used for optimization are the dimensionless eccentricity ratio and the normalized friction coefficient. So, the reference cases for the applied loads are presented in the following tables:

**Table 7: Reference cases of plain bearing for rotational speed of 1000 RPM and applied loads of 200 N, 500 N and 1000 N.**

| **Reference Case No.** | 1 | 2 | 3 |
|---|---|---|---|
| **Applied load (N)** | 200 | 500 | 1000 |
| **Rotational speed (RPM)** | 1000 | 1000 | 1000 |
| **Dimensionless eccentricity ratio** | 0.5048 | 0.721 | 0.834 |
| **Normalized friction coefficient** | 4.223 | 2.242 | 1.485 |

**Table 8: Reference cases of plain bearing for rotational speed of 500 RPM and applied loads of 200 N, 500 N and 1000 N.**

| Reference Case No. | 1 | 2 | 3 |
|---|---|---|---|
| **Applied load (N)** | 200 | 500 | 1000 |
| **Rotational speed (RPM)** | 500 | 500 | 500 |
| **Dimensionless eccentricity ratio** | 0.675 | 0.834 | 0.906 |
| **Normalized friction coefficient** | 2.588 | 1.485 | 1.015 |

## 3.4 Numerical simulations and optimization of the bearing performance (based on [18], [25], [26], [27], [28])

The bearing solver described in section 3.3 was coupled with a two-objective optimization code using the Matlab built-in optimizer.

As mentioned in the introduction, two surface treatments are studied and thus bearing optimization is conducted separately for artificial texturing and hydrophobicity at parts of the interacting surfaces.

Concerning artificial texturing, seven (7) optimization design parameters have been selected:

1. *start_x* is the angle at which texturing starts on x axis (circumferential direction)
2. *end_x* is the angle at which texturing ends on x axis (circumferential direction)
3. *density_x* is the density of the surface that contains textures along x axis (circumferential direction)
4. *start_y* is the non-dimensional value of the bearing length at which texturing starts on y axis (axial direction)
5. *end_y* is the non-dimensional value of the bearing length at which texturing ends on y axis (axial direction)
6. *density_y* is the density of the surface that contains textures along y axis (axial direction)
7. *depth* is the depth of the textures in both axis

$N_{x,}N_y$ are the number of dimples in the x-axis (circumferential direction) and y-axis (axial) directions, respectively (their values are constant for each textured bearing)

All of the optimization parameters are shown in Figure 22.

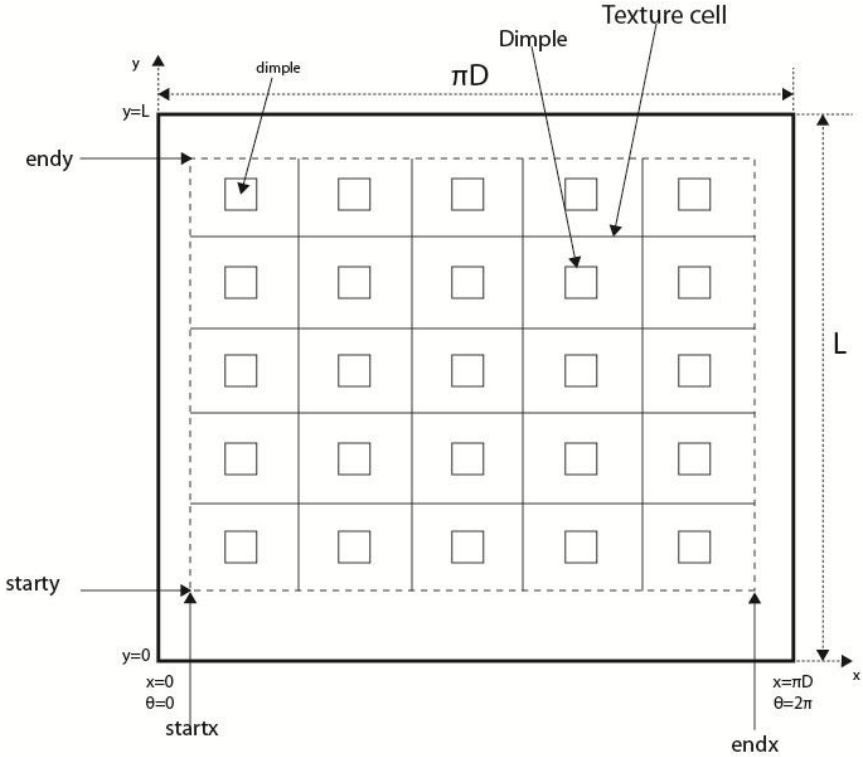


**Figure 22: Design parameters of the textured journal bearing.**

*Density x* and *density y* are defined as the ratio of the dimple length to the texture cell length along the x and y axes, respectively, as seen in Figure 14. The *depth* of each dimple is also shown in Figure 14.

For the hydrophobic bearings, 4 design parameters are taken into consideration:

1. *slip_start_angle* is the angle at which hydrophobicity starts on x axis (circumferential direction)
2. *slip_end_angle* is the angle at which hydrophobicity ends on x axis(circumferential direction)
3. *slip_start_y* is the non-dimensional value of the bearing length at which hydrophobicity starts on y axis (axial direction)
4. *slip_end _y* is the non-dimensional value of the bearing length at which hydrophobicity ends on y axis (axial direction)

The design parameters of the hydrophobic bearing are shown in Figure 23.

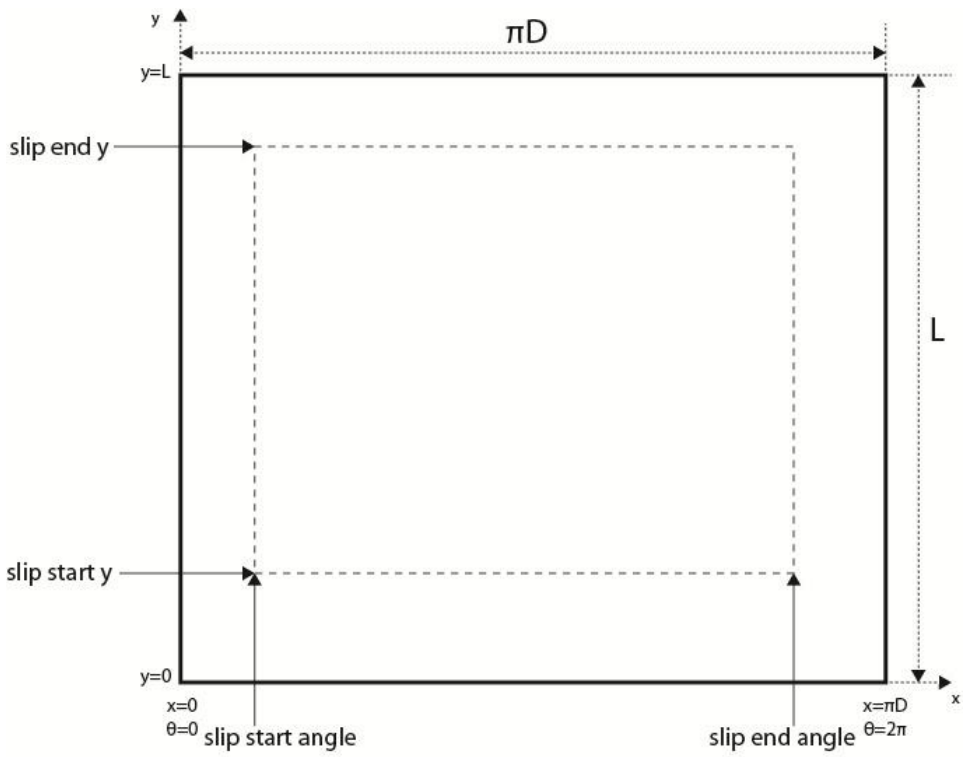


**Figure 23: Design parameters of the hydrophobic journal bearing.**

The optimization will take place for combinations of two parameters:

- the applied load to the bearing, with values of 200 N, 500 N and 1000 N
- the rotational speed of the shaft, with values of 500 RPM and 1000 RPM

The optimization aims at minimizing the normalized friction coefficient and at maximizing lubricant film thickness, with the latter being equivalent to minimizing dimensionless eccentricity ratio. The expressions for calculated normalized friction coefficient and dimensionless eccentricity ratio are presented hereafter:

- $f = \mu \cdot \left(\frac{R}{c}\right)$, where $\mu = \frac{F}{W} = \frac{\int_0^L \int_0^B \tau dx dy}{W}$
- $h = c \cdot (1 - e)$, where $\varepsilon = \frac{e}{c}$

As stated earlier, optimization is performed for two surface treatments, that of artificial surface texturing and hydrophobicity. Regarding artificial texture patterns, four different types of journal bearings of the same principal dimensions have been evaluated: (a) a pocket bearing (one texture cell in the circumferential dimension and one texture cell in the axial direction, 1x1), (b) a bearing with five circumferential grooves (c) a bearing with five radial grooves (1x5) and (d) a bearing with rectangular dimples (five textures cell in the circumferential dimension and five texture cells in the axial direction, 5x5). The same process will be conducted for bearings with hydrophobic surfaces. Two different types of hydrophobic surfaces have been evaluated: (a) hydrophobic surfaces with slip length b*=0.1 and (b) hydrophobic surfaces with slip length b*=1.

To this end, a main Matlab script, initiating the optimization procedures, and two separate Matlab functions, each one for a different surface treatment were developed, both calling the same executable file (*bearing solver,* section 3.3), but with different input data.

The built-in Matlab function that finds minima using a genetic algorithm is the *gamultiobj* function.

*[x,fval] = gamultiobj(FitnessFunction,numberOfVariables,[],[],[],[],LB,UB,options);*

Specifically it finds the Pareto front (section 3.2) of the objective function `FITNESSFCN`. NVARS is the number of design variables, as they have been described in section 3.4. The fitness functions that are used are *bearing_2Obj_Fun_Textures* for the artificial texturing case and *bearing_2Obj_Fun_Slip* for the hydrophobic case. The number of variables is set as 7 and 4 for artificial texturing and hydrophobicity, respectively. Linear equalities and linear inequalities have not been used in our case, so a symbol of *[]* has been used. Boundary constraints for both cases are shown in Table 9 and Table 10.

**Table 9: Upper and lower boundaries of the parameters for textured surfaces.**

| Design parameter for textured bearings | Lower Boundary | Upper Boundary |
|---|---|---|
| ***start_x* (deg)** | 10 | 105 |
| ***end_x* (deg)** | 105 | 200 |
| ***density_x*** | 0.2 | 0.8 |
| ***start_y* (deg)** | 0.02 | 0.4 |
| ***end_y* (deg)** | 0.6 | 0.98 |
| ***density_y*** | 0.2 | 0.8 |
| ***depth* (μm)** | 5 | 90 |

**Table 10: Upper and lower boundaries of the parameters for hydrophobic surfaces.**

| Parameters for hydrophobic surfaces | Lower boundary | Upper boundary |
|---|---|---|
| **slip_start_angle (deg)** | 10 | 105 |
| **slip_end_angle (deg)** | 105 | 200 |
| **slip_start_y** | 0.1 | 0.4 |
| **slip_end_y** | 0.6 | 0.9 |

Specific options for the genetic algorithm can be created with the *gaoptimset* function, an example of which is shown just below:

*options='gaoptimset('PlotFcns',{@gaplotpareto,@gaplotscorediversity},'Generations',40,'PopulationSize',40)'.*

Parameter *'PlotFcns'* is used to plot various quantities during simulation and in our case it plots two quantities: *@gaplotpareto and @gaplotscorediversity,* where gaplotpareto plots a Pareto front for the two objectives, and *gaplotscorediversity* plots a histogram of the scores of the current generation. The other two parameters are the *generations* and *populationsize,* which state the maximum number of generations allowed and the number of individuals each generation contains, respectively. In our case both parameters are set to be 40, which means a maximum size of 40 generations, with 40 individuals in each generation.

There is also the option to select a certain criterion, that when met the optimization loop stops. In our case, a total amount of 40 generations was used, and each generation contained a population of 40 individuals. So, in total, each optimization problem required a total of 1600 different solutions. Each solution is saved in a text file, so after each different case is solved, it can be accessed and processed, accordingly.

The only disadvantage found by using the above Matlab functions, is that the Pareto front was only generated as a *Matlab .fig* file, and that there was no method to distinguish the non-dominant solutions from the total amount of solutions, 1600 in our case, and save them in a separate text file for further use, followed by their respective geometry (set of design variables). Therefore, an external Matlab function is called after the creation of the Pareto-optimal set, in order to access the Pareto points values and write them in a text file. After that, with the Pareto point values of dimensionless eccentricity ratio and normalized friction coefficient fully known, it is feasible to assign each solution to its respective geometry.

The above solving process using Matlab is depicted in Figure 24.

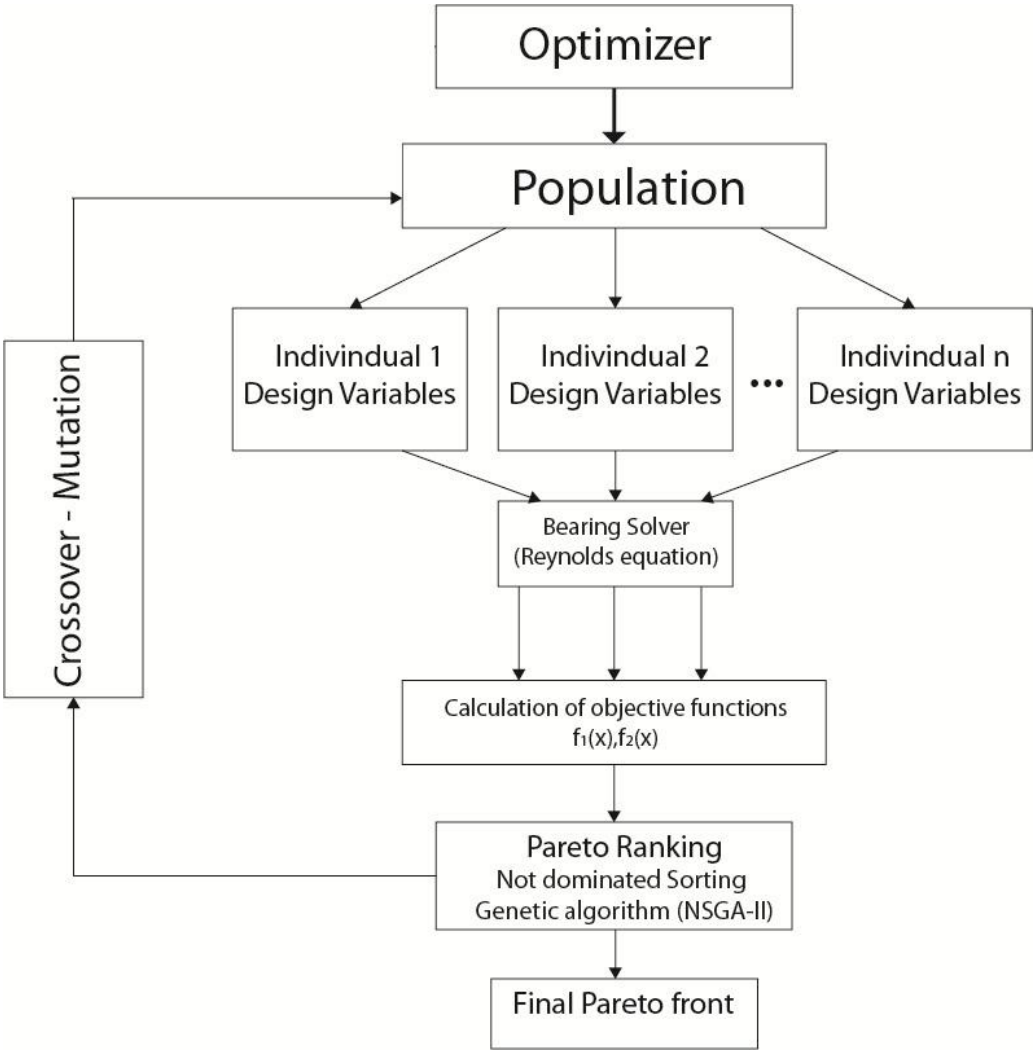


**Figure 24: Optimization procedure.**

Finally, another Matlab script was utilized for post processing of the results. It was used to visualize the fluid film geometry (film thickness, *h*), and to plot the resulting pressure distribution, for bearing designs selected by the user.

### 3.4.1 Plain journal bearing: numerical simulations

In this section simulations for the plain journal bearing are performed, for three representative values of vertical load, from 200 N to 1000 N and for two values of rotational speed, namely 500 RPM and 1000 RPM. In Table 11, various operating characteristics are presented in detail for the eight different considered loading conditions.

**Table 11: Reference journal bearing design: Performance indices for different operating conditions of the bearing.**

| **Shaft speed, *N*** | 500 RPM | | | 1000 RPM | | |
|---|---|---|---|---|---|---|
| **$P_z$ (N)** | 200 | 500 | 1000 | 200 | 500 | 1000 |
| **Sommerfeld Number, *S*** | 0.08775 | 0.0351 | 0.01755 | 0.1755 | 0.0702 | 0.0351 |
| **Dimensionless eccentricity ratio, $\varepsilon$** | 0.674783 | 0.83404 | 0.906141 | 0.504825 | 0.720992 | 0.834065 |
| **Attitude angle, $\varphi$ (deg)** | 45.5885 | 33.2928 | 25.6792 | 56.4238 | 42.3855 | 33.2973 |
| **Non-dimensional Load Capacity, $W^*$** | 0.189957 | 0.474834 | 0.949957 | 0.0949668 | 0.237412 | 0.47483 |
| **Normalized friction Coefficient, $f$** | 2.58772 | 1.4846 | 1.01514 | 4.2233 | 2.24261 | 1.48473 |
| **Maximum Pressure (Pa), $P_{max}$** | 578914 | 1.86039e+06 | 4.55202e+06 | 494124 | 1.53489e+06 | 3.72152e+06 |
| **Angle of maximum pressure (deg), $\theta_{max}$** | 16.7885 | 15.2928 | 14.8792 | 16.8238 | 17.1855 | 15.2973 |
| **Minimum film thickness (m), $h_{min}$** | 1.62608e-05 | 8.29799e-06 | 4.69297e-06 | 2.47588e-05 | 1.39504e-05 | 8.29674e-06 |
| **Power loss (Kw) (N), $E_p$** | 0.0013551 | 0.00194334 | 0.00265844 | 0.00442263 | 0.00587101 | 0.00777397 |
| **Inlet Flow rate, Non-dimensional value, $\overline{Q}_i$** | 1.41861 | 1.48373 | 1.49966 | 1.32873 | 1.43584 | 1.48374 |
| **Side Flow rate, Non-dimensional value, $\overline{Q}_l$** | 1.05673 | 1.2926 | 1.38941 | 0.793735 | 1.12161 | 1.29186 |
| **Friction torque (kN m), *F*** | 2.58805e-05 | 3.71151e-05 | 5.07725e-05 | 4.22319e-05 | 5.60599e-05 | 7.42304e-05 |

From Table 11, it is derived that minimum film thickness is directly related to bearing load: an increase in bearing load results in decreased film thickness. On the other hand, dimensionless eccentricity ratio increases with increasing bearing load. Another important factor, namely the normalized friction coefficient behaves equivalently to minimum film thickness. The above are shown in Figure 25 and in Figure 26, in which the effect of rotor speed is also clarified: higher rotational speeds lead to higher dimensionless eccentricity ratio values and to decreased values of minimum film thickness and normalized friction coefficient.

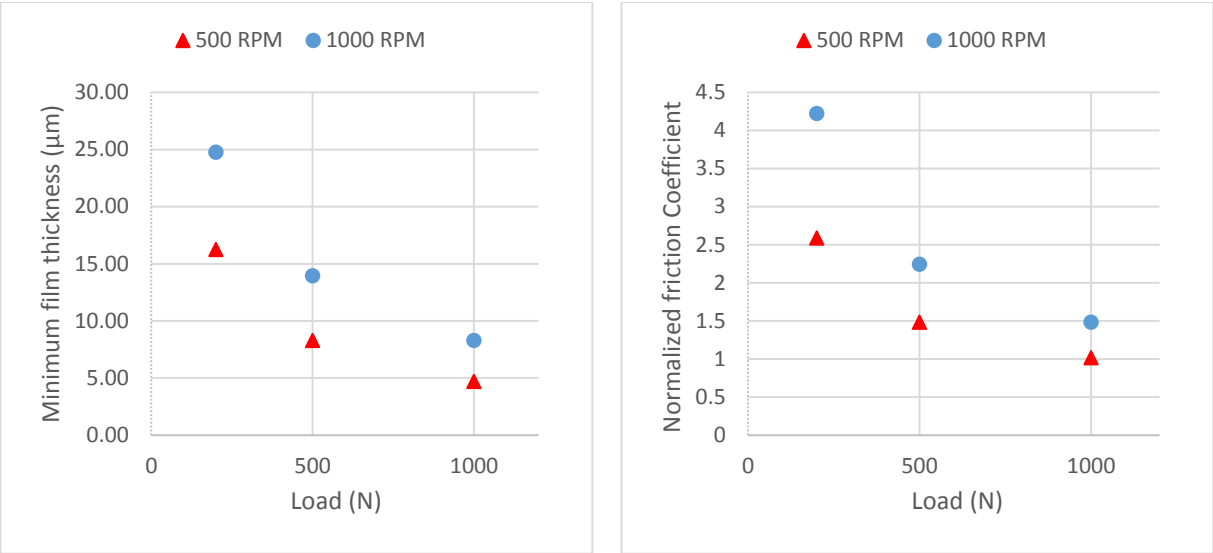


**Figure 25: (a) Minimum film thickness, $h_{min}$, and (b) Normalized friction coefficient, f, versus specific bearing load for two different values of rotational speed.**

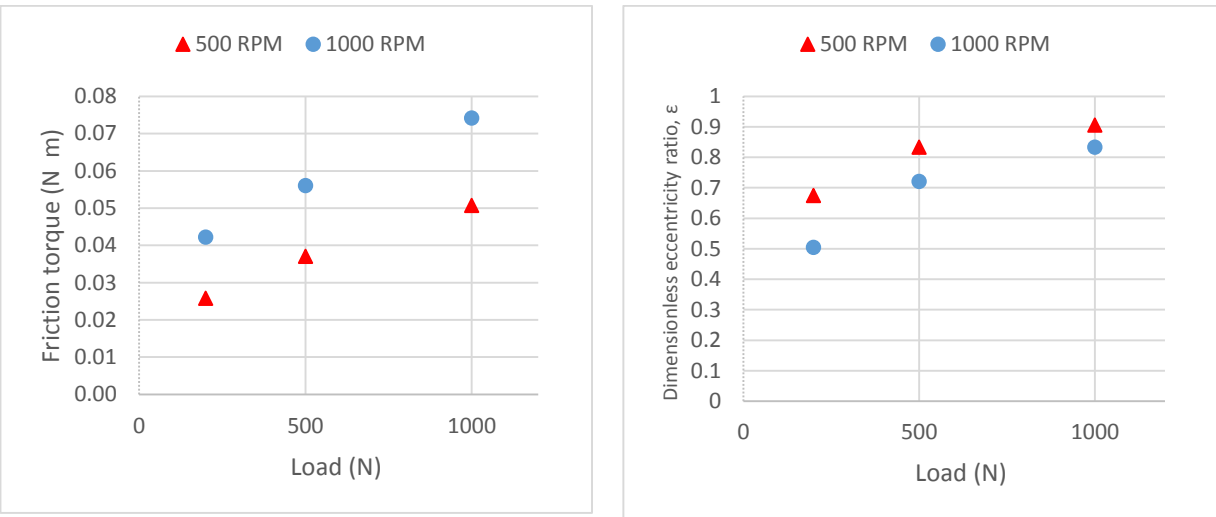


**Figure 26: (a) Friction torque, $M_f$, and (b) dimensionless eccentricity ratio, ε, versus specific bearing load for two different values of rotational speed.**

## 3.5 Bearings with textured surfaces/ hydrophobicity

Many modern bearing designs use certain modifications to their surfaces, such as texture and hydrophobicity. Artificial surface texturing serves by increasing the hydrodynamically generated pressure, traps debris that can damage the working surfaces, and act as a lubricant reservoir, providing oil, especially in mixed lubrication conditions, where local oil starvation prevails. The most common artificially textured bearings that have been studied in the recent literature are bearings with axial grooves, circumferential grooves and rectangular/ spherical dimples.

The objective of the present section is the cross-evaluation of journal bearings with different texture patterns, in comparison to the reference plain (conventional) bearing presented in section3.4.1, under similar operating conditions. The ultimate goal is to find appropriate texture patterns that provide enhanced performance characteristics. The textured and hydrophobic cases and their names are presented in Table 12 and Table 13.

At this point it is useful to add that in the Pareto front diagrams, the reference case point is shown as an orange x, while the whole of the optimization solution points are shown as blue crosses. The Pareto front points are shown as red dots.

**Table 12: Textured bearings studied in the present work.**

| Number of dimples in circumferential direction | Number of dimples in axial direction | Case name |
|---|---|---|
| 1 | 1 | T,1,1 (pocket bearing) |
| 5 | 1 | T,5,1 (bearing with circumferential grooves) |
| 1 | 5 | T,1,5 (bearing with axial grooves) |
| 5 | 5 | T,5,5 (bearing with rectangular dimples) |

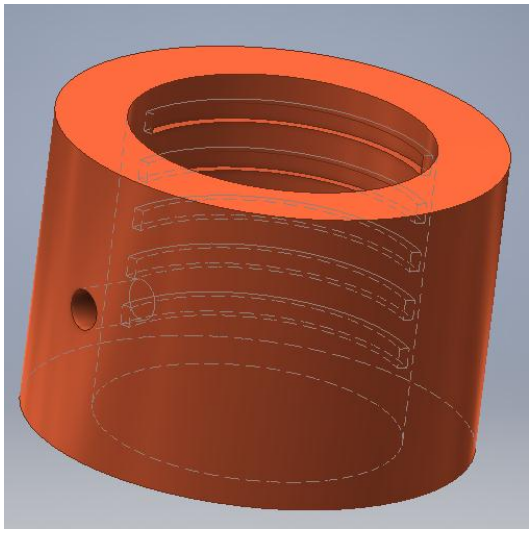

(a)

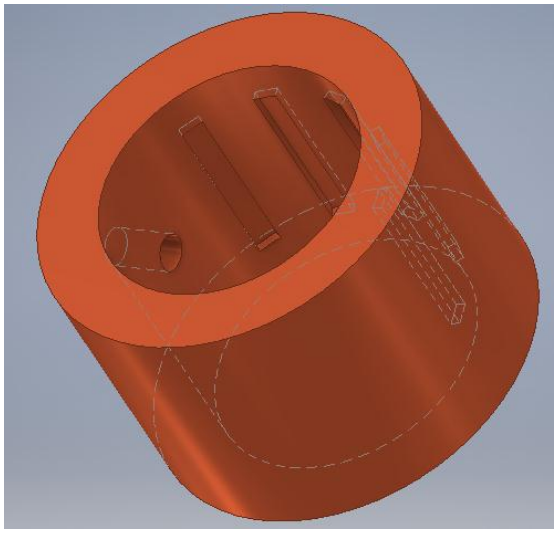

(b)

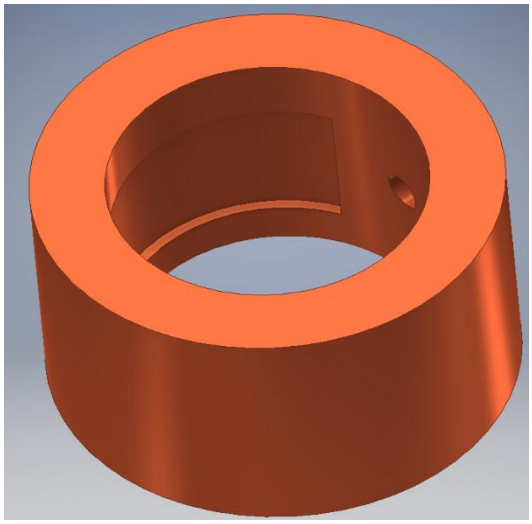

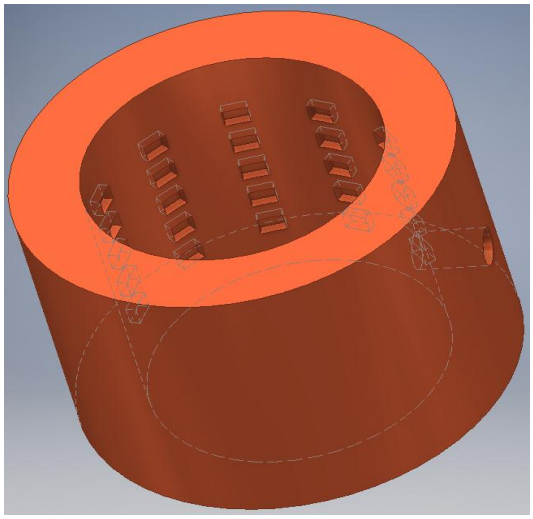

(c) (d)

**Figure 27: Example of bearing geometry for textured bearings (a) T,5,1, (b) T,1,5, (c) T,1,1, (d) T,5,5 .**

**Table 13: Hydrophobic bearings studied in the present work**

| Slip length, *b** | Case name |
|---|---|
| 0.1 | H,0.1 |
| 1 | H,1 |

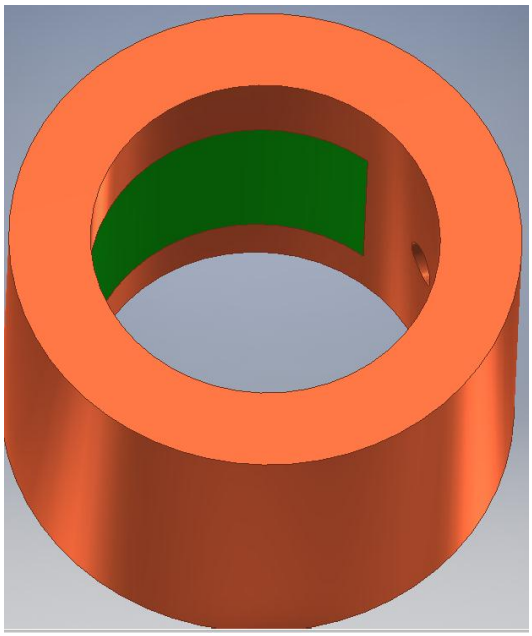

**Figure 28: Hydrophobic bearing.**

In axially grooved bearings, a groove of length $L_g$ extends axially from the bearing midplane, to either side of the bearing. In typical uses the total groove length is about 80% of the bearing length, leaving l=0.1 L on either side. The minimum width of the depth region should be at least one-tenth of the diameter, $w_g = D/10$, with a depth of D/30. An axial groove is useful for better distributing oil over the entire length of the bearing and to better control the rise of its temperature. For a steadily loaded bearing with a length of about 25-50 mm a bearing with axial grooves is more suitable for better lubricant distribution, than a bearing with a simple supply hole. The selection of the optimum artificially textured geometry is decided based on the optimal values of dimensionless eccentricity ratio and normalized friction coefficient.

### 3.5.1 Bearings with textured surfaces

In Table 14 and Table 15, the simulation results regarding textured bearings are presented. Table 14 presents results corresponding to rotational speed of 1000 RPM, whereas in Table 15, results corresponding to rotational speed of 500 RPM are presented.

For each value of rotational speed, three different values of bearing load are simulated. At the first column of each Table, the name of the studied case is presented (naming conventions have been presented in Table 12). In the middle column of each Table, the Pareto fronts of each optimization problem are presented (large dots), along with non-dominating solutions of the optimization process (cross symbols), and the performance of the reference (plain) bearing (large X symbol).

It is observed that, in all cases, a substantial reduction of normalized friction coefficient and dimensionless eccentricity ratio is achieved at low values of bearing load (200 N). The bearings are in that case moderately loaded (eccentricity ratio approximately 0.5 to 0.65). At higher values of bearing load (500 N, 1000 N) the improvement is only marginal. Further, it is observed that artificially textured bearings have improved performance at higher values of rotational speed (large values of Sommerfeld number).

In summary, decrease of eccentricity ratio of the order of 3%-6% can be achieved, followed by a corresponding decrease of friction coefficient in the range of 2%-3.6% in comparison to the plain journal bearing (bearing at low to moderate loads). The (T,5,1) and (T,5,5) bearing designs exhibit the best performance in terms of both performance indices, followed by designs (T,1,1) and (T,1,5).

**Table 14: Pareto front data and performance of optimal textured designs, for applied loads of 200 N, 500 N and 1000 N at rotational speed of 1000 RPM.**

| Case | Pareto fronts | Performance of optimal designs |
|---|---|---|
| T,1,1 | 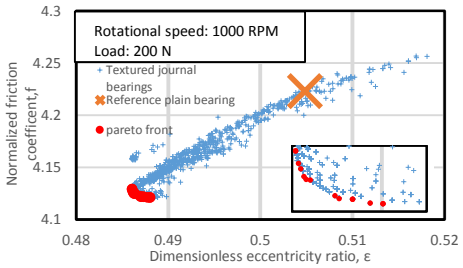 <br> 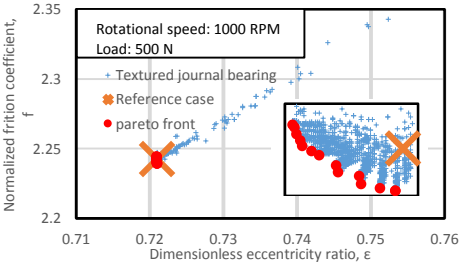 <br> 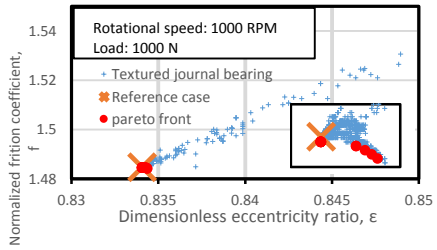 | 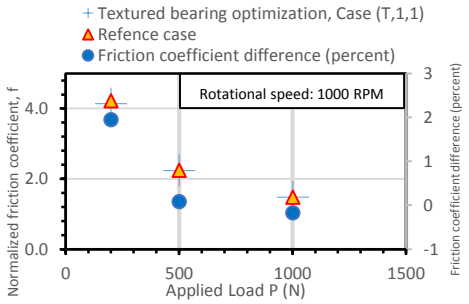 <br> 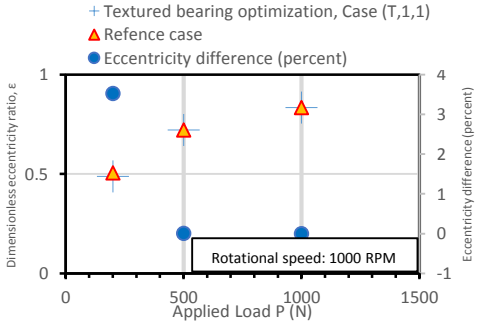 |
| T,1,5 | 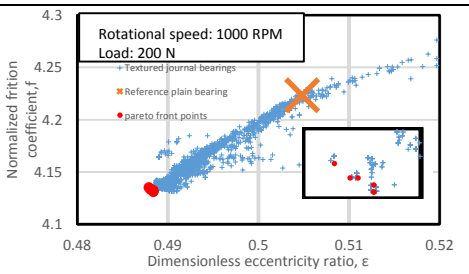 <br> 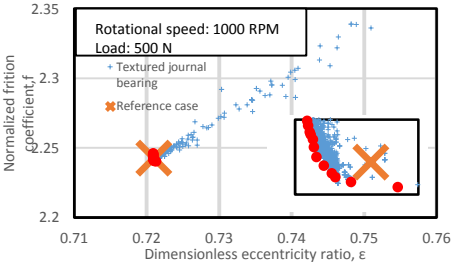 <br> 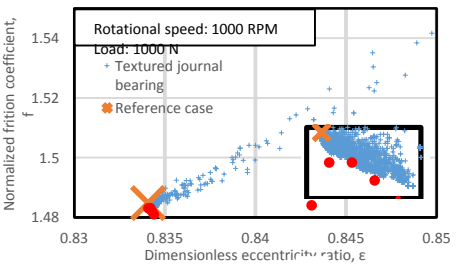 | 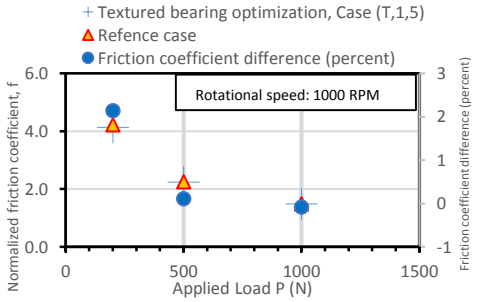 <br> 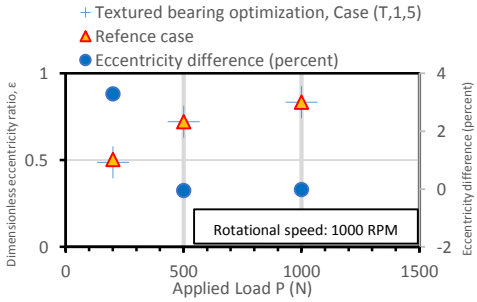 |

T,5,1

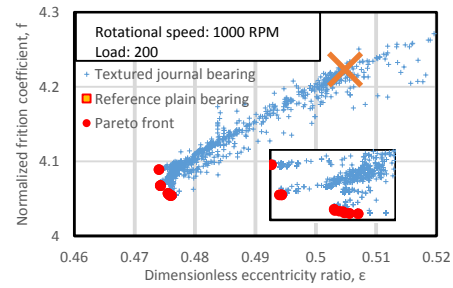
Rotational speed: 1000 RPM
Load: 200
Textured journal bearing
Reference plain bearing
Pareto front
Normalized frition coefficient, f
Dimensionless eccentricity ratio, ε

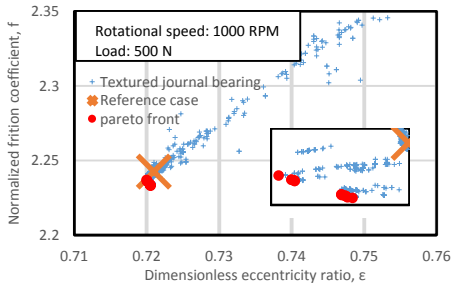
Rotational speed: 1000 RPM
Load: 500 N
Textured journal bearing
Reference case
pareto front
Normalized frition coefficient, f
Dimensionless eccentricity ratio, ε

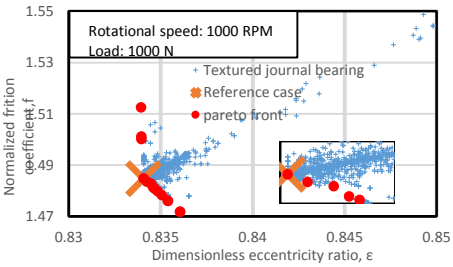
Rotational speed: 1000 RPM
Load: 1000 N
Textured journal bearing
Reference case
pareto front
Normalized frition coefficient, f
Dimensionless eccentricity ratio, ε

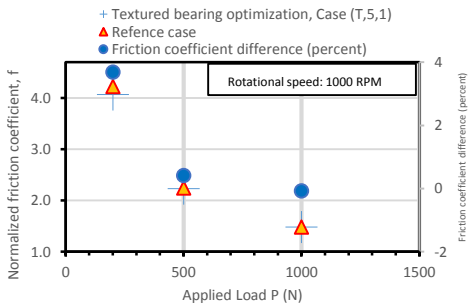
Textured bearing optimization, Case (T,5,1)
Refence case
Friction coefficient difference (percent)
Rotational speed: 1000 RPM
Normalized friction coefficient, f
Friction coefficient difference (percent)
Applied Load P (N)

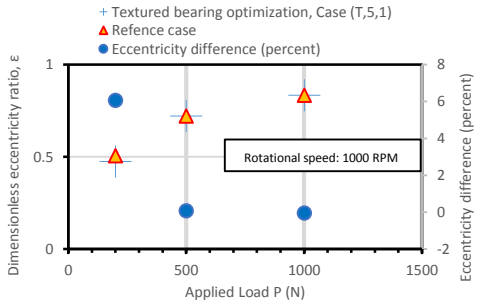
Textured bearing optimization, Case (T,5,1)
Refence case
Eccentricity difference (percent)
Rotational speed: 1000 RPM
Dimensionless eccentricity ratio, ε
Eccentricity difference (percent)
Applied Load P (N)

T,5,5

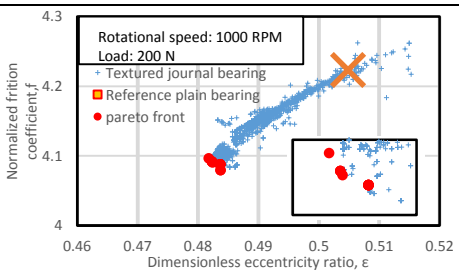
Rotational speed: 1000 RPM
Load: 200 N
Textured journal bearing
Reference plain bearing
pareto front
Normalized frition coefficient, f
Dimensionless eccentricity ratio, ε

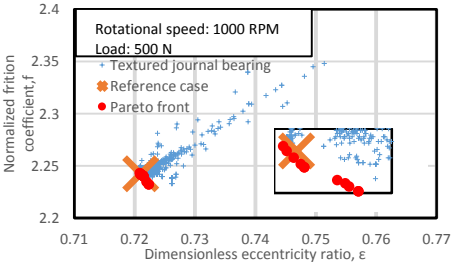
Rotational speed: 1000 RPM
Load: 500 N
Textured journal bearing
Reference case
Pareto front
Normalized frition coefficient, f
Dimensionless eccentricity ratio, ε

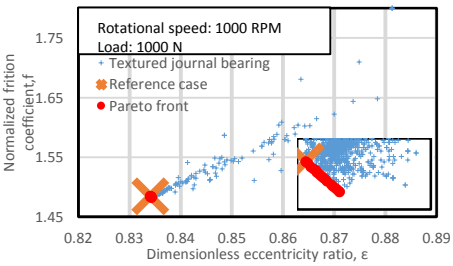
Rotational speed: 1000 RPM
Load: 1000 N
Textured journal bearing
Reference case
Pareto front
Normalized frition coefficient, f
Dimensionless eccentricity ratio, ε

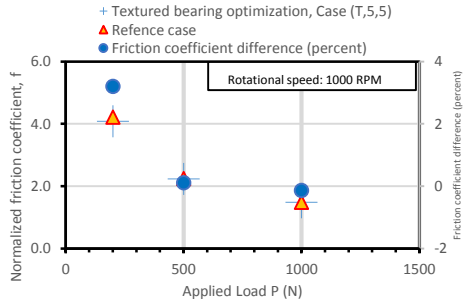
Textured bearing optimization, Case (T,5,5)
Refence case
Friction coefficient difference (percent)
Rotational speed: 1000 RPM
Normalized friction coefficient, f
Friction coefficient difference (percent)
Applied Load P (N)

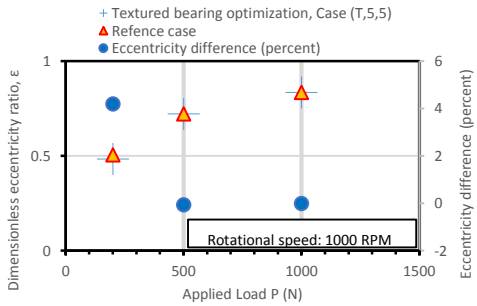
Textured bearing optimization, Case (T,5,5)
Refence case
Eccentricity difference (percent)
Rotational speed: 1000 RPM
Dimensionless eccentricity ratio, ε
Eccentricity difference (percent)
Applied Load P (N)

**Table 15: Pareto front data and performance of optimal textured designs, for applied loads of 200 N, 500 N and 1000 N at rotational speed of 500 RPM.**

| Case | Pareto fronts | Performance of optimal designs |
|---|---|---|
| T,1,1 | 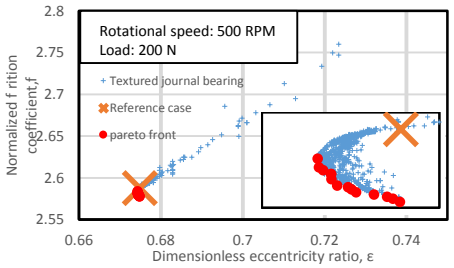 <br> 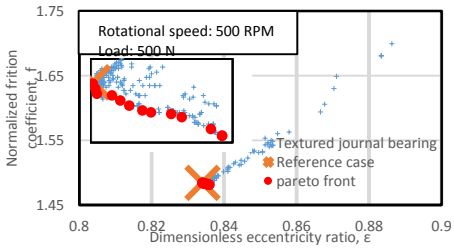 <br> 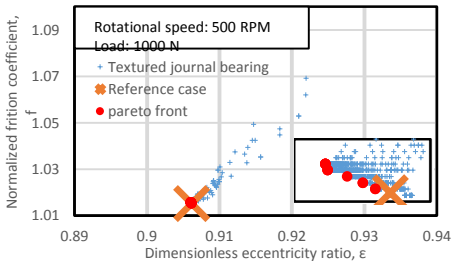 | 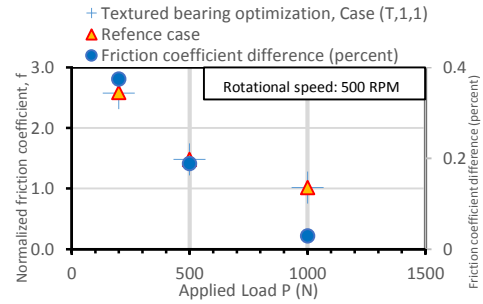 <br> 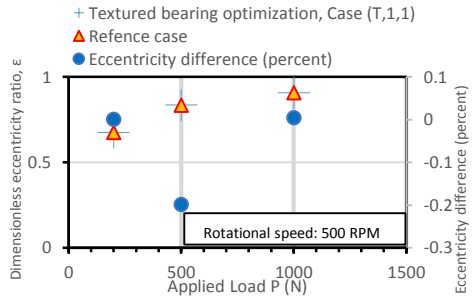 |
| T,1,5 | 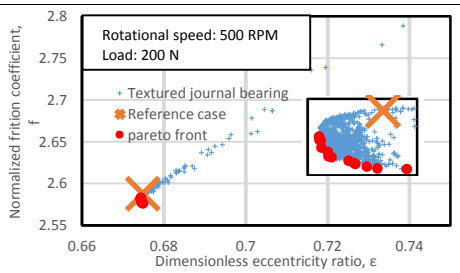 <br> 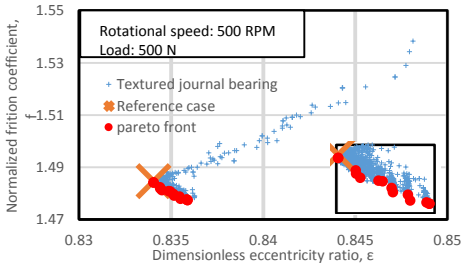 <br> 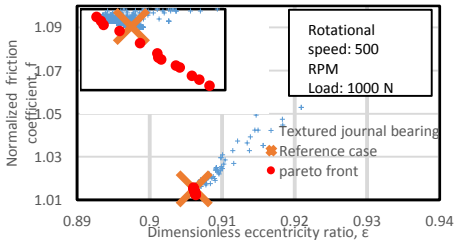 | 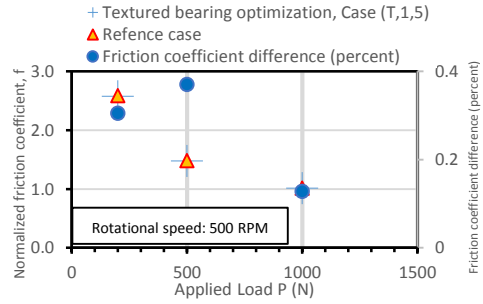 <br> 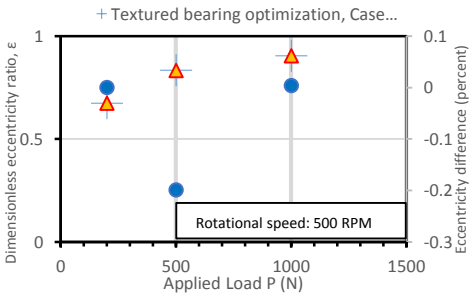 |

T,5,1

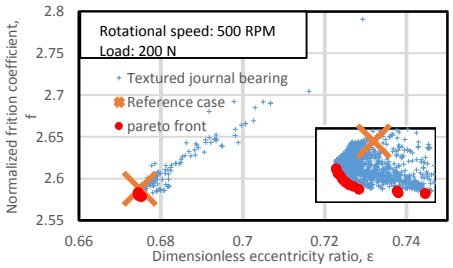
Rotational speed: 500 RPM
Load: 200 N
Textured journal bearing
Reference case
pareto front
Normalized friction coefficient, f
Dimensionless eccentricity ratio, ε

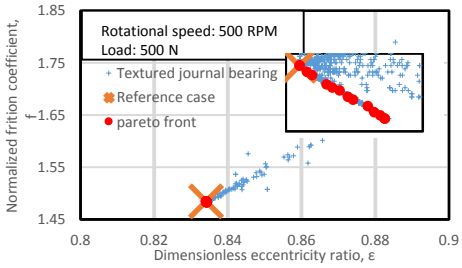
Rotational speed: 500 RPM
Load: 500 N
Textured journal bearing
Reference case
pareto front
Normalized friction coefficient, f
Dimensionless eccentricity ratio, ε

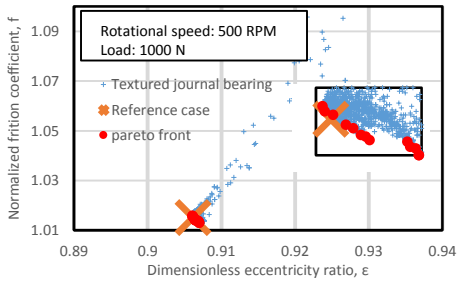
Rotational speed: 500 RPM
Load: 1000 N
Textured journal bearing
Reference case
pareto front
Normalized friction coefficient, f
Dimensionless eccentricity ratio, ε

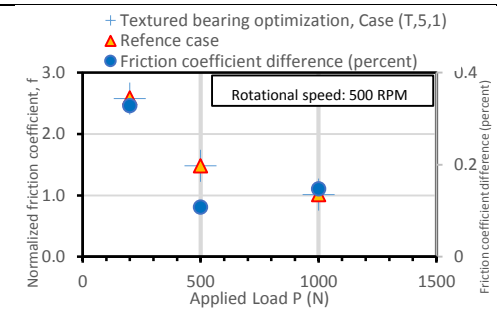
Textured bearing optimization, Case (T,5,1)
Refence case
Friction coefficient difference (percent)
Rotational speed: 500 RPM
Normalized friction coefficient, f
Friction coefficient difference (percent)
Applied Load P (N)

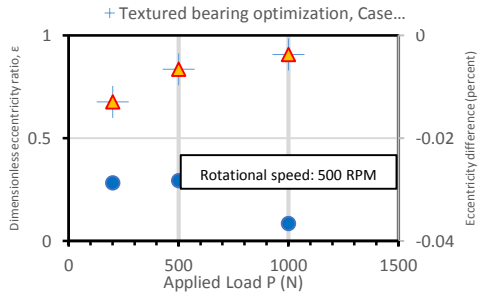
Textured bearing optimization, Case...
Rotational speed: 500 RPM
Dimensionless eccentricity ratio, ε
Eccentricity difference (percent)
Applied Load P (N)

T,5,5

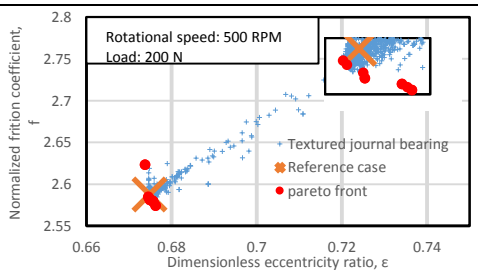
Rotational speed: 500 RPM
Load: 200 N
Textured journal bearing
Reference case
pareto front
Normalized friction coefficient, f
Dimensionless eccentricity ratio, ε

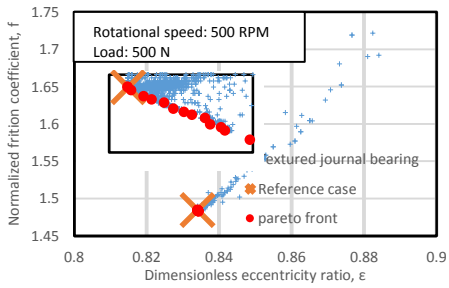
Rotational speed: 500 RPM
Load: 500 N
Reference case
pareto front
Normalized friction coefficient, f
Dimensionless eccentricity ratio, ε

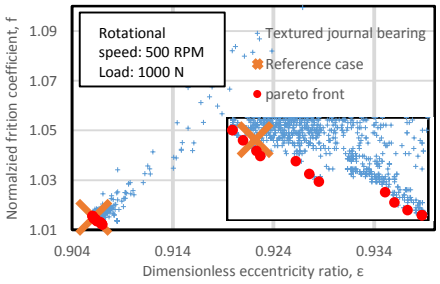
Rotational speed: 500 RPM
Load: 1000 N
Textured journal bearing
Reference case
pareto front
Normalized friction coefficient, f
Dimensionless eccentricity ratio, ε

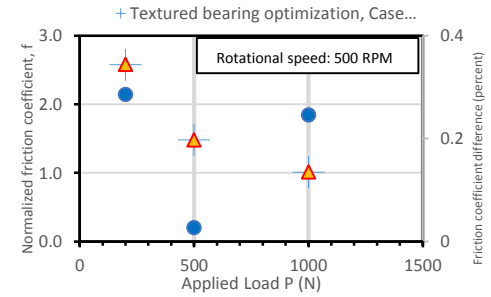
Textured bearing optimization, Case...
Rotational speed: 500 RPM
Normalized friction coefficient, f
Friction coefficient difference (percent)
Applied Load P (N)

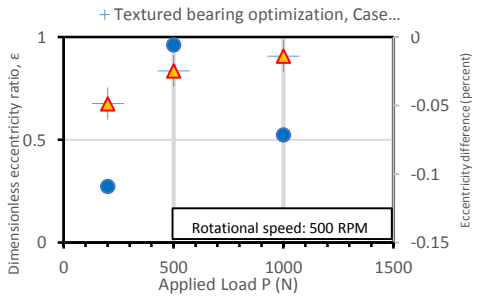
Textured bearing optimization, Case...
Rotational speed: 500 RPM
Dimensionless eccentricity ratio, ε
Eccentricity difference (percent)
Applied Load P (N)

### 3.5.2 Hydrophobic models

In Table 16 and Table 17, the simulation results regarding hydrophobic bearings are presented. Table 16 presents results corresponding to rotational speed of 1000 RPM, whereas in Table 17, results corresponding to rotational speed of 500 RPM are presented. Two different hydrophobic bearing designs are presented, corresponding to values of slip length equal to 0.1 and 1 respectively.

For each value of rotational speed, three different values of bearing load are simulated. At the first column of each Table, the name of the studied case is presented (naming conventions have been presented in Table 13). In the middle column of each Table, the Pareto fronts of each optimization problem are presented (large dots), along with non-dominant solutions of the optimization process (cross symbols), and the performance of the reference (plain) bearing (large X symbols). Hydrophobic bearings are shown to provide significant improvement, in comparison to plain bearings, for all the combinations of load and rotational speed. Best results are observed for values for non-dimensional slip length b* equal to 1.

In particular, for rotational speed equal to 1000 RPM, a decrease of dimensionless eccentricity ratio of approximately 20% is observed at the (low) load of 200 N, followed by a decrease of normalized friction coefficient by approximately 16%, in comparison to plain bearings. This improvement is less pronounced at higher values of bearing load. For rotational speed of 500 RPM, the trends are similar: an improvement of approximately 7% in dimensionless eccentricity ratio is observed at the (low) load of 200 N, followed by a decrease of normalized friction coefficient of approximately 12%. A substantial reduction of normalized friction coefficient is also observed at higher bearing loads (500 N, 1000 N).

**Table 16: Pareto front data and performance of optimal hydrophobic designs, for applied loads of 200 N, 500 N and 1000 N, at rotational speed of 1000 RPM.**

| Case | Pareto fronts | Performance of optimal designs |
|---|---|---|
| H,0.1 | 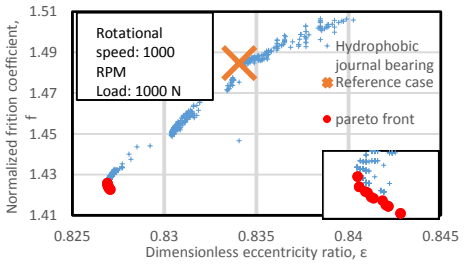 <br> 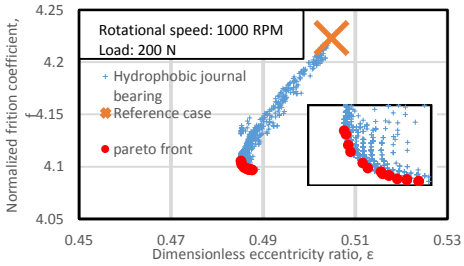 <br> 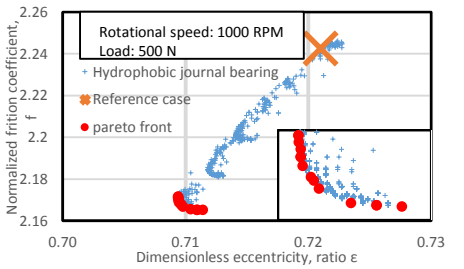 | 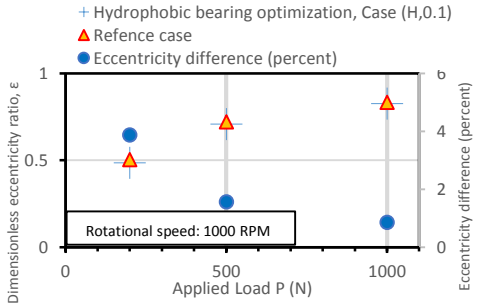 <br> 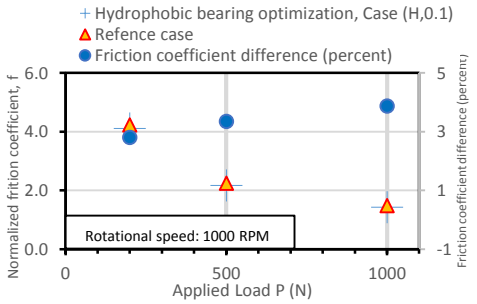 |
| H,1 | 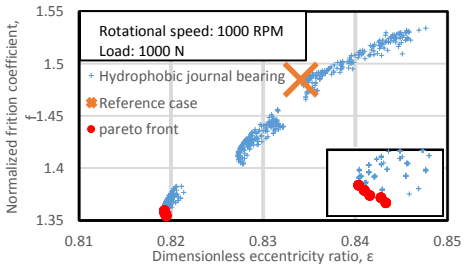 <br> 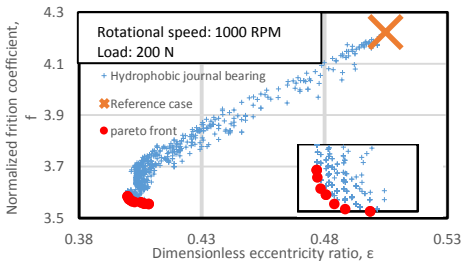 <br> 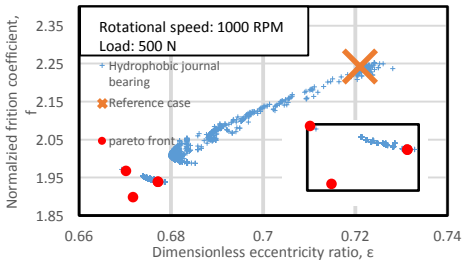 | 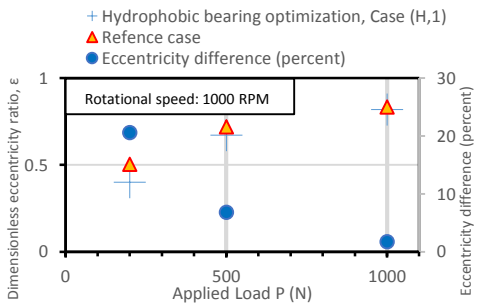 <br> 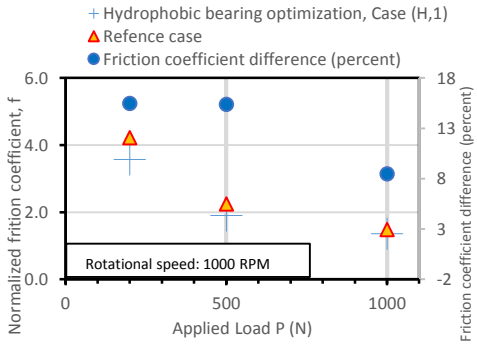 |

**Table 17: Pareto front data and performance of optimal hydrophobic designs, for applied loads of 200 N, 500 N and 1000 N, at rotational speed of 500 RPM.**

| Case | Pareto fronts | Performance of optimal designs |
|---|---|---|
| H, 0.1 | 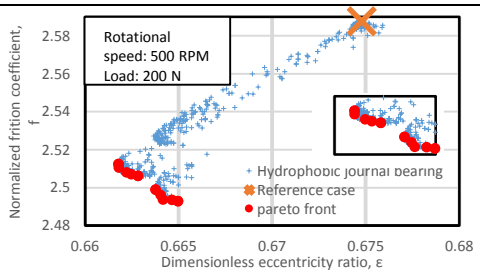 <br> 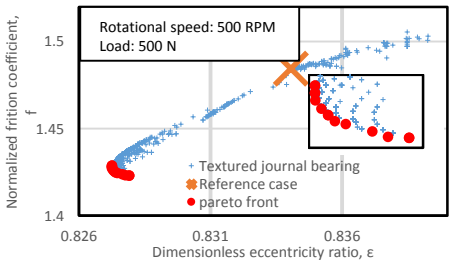 <br> 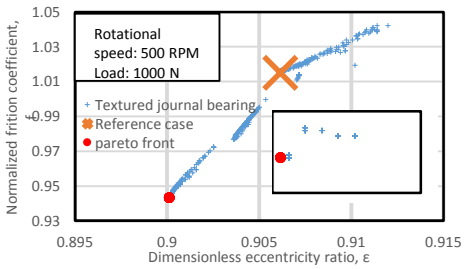 | 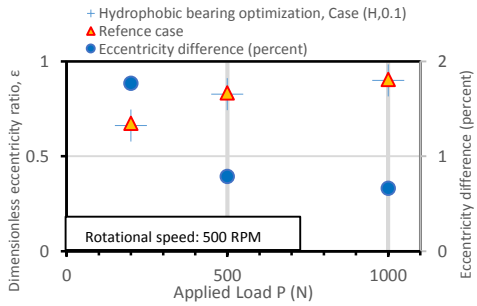 <br> 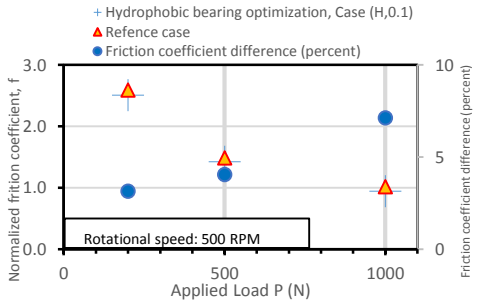 |
| H,1 | 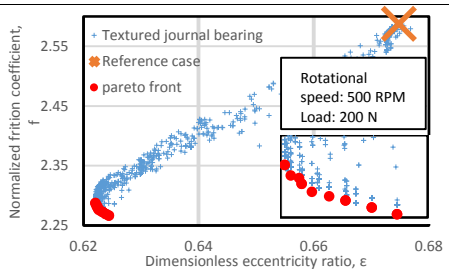 <br> 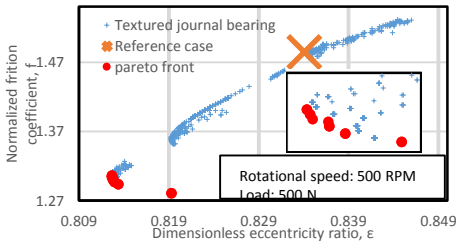 <br> 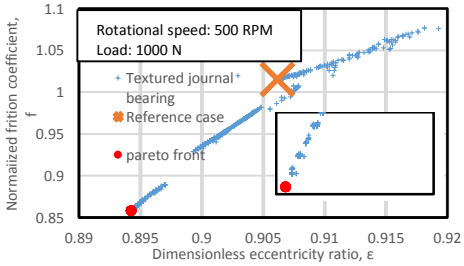 | 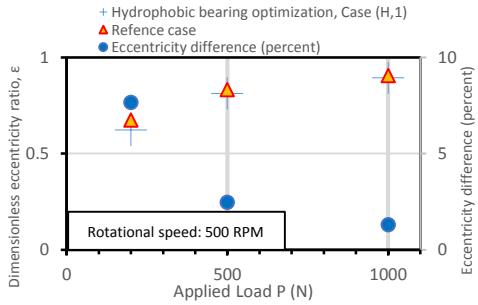 <br> 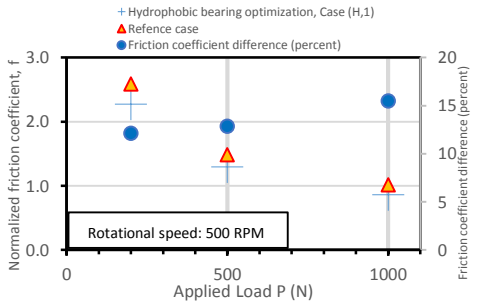 |

## 3.6 Optimum geometries of textured/hydrophobic bearings

Following the optimization of the textured and hydrophobic bearings of the previous section, the Pareto front points were used in order to find the optimum geometry for each case. At this point it should be noted that the optimum geometries presented below are the ones that showed satisfactory improvement of the bearing performance compared to the plain bearing for both artificial texturing and hydrophobicity. Also, for each combination of load and rotational speed, only a single point of the Pareto front was selected, which exhibits a very good performance in terms of both objectives (dimensionless eccentricity ratio, normalized friction coefficient).

### 3.6.1 Optimum geometries for textured surface models

The optimum geometries of textured bearings are presented in Table 18. Bearing performance indices (dimensionless eccentricity ratio, normalized friction coefficient) of the optimum geometries are shown in Table 19. It is shown that in textured bearings, improvement of performance in terms of dimensionless eccentricity ratio and normalized friction coefficient is noteworthy only for the combination of applied load of 200 N and rotational speed of 1000 RPM. Therefore, optimum geometries and relative results are shown only for this load/speed combination (Table 18).

**Table 18: Optimum geometry of textured bearings for the applied loads of 200 N and rotational speed of 1000 RPM.**

| Geometry parameters/ Textured cases | Applied Load (N) | Start x (deg) | End x (deg) | Density x | Start y (deg) | End y (deg) | Density y | Depth (μm) |
|---|---|---|---|---|---|---|---|---|
| T,1,1 | 200 | 47.37 | 188.55 | 0.79 | 0.09 | 0.91 | 0.76 | 19 |
| T,1,5 | 200 | 56.04 | 189.19 | 0.8 | 0.19 | 0.83 | 0.79 | 18 |
| T,5,1 | 200 | 55.69 | 196.45 | 0.78 | 0.13 | 0.89 | 0.74 | 23 |
| T,5,5 | 200 | 37.53 | 192.2 | 0.79 | 0.19 | 0.81 | 0.73 | 20 |

**Table 19: Textured bearings: load 200 N, rotational speed 1000 RPM: performance indices and corresponding improvement, in comparison to the reference plain bearing.**

| Geometry parameters/ Textured cases | Applied Load (N) | 1000 RPM | | | |
|---|---|---|---|---|---|
| | | Dimensionless eccentricity ratio | Improvement of the bearing performance (%) | Normalized friction coefficient | Improvement of the bearing performance (%) |
| T,1,1 | 200 | 0.4870 | 3.52 | 4.141 | 1.95 |
| T,1,5 | 200 | 0.4882 | 3.29 | 4.133 | 2.14 |
| T,5,1 | 200 | 0.4742 | 6.059 | 4.067 | 3.68 |
| T,5,5 | 200 | 0.4836 | 4.19 | 4.088 | 3.21 |

### 3.6.2 Optimum geometries for hydrophobic surface models

The optimum hydrophobic bearing designs are presented in Table 20 and Table 21. Bearing performance indices (dimensionless eccentricity ratio, normalized friction coefficient) of the optimum geometries are shown in Table 22 and Table 23. It is shown that in hydrophobic bearings, performance of the bearing showed noteworthy improvement for all the studied combinations of applied load (200 N, 500 N and 1000 N) and rotational speed (500 RPM and 1000 RPM).

**Table 20: Optimum geometry of hydrophobic bearings for applied loads of 200 N, 500 N and 1000 N, and rotational speed of 1000 RPM.**

| Geometry parameters/ Hydrophobic cases | Applied Load (N) | Slip start angle (deg) | Slip end angle (deg) | Slip start y | Slip end y |
|---|---|---|---|---|---|
| H,0.1 | 1000 | 85.25 | 197.49 | 0.14 | 0.85 |
| | 500 | 43.38 | 198.94 | 0.15 | 0.84 |
| | 200 | 35.59 | 195.53 | 0.18 | 0.82 |
| H,1 | 1000 | 29.84 | 195.37 | 0.12 | 0.88 |
| | 500 | 43.38 | 198.94 | 0.15 | 0.84 |
| | 200 | 24.88 | 195.97 | 0.14 | 0.87 |

**Table 21: Optimum geometry of hydrophobic bearings for applied loads of 200 N, 500 N and 1000 N, and rotational speed of 500 RPM.**

| Geometry parameters/ Hydrophobic cases | Applied Load (N) | Slip start angle (deg) | Slip end angle (deg) | Slip start y | Slip end y |
|---|---|---|---|---|---|
| H,0.1 | 1000 | 82.46 | 196.27 | 0.12 | 0.89 |
| | 500 | 57.58 | 198.99 | 0.13 | 0.88 |
| | 200 | 81.98 | 199 | 0.13 | 0.85 |
| H,1 | 1000 | 49.75 | 196.42 | 0.12 | 0.87 |
| | 500 | 57.58 | 198.99 | 0.13 | 0.88 |
| | 200 | 22.47 | 197.98 | 0.15 | 0.86 |

**Table 22: Hydrophobic bearings: load 200 N, 500 N and 1000 N, rotational speed 500 RPM and 1000 RPM: values of dimensionless eccentricity ratio and corresponding improvement, in comparison to the reference plain bearing.**

| Geometry parameters/ Textured cases | Applied Load (N) | 1000 RPM | | 500 RPM | |
|---|---|---|---|---|---|
| | | Dimensionless eccentricity ratio | Improvement of the bearing performance (%) | Dimensionless eccentricity ratio | Improvement of the bearing performance (%) |
| H,0.1 | 1000 | 0.8269 | 0.85 | 0.9001 | 0.66 |
| | 500 | 0.7097 | 1.56 | 0.8274 | 0.79 |
| | 200 | 0.4852 | 3.88 | 0.6628 | 1.77 |
| H,1 | 1000 | 0.8193 | 1.76 | 0.8942 | 1.31 |
| | 500 | 0.6717 | 6.83 | 0.8133 | 2.48 |
| | 200 | 0.4008 | 20.59 | 0.6229 | 7.67 |

**Table 23: Hydrophobic bearings: load 200 N, 500 N and 1000 N, rotational speed 500 RPM and 1000 RPM: values of normalized friction coefficient and corresponding improvement, in comparison to the reference plain bearing.**

| Geometry parameters/ Textured cases | Applied Load (N) | 1000 RPM | | 500 RPM | |
|---|---|---|---|---|---|
| | | Normalized friction coefficient | Improvement of the bearing performance (%) | Normalized friction coefficient | Improvement of the bearing performance (%) |
| H,0.1 | 1000 | 1.4243 | 3.87 | 0.9433 | 7.12 |
| | 500 | 2.1675 | 3.35 | 1.4246 | 4.04 |
| | 200 | 4.1048 | 2.81 | 2.5061 | 3.15 |
| H,1 | 1000 | 1.3563 | 8.46 | 0.8582 | 15.50 |
| | 500 | 1.8978 | 15.38 | 1.2938 | 12.85 |
| | 200 | 3.5700 | 15.47 | 2.2741 | 12.12 |

## 3.7 Textured/ hydrophobic bearings versus the reference plain bearing

In section 3.6 it has been shown that introduction of artificial surface texturing or hydrophobicity at part of the bearing surface may lead to substantial improvement of bearing performance. In Figure 29-Figure 31, oil film thickness and pressure distributions in the lubricant domain are presented, for bearing load of 200 N and rotational speed of 1000 RPM. Pressure distribution in the textured and hydrophobic bearings exhibits an increased gradient in the converging region, reaching a maximum which is higher than the corresponding of the plain bearing. This performance is due to the existence of dimples/ hydrophobic surface in the converging region of the bearing, which at the same time, leads to a reduction of corresponding shear stresses in the lubricant/ rotor interface.

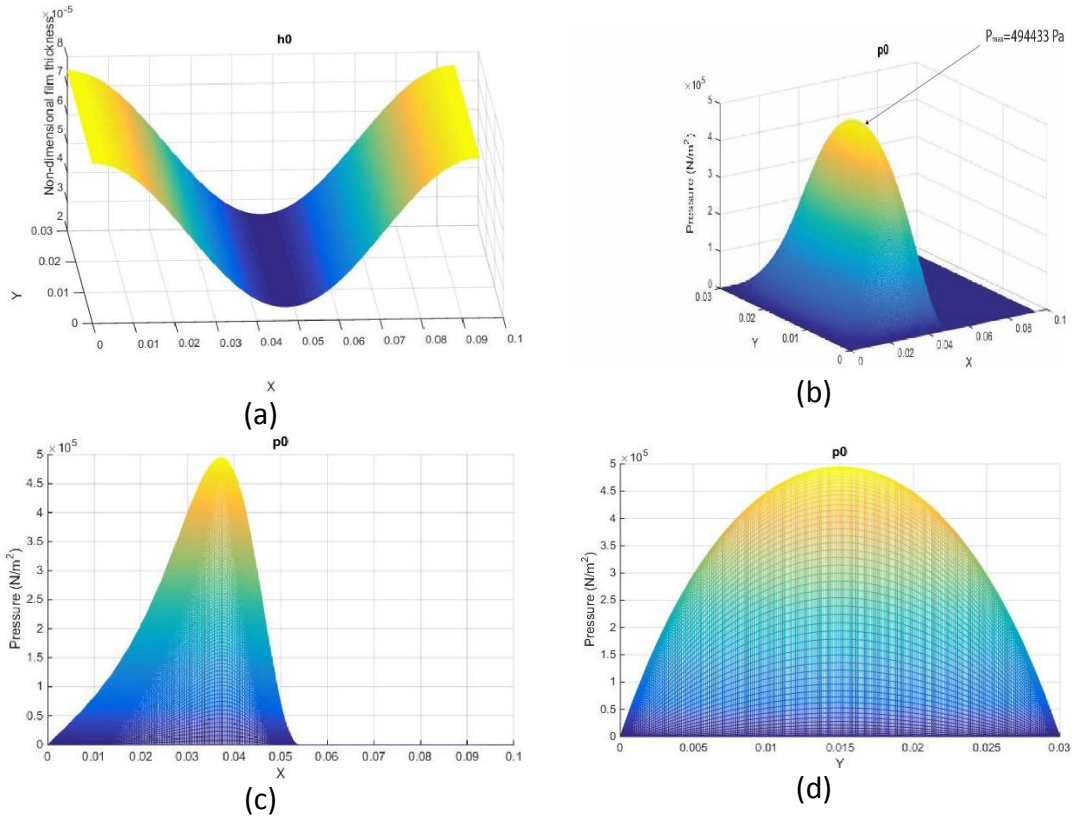


**Figure 29: Reference plain bearing: (a) 3d profile of lubricant film thickness, (b) 3d profile of developed pressure in the lubricant film, (c) pressure profile along the x axis (circumferentially), (d) pressure profile along the y axis (axially).**

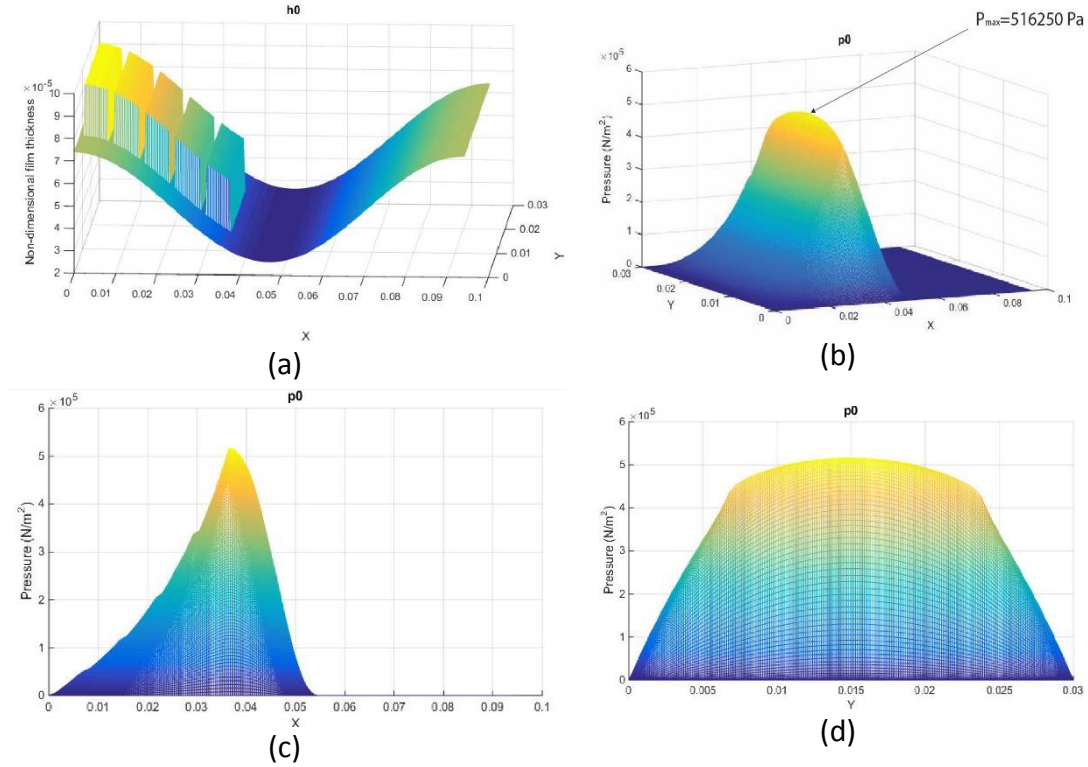


**Figure 30: Textured bearing design (5x1): (a) 3d profile of lubricant film thickness, (b) 3d profile of developed pressure in the lubricant film, (c) pressure profile along the x axis (circumferentially), (d) pressure profile along the y axis (axially)**

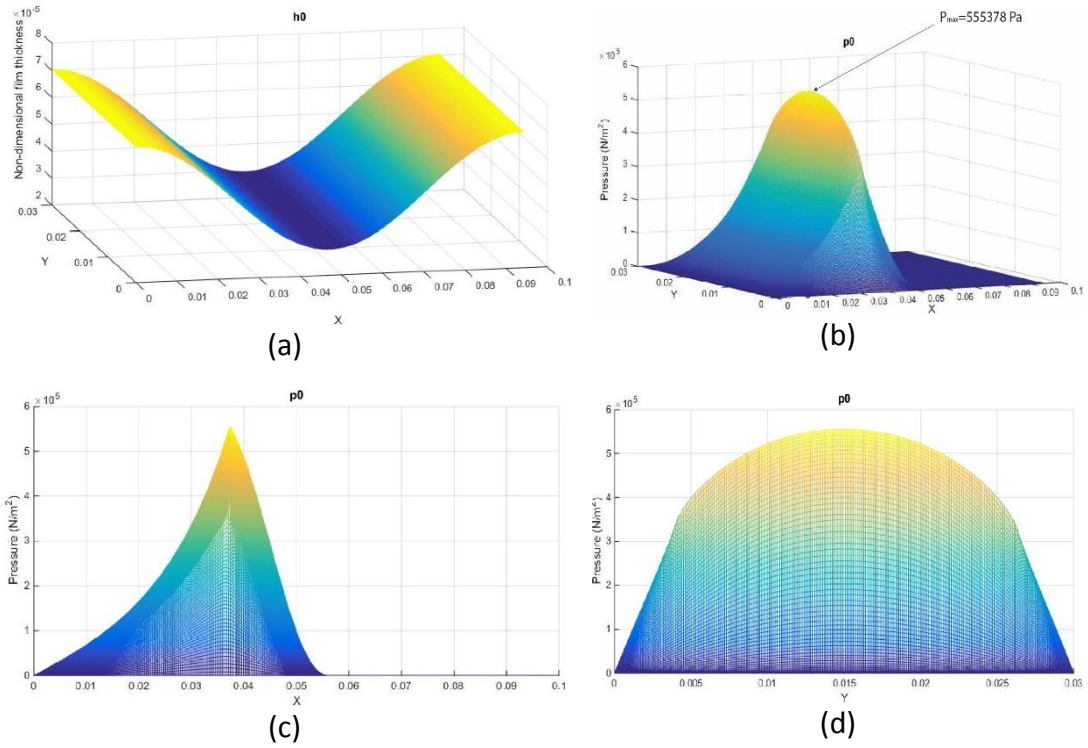


**Figure 31: Hydrophobic bearing design (H,1.0) : (a) 3d profile of lubricant film thickness, (b) 3d profile of developed pressure in the lubricant film, (c) pressure profile along the x axis (circumferentially), (d) pressure profile along the y axis (axially).**

# 4 Design and construction of a journal bearing test-rig

## 4.1 Existing UMT Tribometer facility

### 4.1.1 UMT Tribometer

The UMT Multi-Specimen Test System can be used effectively for the tribological testing of ferrous and non-ferrous metals, plastics, ceramics, paper, composites, thin and thick coatings, as well as of solid lubricants, lubricating fluids, oils and greases.

Various common tribology test models are available such as:

- Pin on disk
- Ball on disk
- Ball on one, two or three balls
- Pin on V-block
- Block on ring
- Disc on disc (flat on flat)
- Screw in nut

The UMT can accommodate both upper and lower samples of practically any shape. The upper specimen is connected to a vertical linear motion system that has a travel length of 150 mm. Wear measurements can be performed by the instrument to an accuracy of 50 nm. A precision spindle can rotate the lower specimen at speeds from 0.001 RPM up to 5,000 RPM. Accurate strain-gauge sensors perform simultaneous measurements of load and torque in two to six axes. The forces can be measured precisely in the ranges from milligrams to kilograms, with a resolution of 0.00003% of the full-scale and very high repeatability.

A normal-load sensor provides feedback to the vertical motion controller, actively adjusting the sample position to ensure a constant load during testing. The tester has fully automated PC-based motor-control and data acquisition, with a user-friendly proprietary software system in a Windows 7 multitasking environment. The test data can be acquired, calculated and displayed in real time, as well as stored for future retrieval.

**Figure 32: UMT Tribometer.**

### 4.1.2 Oil pump

The pump feeding oil to the journal bearing of the experimental setup is the RK-4 Rotor Kit Oil Pump of Bently Nevada. The pump comes with an analog type indicator that shows pressure in psi and in kPa. The maximum pressure of the pump is 4.2 kPa.


**Figure 33: RK-4 Rotor Kit Oil Pump.**

For the lubrication of the bearing the lubricant oil that was used is the SAE 10, and its dynamic viscosity is shown in Table 24, as they have been evaluated in laboratory conditions.

**Table 24: Dynamic viscosity of SAE 10 oil**

| Temperature | Dynamic viscosity (mPa ·s) |
|---|---|
| 30 °C | 54.620 |
| 40 °C | 33.627 |
| 80 °C | 8.308 |

### 4.1.3 Electric motor

The journal bearing shaft receives motion from an electric motor, which can develop a rotational speed up to 10000 RPM. The rotor model is the Bently Nevada Rotor Kit Model RK4. The rotational speed and the acceleration/deceleration of the electric motor, and therefore of the shaft, can be regulated from a controller, the RK4 Controller. The rotational speed of the shaft is measured by two proximity sensors that are installed in a suitably shaped gear.

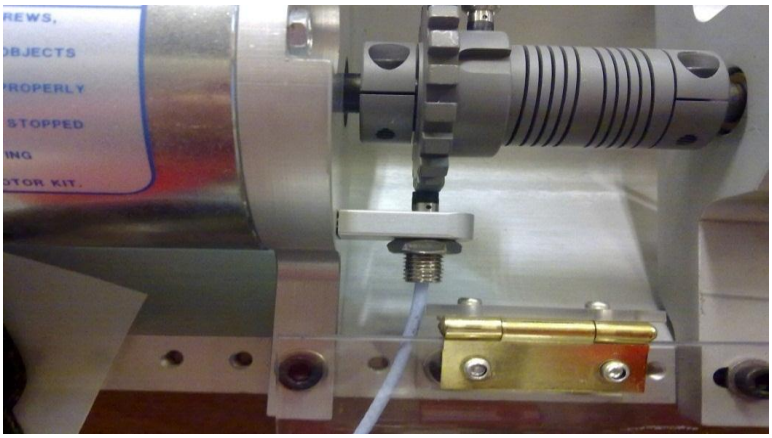

**Figure 34: Electric motor of the bearing test rig.**

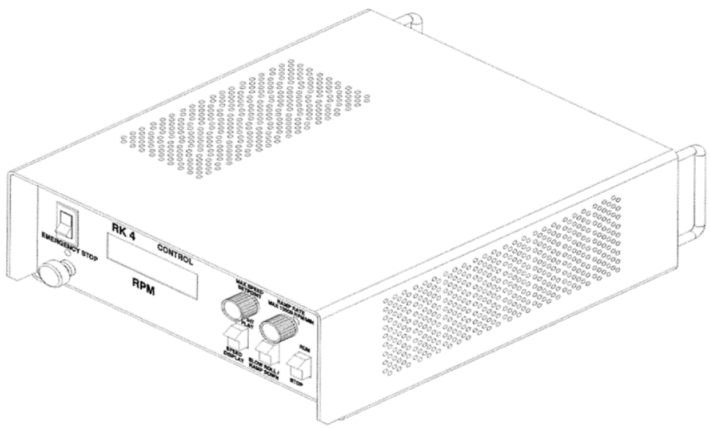


**Figure 35: Drawn representation of the RK4 Controller.**

The shaft is attached to the electric motor with the use of flexible torsional coupling. This way, the misalignment of the shaft in the bearing can be avoided. Pretension of the shaft can be imposed by tightening of four screws that form a cross.

## 4.2 Design of journal bearing testing apparatus

### 4.2.1 General description

Before the actual construction of the experimental setup, a CAD assembly design was made in Autodesk Inventor 2016, in order to aid the manufacturing process and to depict all the individual parts and their details. The final assembly consists of 23 parts, which are the following and can also be seen in the final drawings coming as an appendix of the present thesis.

1. Rail for z motion upper part
2. Rail for z motion lower part
3. L part
4. TCH100 Torque sensor
5. Bearing housing flange
6. Bearing housing
7. Bearing
8. Support for ball bearing P000 upper part
9. Support for ball bearing P000 lower part
10. Oil reservoir
11. Basic motor support structure
12. Tribometer flange
13. Ball bearing P000
14. Shaft
15. Rolling element bearing (SN507)
16. Motor (Bently Nevada RK4)
17. Motor support shell
18. Motor support shell(s)
19. Support structure leg(s)
20. Support for slider
21. Slider
22. Slider guide(s) part1
23. Slider guide(s) part2

The above assigned numbers and the respective test rig items are seen in Figure 36.

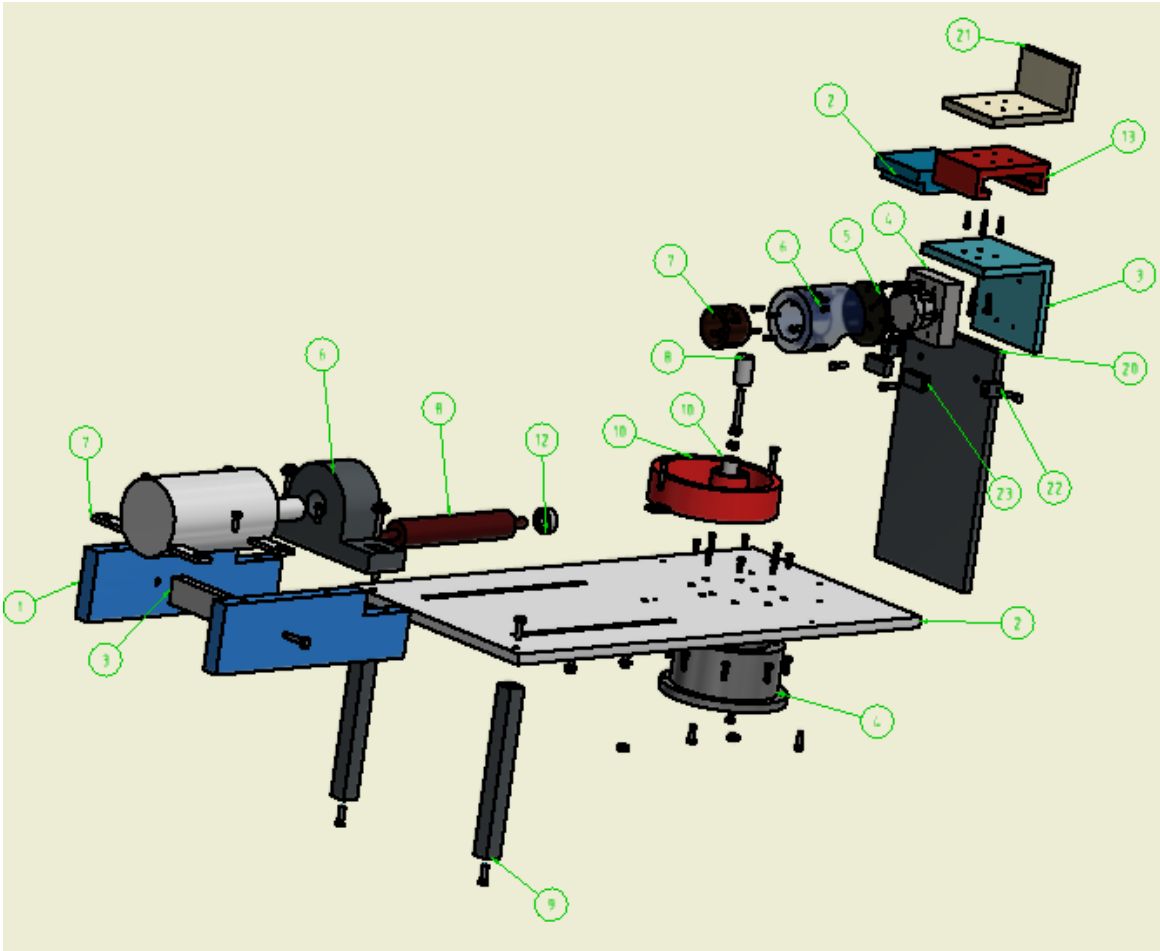

**Figure 36: Exploded view of the journal bearing test rig.**

The test rig can be divided in four parts based on the functionality issues:

The first part is the *bearing-rail system*, and it consists of the upper and lower rail for z axis motion (items 1 and 2), the L part (item 3), the torque sensor type TH-100 (part 4), the bearing housing and bearing housing flange (parts 6 and 5, respectively) and finally the journal bearing (part 7). The connection of the itemσ in the bearing-rail system goes as follows: the upper part of the rail for z motion connects to the tribometer load sensor so it remains steady throughout the experiment and the load can be applied to the journal bearing through the tribometer. The load sensor is responsible for measuring and adjusting the applied load at any time. Then, the lower part of the rail for the z motion is inserted in the upper, in order for the rail system to be completed. Then the L part is attached to the lower part of the rail and, on it, the torque sensor is placed, so it can take measurements of the friction torque of the journal bearing during the experiments. The bearing housing flange is connected to the torque sensor and supports the bearing housing. The bearing is placed inside the bearing housing. So, with this connection between parts 1 to 7 the bearing system remains steady and measurements can be taken with the use of the tribometer, with a range of applied loads from 1 to 1000 N. Also, the use of the tribometer enables the temporal variation of the applied load during the experiments, allowing

measurements to be taken in transient loading states, apart from the steady state condition.

The second part is the *motor-shaft system*. It is composed of the shaft (item 14), the motor (item 16), the rolling bearing SN507 and ball bearing P000 (items 15 and 13 respectively) and the motor support shells (items 17 and 18). The shaft is attached to the motor through a flexible torsional coupling as it has been described in 4.1.3. The rolling element bearing SN507 and the ball bearing P000 are placed on the two ends of the shaft, as shown in Figure 36. This way the shaft is supported at either ends, minimizing the effects of bending moment. The motor is placed on its support shells. The support shells are designed and constructed in a way that the back and forth movement of the motor-shaft system is enabled. This way, the shaft can be inserted or taken out of the bearing, whenever necessary, with minimum effort.

The third part is the *support system* for the test rig. It is consisted of the basic support structure (item 11), the tribometer flange (item 12), the oil reservoir (item 10) the upper and lower support parts for ball bearing P000 (items 8 and 9 respectively) and support structure legs (item 19). The tribometer flange is placed on the tribometer, and the basic support structure is connected on its top. This way, the whole test rig is steady and protected from oscillation, which may be developed by the high rotational speeds of the motor. The basic support structure has two slots that, combined with the support shells of the motor, enable the back and forth movement of the motor and the shaft. The support for the ball bearing P000 is consisted of two parts, which are connected with a screw. This way, the height of the P000 ball bearing can be regulated with an accuracy of micrometers on the vertical axis so that the upper part of the support can be placed in the right height. Then it is made steady in that position with the use of two nuts.

The fourth part is the *autonomous slider system.* It consists of the slider support slider (item 20), the slider (item 21) and the slider guide (items 22 and 23). These four items, when connected, they form an autonomous slider system that makes feasible the load application through constant weights, without requiring the use of the UMT tribometer load system. The constant weights are placed on the slider, and with the use of the slider guides, the constant load is applied to the bearing and the shaft. When using this system the applied load can exceed 1000 N, which is the applied load upper limit when using the UMT tribometer load sensor. All the measurements in this case are done with the use of the torque sensor TH-100. This system can be used for both steady-state and transient experiments, however the latter requires the use of the UMT Tribometer.

At this point it should be noted that the autonomous slider system is optional. When the load is applied through the UMT tribometer, only the three first subsystems are needed. When the UMT tribometer setup is used, the load is applied to the bearing through the load sensor, which is responsible for measurements in steady and in transient states. The developed friction force in the bearing can be measured with the use of the torque sensor, which is placed between the L part and the bearing, as it has already been described.

A photo of the assembled journal bearing test rig is shown in Figure 37:

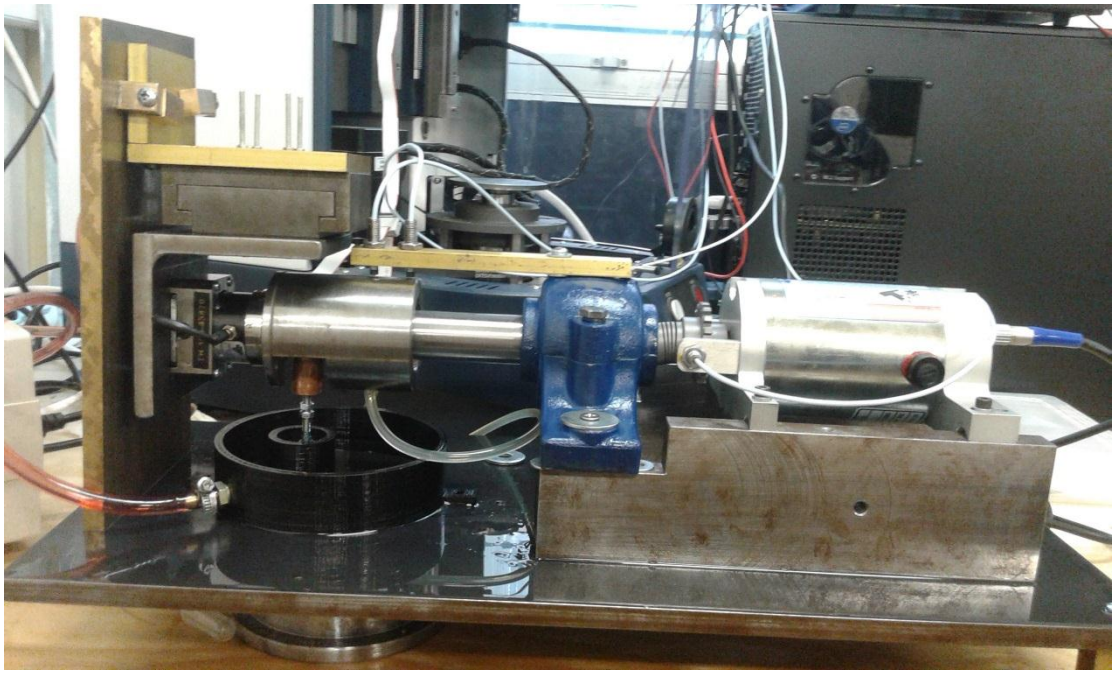

**Figure 37: Assembled journal bearing test rig.**

All the used screws for the connection of the items are metric, ranging from M3 to M6.

The bearing is lubricated with the use of the Bently pump, that has been described in section 4.1.2. The oil that leaks out of the bearing is gathered in the oil reservoir, and sent back to the bearing, with the help of a piping system that is connected to the pump on one end and to the bearing through the oil feed hole on the other end. The lubricating system consists of a number of pipes, angles, connectors and switches.

### 4.2.2 Materials

The items were constructed from the following materials:

**Table 25: Journal bearing test rig: part materials.**

| Item | Item number | Material |
|---|---|---|
| Rail for z motion upper part | 1 | Iron |
| Rail for z motion lower part | 2 | Iron |
| L part | 3 | Iron |
| Bearing housing flange | 5 | Steel |
| Bearing housing | 6 | Steel |
| Bearing | 7 | Copper/ Phosphorus |
| Support for ball bearing P000 upper part | 8 | Copper |
| Support for ball bearing P000 lower part | 9 | Copper |
| Oil reservoir | 10 | ABS plastic |
| Basic motor support structure | 11 | Iron |
| Tribometer flange | 12 | Steel |
| Shaft | 14 | Stainless steel |
| Motor support shell | 17 | Steel |
| Motor support shell(s) | 18 | Steel |
| Support structure leg(s) | 19 | Steel |
| Slider support | 20 | Brass |
| Slider | 21 | Brass |
| Slider guide(s)-part 1 | 22 | Brass |
| Slider guide(s)-part 2 | 23 | Brass |

### 4.2.3 Bearing

The bearing has a diameter of 30 mm, a length of 31 mm and a thickness of 7 mm. The two ends of the bearing have each a fillet of 0.5 mm, in order for the lubricant to exit smoothly during the testing operation. So the bearing active length is 30 mm.

- Oil feed slot: it is placed at an axial position of 15.5 mm from the bearing′s edge.
- Proximity probes: the proximity probes slots are placed at a relative angle of $45^{o}$ to the oil feed slot and at a height of 10.5 mm and 20.5 mm from the bearing edge. So, in total there are 4 proximity probes slots.
- Pressure probes: the pressure probes are placed at a circumferential position of 125, 180 and 235 degrees relative to the oil feed slot and at an axial position of 8 mm and 15.5 mm from the bearing′s edge. In total there are 6 pressure probes, which gives an evaluation of the overall pressure profile that is developed in the lubricating film.

- Temperature probes: there are in total 6 temperature probes. Four of them are placed at a circumferential position of 157.5 and 202.5 degrees relative to the oil feed slot, and at an axial position of 8 mm and 15.5 mm from the bearing edge. One temperature probe is placed at a circumferential position of 144.5 degrees relative to the oil feed slot, and at an axial position of 13 mm from the bearing edge. Finally, one additional temperature probe that is placed at a circumferential position of 144.5 degrees relative to the oil feed slot, and at an axial position of 19 mm from the bearing edge. The temperature probe depths vary from 2 mm to 6.4 mm. That variation in the positions and the depth gives an evaluation of the overall temperature profile that is developed in the bearing through its thickness.

The exact positions of the slot of the oil feed, the proximity, the pressure and the temperature probes are shown in Figure 38. The bearings that were manufactured came only with the oil hole on them as shown in Figure 39.

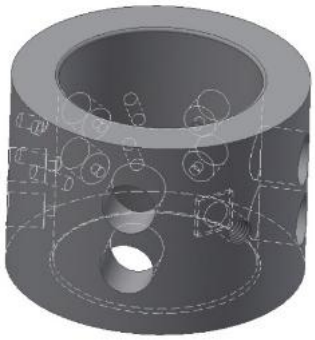

**Figure 38: 3D view of a bearing specimen.**

**Figure 39: Manufactured bearings. Copper bearing (left), and steel bearing (right).**

### 4.2.4 Bearing housing

The bearing housing has a diameter of 44 mm, a length of 78 mm and a thickness of 12 mm. Its diameter is set at 44 mm in order to enable the bearing to fit exactly inside the bearing housing, as the bearing has an outer diameter of 44mm. At an axial position of 33 mm from the bearing housing top edge, a reduced inner diameter of 38 mm is present, which acts as a stop for the bearing, in order not to move any further from that point, during testing operation. The bearing housing has the same number of slots as the bearing and its main use is to support the bearing as well as the different probes that are used in the experiments. So, the slots are located in the follow positions:

- Oil feed slot: it is placed at an axial position of 25.5 mm from the bearing bottom edge.
- Proximity probes: the proximity probes slots are placed at a relative angle of 45 to the oil feed slot and at a height of 20.5 mm and 30.5 mm from the bearing bottom edge.
- Pressure probes: the pressure probes are placed at a circumferential position is 125, 180 and 235 degrees relative to the oil feed slot, and at an axial position of 18 mm and 25.5 mm from the bearing edge.
- Temperature probes: there are in total 6 temperature probes. Four of them are placed at a circumferential position of 157.5 and 202.5 degrees relative to the oil feed slot, and at an axial position of 18 mm and 25.5 mm from the bearing´s edge. One temperature probe is placed at a circumferential position of 144.5 degrees relative to the oil feed slot, and at an axial position of 23 mm from the bearing edge. Finally, one additional temperature probe that is placed at a circumferential position of 144.5 degrees relative to the oil feed slot, and at an axial position of 29 mm from the bearing edge. The slots for the temperature probes are threaded, in order for the temperature probe to be suitably adjusted.

At the top edge of the bearing housing there are 5 threaded holes, which are used for connection between the bearing housing and the bearing housing flange.

The exact positions of the slot of the oil feed, the proximity, the pressure and the temperature probes are shown in Figure 40. The bearing housing that was manufactured came only with the oil hole on it as shown in Figure 40.

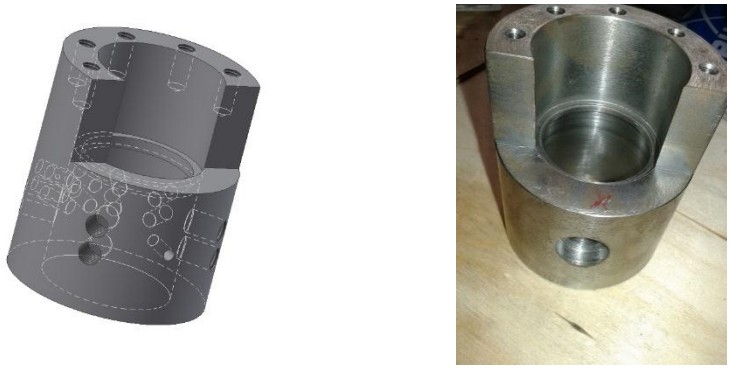

**Figure 40: Bearing housing: 3D view of the bearing housing (left), photo of the manufactured part (right).**

### 4.2.5 Shaft

The shaft consists of three segments. The main segment has a length of 160 mm and a diameter of 29.9 mm. This diameter fits within the bearing inner diameter of 30 mm, and provides a diametral clearance of 0.1 mm. The second segment has a length of 30 mm and a diameter of 10 and is used to connect the shaft with the motor. The third segment has a length of 25 mm and a diameter of 10 mm. On this segment the rolling element bearing P000 is connected. The active length of the shaft has a length of 30 mm, which is the same as the bearing active length.

A CAD representation of the shaft is shown in Figure 41.

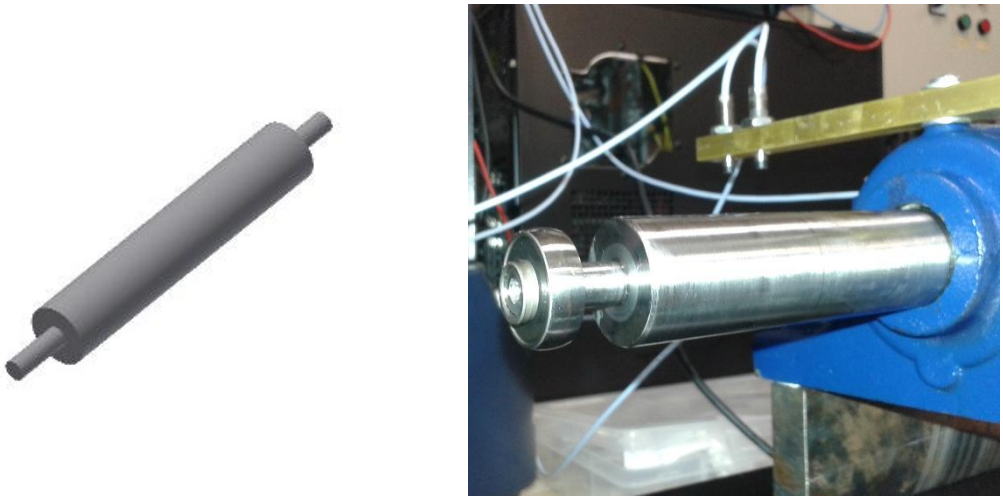

**Figure 41: 3D view of the test-rig shaft (left), manufactured shaft (right).**

## 4.3 Auxiliary systems, measurement sensors

For the purposes of the measurements, a variety of sensors and probes has been used. Below there is an analytical presentation of them.

### 4.3.1 Rotational motion drive with specimen table type S21ME/S21M0

This drive has the following characteristics:

- Maximum rotational speed: 1000 RPM
- Maximum Load: 20 kg

- Acceleration/Deceleration time (s): 5
- Encoder resolution: 8000

**Figure 42: Rotational motor drive type S21ME/S21M0.**

### 4.3.2 Load sensor type DHF-100

- Range: 10 to 1000 N (1 to 100 kg)
- Resolution: 50 mN (5.0 g)

**Figure 43: Load sensor type DHF-100.**

### 4.3.3 Torque sensor type TH-100

*Torque*:

- Range: 100 to 20000 N*mm
- Resolution: 2.5 N*mm

*Load*:

- Range: 10 to 1160 N (1 to 116 kg)
- Resolution: 135 mN

*Friction/Vertical Force*:

- Range 5.8 έως 580 N (0.58 έως 58 kg)
- Resolution: 65 mN

**Figure 44: Torque sensor type TH-100.**

### 4.3.4 Proximity sensor

The proximity sensors that are used came with the Bently Nevada Rotor Kit Model RK4 test rig. They are able to measure the distance between a metallic object and their tip. The measurements, which are in voltage, pass through an amplifier, and then are collected with the help of a data acquisition card (Daqboard 2000). Then, they are converted in distance units (mm), with the aid of a computer.

The proximity sensors have a thread so they can be adjusted on appropriate bases that allow them to be close to the shaft. After the adjustment, the proximity sensors can be positioned vertically, horizontally, or at an angle of $45^{o}$, as shown in Figure 45.

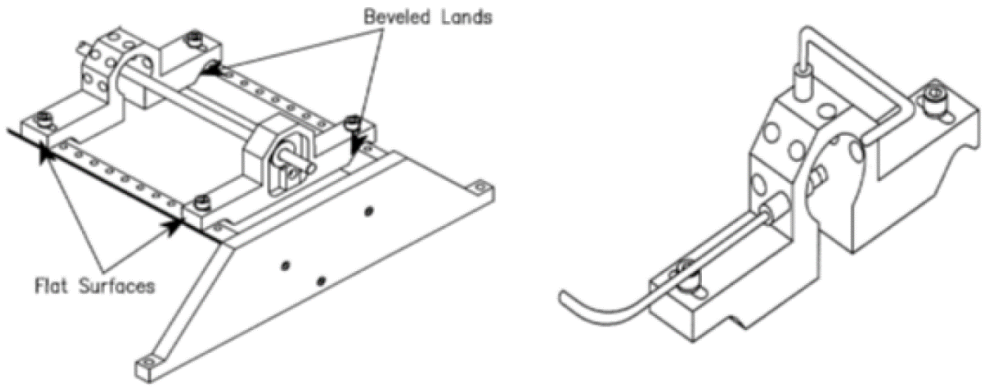


**Figure 45: Sketch of the proximity sensor brackets.**

After the assembly of the proximity sensors and the bracket, a volt-meter is used in order to measure the distance between the proximity sensors and the shaft.

**Figure 46: Proximity sensor tip.**

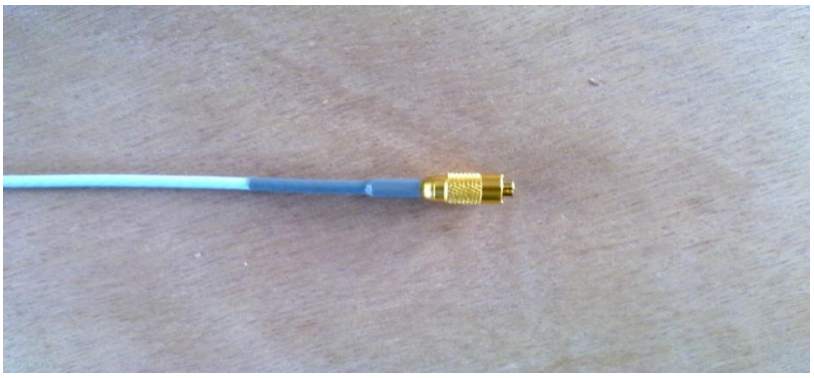

**Figure 47: Cable output of proximity sensors: outer diameter of 7.23 mm.**

Finally a drawing of the proximity sensor tip is shown in Figure 48.

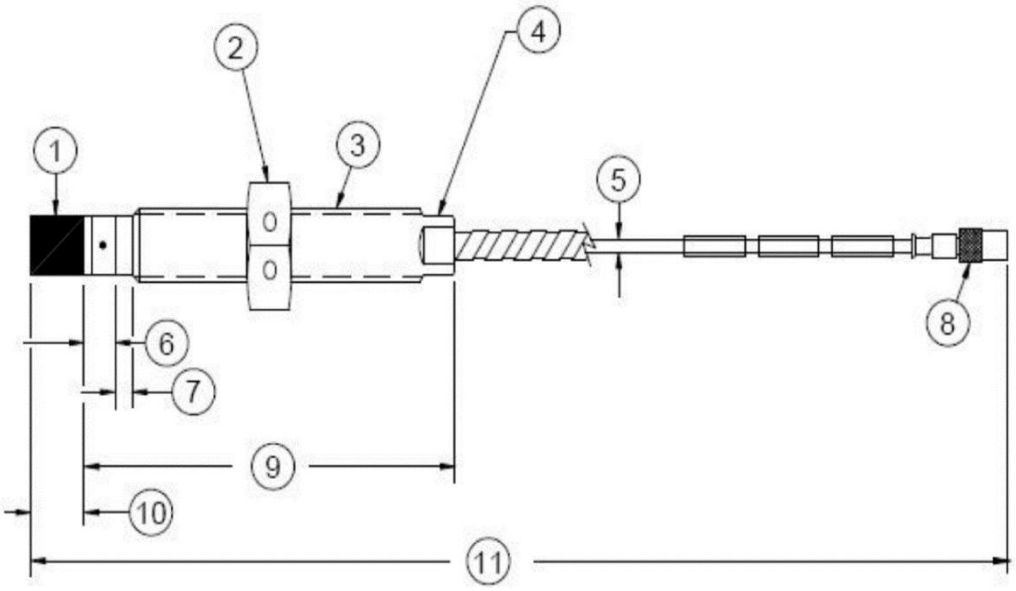


**Figure 48: Drawing of the proximity sensor tip.**

1. Probe tip, diameter: 5.26 mm
2. Hex nut
3. Cover thread
4. Sectional narrowing
5. Cable (maximum inner diameter: 2.8mm, maximum inner diameter along with the casing: 7.6 mm)
6. End cover, dimension: 3.23 mm
7. Threadless cover length
8. Coaxial connection (male), maximum outer diameter of 7.23mm
9. Cover length: 35.3 mm
10. Sensor tip length: 2.92 mm
11. Total length without cable: 43.8 mm

### 4.3.5 Pressure sensor

The pressure sensors that are used are WIKA, type A10. Their features are shown below:

*Range*: 0 to 100 bar

*Resolution*: +/- 1% of the measuring range


**Figure 49: WIKA type A10 pressure sensor.**

### 4.3.6 Temperature sensor

The temperature sensor that is used is the EGT K type thermocouple, which comes with a M5 thread. It has the following features:

- Operating temperature of -100 to 1250 $^{O}C$
- Probe diameter: 2mm
- Probe length: 10mm
- Thread size: M5
- Cable length: 2m
- Probe Material: Stainless Steel
- Cable external shielding: Stainless Steel Braiding
- Cable internal insulation: Fiberglass
- Type: Grounded
- Connector: Mini K Type Connector

**Figure 50: EGT K type thermocouple.**

### 4.3.7 IR Thermography camera DiaCam C.A. 1882

Apart from measuring the lubricating film temperature inside the bearing with conventional thermometers, an IR Thermography camera is also used, in order to accurately measure the temperature of the lubricating oil in the oil reservoir, the piping and also the temperature on the bearing housing surface. The IR Thermography camera DiaCam C.A. 1882 used in the present study takes photos, which are color-coded, depicting the spatial variation of temperature. The thermal camera comes with a specific software, which may be used to post-process the taken snapshots. With the software, the maximum and minimum temperature are shown with accurate values on the screen. Also when the cursor moves over each point of the IR photo, the exact temperature value of that point is shown. Therefore, using the IR Thermography camera enables a more detailed approach of the temperature profile for both the oil and the test rig parts. The IR Thermography camera is shown in Figure 24Figure 51.

**Figure 51: IR Thermography camera.**

### 4.3.8 Ball bearing SN507

The ball bearing SN507 consists of a pillow block that contains a ball bearing, an adapter sleeve and a locking washer, as shown in Figure 52. The pillow block material is cast iron.

**Figure 52: Ball bearing SN507.**

### 4.3.9 Drill, taps and thread construction

Whenever a need to create new holes in some of the items of the experimental setup came up, the drill that is located on the laboratory workbench was used, as shown in Figure 53. First of all, the location of the hole was measured on the item and was marked using a pencil and then with the use of a guide, a hole was opened. After that, the guide was removed and the drill took its place, in order for the hole to be fully opened at the desired dimensions. The guide and the drill are shown in Figure 54.

**Figure 53: Drill located and stationed on the workbench.**

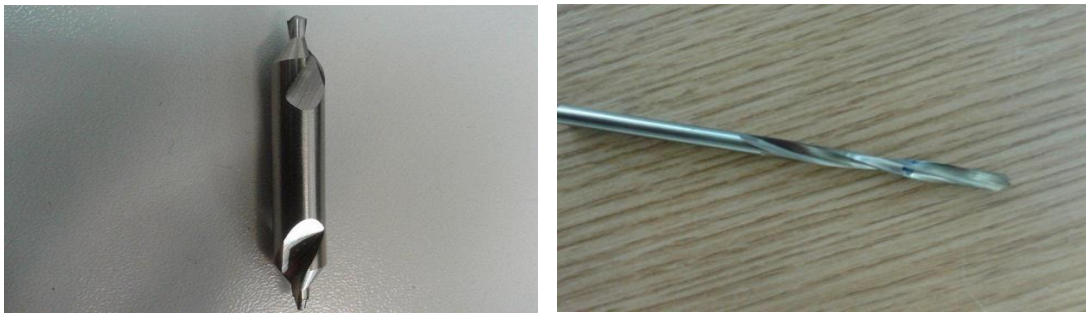

**Figure 54: The guide used for the initial opening of the hole (left), and the drill used for the permanent opening (right).**

Some of the holes were threaded. For this procedure, the hole was opened as described, and then the thread was created with the use of a tap. The tap came with three different parts in order for the thread to be fully functional. The first step after the hole was opened was to use the sharper of the three taps for the creation of a first thread that was the final one. After that the second tap was used in order to create a thread closer to the real one and finally the third tap, which was the bluntest one, was used to create the desired thread. All taps had to be inserted vertically in the hole so that the thread would be fully functional afterwards.

**Figure 55: Taps used for M5 threads.**

# 5 Experimental measurements

## 5.1 Test rig assembly

Before the experimental measurements, it is necessary to properly connect the test rig and the auxiliary items, the computer where the measurements will be collected and the lubricating system. In sections 4.2 and 4.3 there has been a description of the test rig and its auxiliary items. Because at the time of the experimental measurements, the load sensor was not usable, the autonomous setup of the test rig that was used, which consists of all four parts as they are described in section 4.2.1. The measurements of the present section were taken utilizing the torque meterTH-100, which is connected directly to the tribometer.

The first step is to connect all of the test rig items as it has been explained in section 4.2.1. Then, before initiating the experimental procedures, the lubricating system must be examined, to avoid leakage or existence of air bubbles in the piping system, which resulting in pressure loss of the lubricant. So with the electric motor switched off, the pump is set to use, sending lubricant oil in the bearing. This way, apart from detection of faults of the lubricating system, pressurized lubricant oil is inserted between the bearing and the shaft, creating a first lubricating film that will help the shaft to rotate in the bearing without being in dry state and thus damaging its surface.

After the lubricating system is checked and made sure that is without any faults, the electric motor must be prepared to run, as it has been described in section 4.1.3. The rotor is then set to a low rotational speed, while the pump is working, in order for the lubricating oil to create the hydrodynamic film between the surfaces of the bearing and the shaft. The final step is to apply the load under which the measurement will take place and set the desired rotational speed of the shaft.

When all of the above actions are completed, the test rig is ready for experimental measurements, with the use of the UMT tribometer and the torque meter TH-100. The toque meter has been modified, so that when it is mounted on the UMT tribometer, its output is not measured in volt, but instead the output is in N·mm. The measurements of friction force and friction torque are shown in live panels, and are saved in text files for further processing.

The UMT Software should be started following some certain steps, which are the following:

1. Turn on PC
2. Turn on UMT
3. Start Software
4. Load the correct option file for the desired type of measurement. In the options tab, the load options file tab is selected and then the Rotary-

DHF-100-Tz.opt file is selected, as shown in Figure 56. This is necessary in order for the UMT Tribometer to measure the friction torque through the TH-100 torque sensor, something that is possible when the rotary drive is mounted on the UMT Tribometer. So the rotary drive is connected to the UMT Tribometer before any measurements.

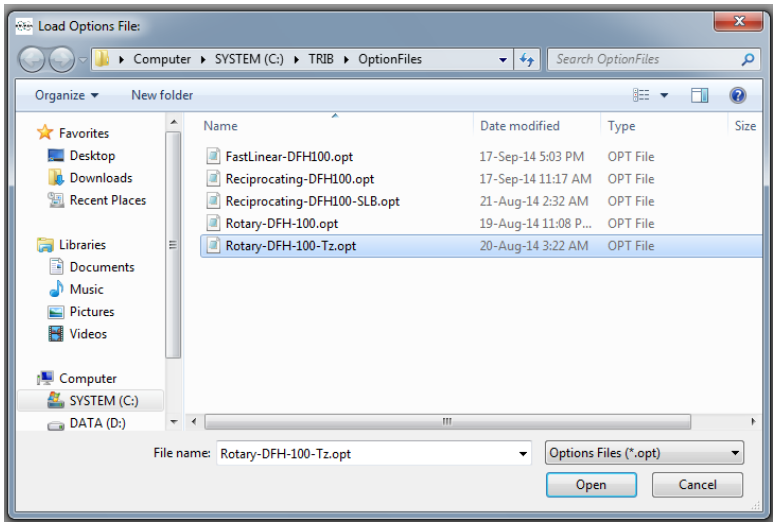


**Figure 56: Load file selection.**

5. Start the live panels. Usually the graphs for Fz/Tz are selected and opened. Because in this case the load sensor will not be connected to the tribometer, the Tz graph is selected and opened.

6. Check of force/torque sensor and zero the channels. After the measured value from the torque sensor that is displayed in the live panel has been reset to zero value, the toque sensor is checked if working properly, as shown in Figure 57. The same action would take place with the Fz live plane, if the load sensor was mounted on the UMT Tribometer.

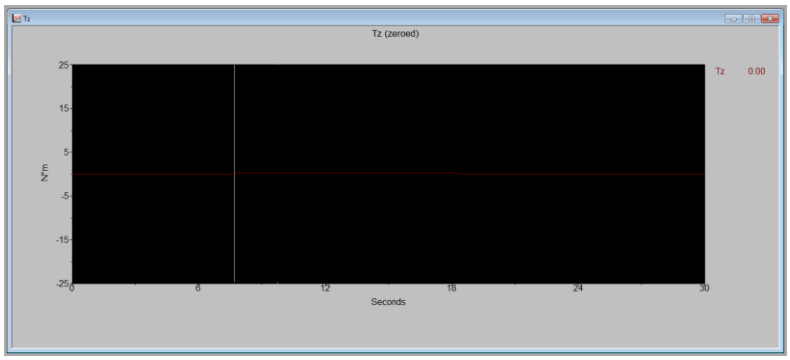


**Figure 57: Tz live panel.**

7. The next step is to create a new sequence in order to define the measurement parameters. The new sequence panel with the alongside tabs is shown in Figure 58. The engage tab remains at its default values, and it shows the force, which the UMT Tribometer will apply to the

rotary drive. This step is more general and in this case it will not be of any use as the load will be applied without the use of the UMT Tribometer. The same applies for the disengage tab: the default values are left and it will have not any further effect in this case. Those two tabs should be of use when the load is applied through the UMT Tribometer with the use of the load sensor DHF-100.

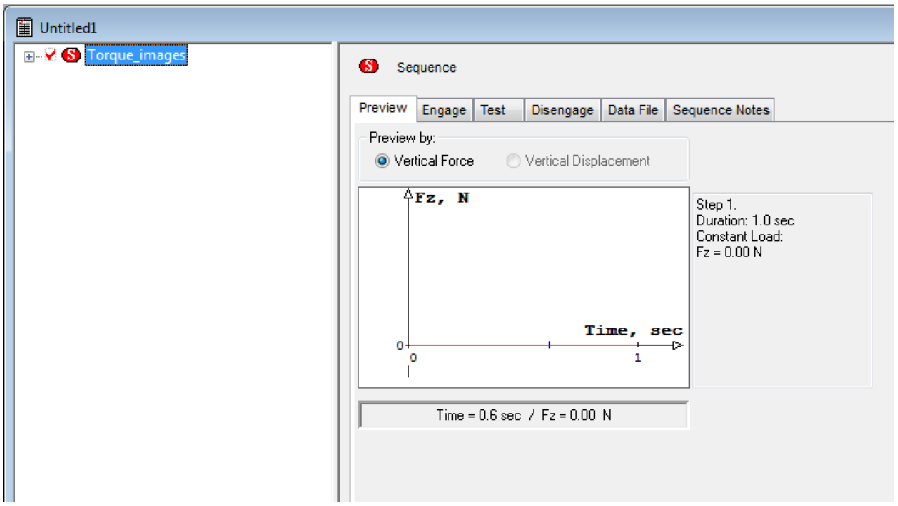


**Figure 58: New sequence panel.**

In the Data File tab, the Create Data File option is selected with the channels and the amount of samples. In the channels tab, the live panels are selected that correspond to the measurement method that will take place. If both the load and the torque sensors are used, then both the Fz and Tz channels are selected, as shown in Figure 59. However, for the measurements of the present section, only the Tz channel has been selected.

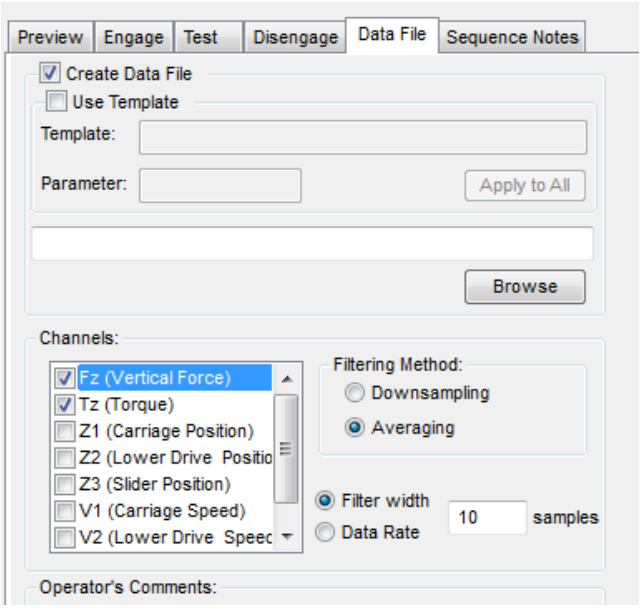


**Figure 59: Data file tab.**

8. After having completed the general sequence options, the first step of the sequence must be created. It should be noted that the first step of the sequence coincides with the engagement step. The 4 tabs of the new sequence panel are presented in Figure 60. Under normal operating conditions of the UMT tool, the most common way to exploit the feedback-control feature of UMT is to use the neutral load, which is permanently monitored by the force sensor. Since the force sensor has malfunctioned, those options were put to idle, and the only contribution of UMT was to act as receiver of the torque meter signal and translating into frictional torque $(\mathrm{N} \cdot m)$. A typical duration of an experimental sequence has been selected equal to 30 s for all the measurement tests.

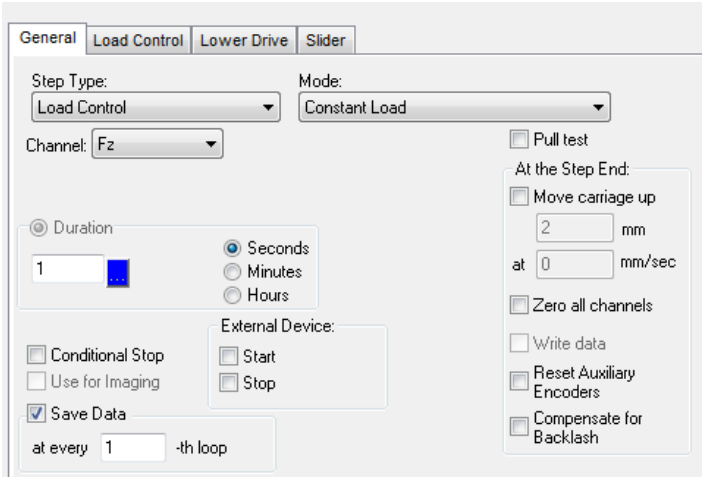


**Figure 60: General first step panel.**

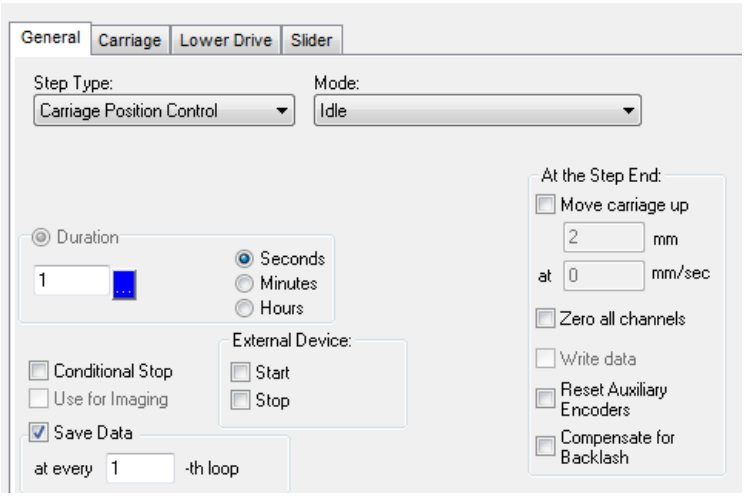


**Figure 61: First step panel for the torque sensor.**

9. The last step is to check the created script. This option examines if all of the selected options are set correctly, and that a functioning measurement script for the UMT Tribometer has been created. If the check is successful, the script can be started in order for the

measurement to take place, and all the measured parameters to be saved to the appropriate files. These two tabs are shown in Figure 62.

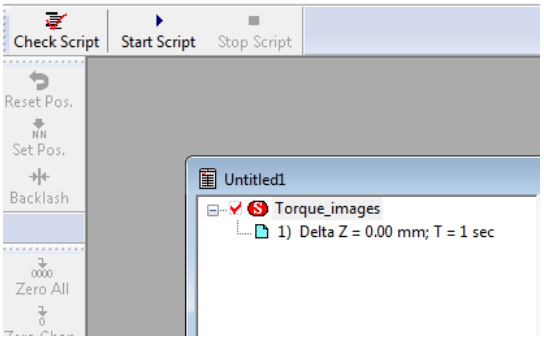


**Figure 62: Check script and Start Script options.**

The created files that contain the measurements are saved in *.csv* files that can be opened by Microsoft Excel for further processing. An image of the test rig when all parts are assembled is shown in Figure 63.

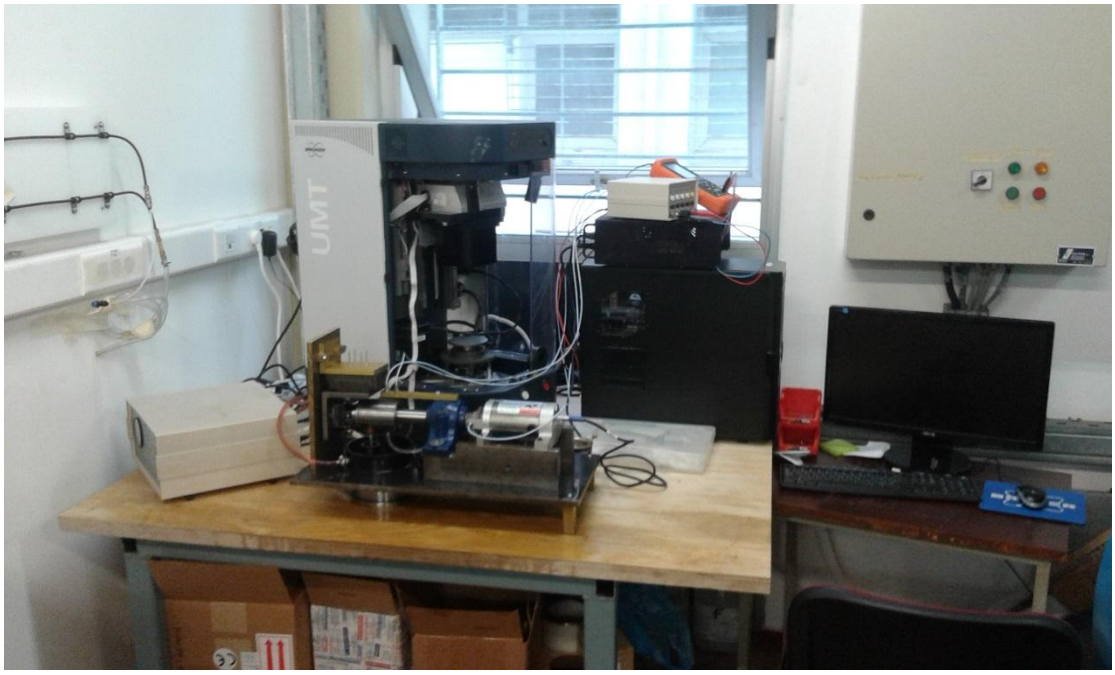


**Figure 63: Test rig with all parts connected.**

## 5.2 Experimental results

### 5.2.1 Plain journal bearings

A series of experimental measurements took place on the test rig. A static load has been applied to the bearing, corresponding to the weight of parts 1, 2, 3, 4, 5, 6 and 21 as they have been described in 4.2.1. The weight of each part is shown in Table 26.

**Table 26: Total weight of items for first measurement of friction torque**

| Item | Item number |
|---|---|
| Rail for z motion upper part | 1 |
| Rail for z motion lower part | 2 |
| L part | 3 |
| Torque sensor type TH-100 | 4 |
| Bearing housing flange | 5 |
| Bearing housing | 6 |
| Slider | 21 |
| Total weight (kg) | 6.097 |

The total weight of 6.097 kg equals to 59.79 N of applied load. The tested bearing was a copper bearing; its geometric characteristics have been presented in Table 2 in section 3.1. Eight different experiments were conducted, for different values of the rotational speed of the shaft, varying from 600 RPM to 2000 RPM. In Table 27 and Figure 65, measurements of friction torque are presented for all the studied cases. Additionally, oil temperature was measured using the IR Thermography camera described in 4.3.7. A characteristic photo of the IR Thermography camera software displaying the bearing housing and the lubricant oil in the oil reservoir and the feeding oil temperatures using the IR Thermography camera software is shown in Figure 64, where the displayed items on screen come with their referenced number.

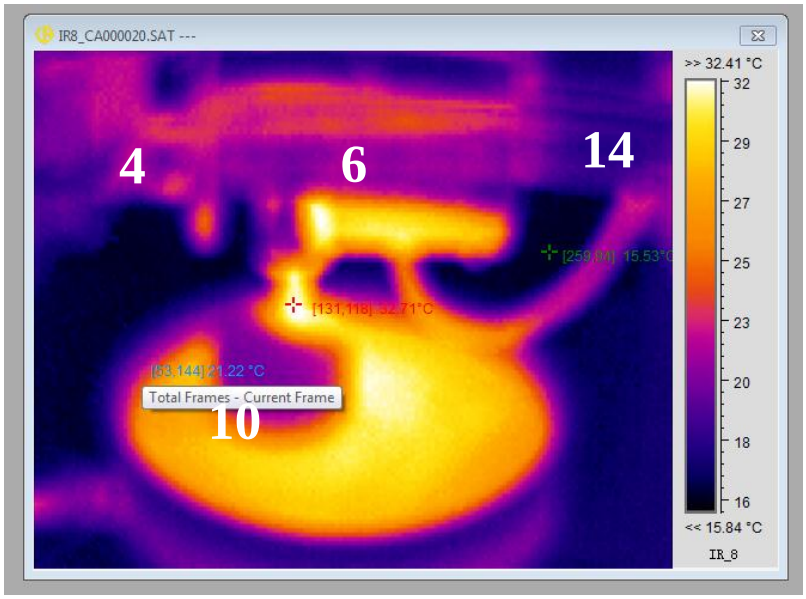


**Figure 64: IR Thermography camera software: snapshot captured during bearing operation**

.

**Table 27: Friction torque measurements in a copper bearing for different rotational speeds of the shaft.**

| Rotational speed (RPM) | $p_{pump}$ (bar above atmospheric) | $T_z$ (N·m) | $T_{oil}$ (ºC) |
|---|---|---|---|
| 600 | 3 | -0,03983 | 32 |
| 800 | 2,8 | -0,05436 | 34 |
| 1000 | 2,8 | -0,06294 | 35 |
| 1200 | 2,8 | -0,07366 | 36 |
| 1400 | 2,8 | -0,07458 | 36 |
| 1600 | 2,8 | -0,08153 | 36 |
| 1800 | 2,8 | -0,08896 | 37 |
| 2000 | 2,8 | -0,09467 | 39 |

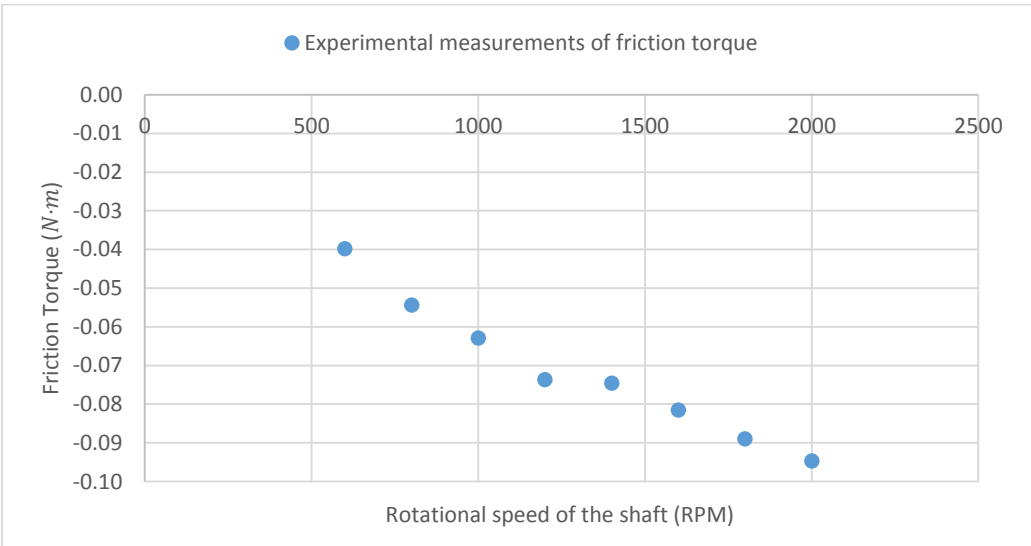


**Figure 65: Experimental measurements of friction torque in the copper plain bearing.**

## 5.3 Reference measurements – comparison with numerical simulations

The experimental measurements that were performed with the use of the test rig showed that friction torque increases in absolute value when the rotational speed of the shaft increases under steady applied load, as showed in Figure 65. These result can validate the numerical analysis data for the plain journal bearing shown in Table 28, which showed a similar trend.

**Table 28: Friction torque in a copper bearing: comparison between experimental measurements and numerical simulations.**

| Rotational speed (RPM) | $p_{pump}$ (bar above atmospheric) | $T_z$ experimental (N·m) | $T_z$ numerical (N·m) | $\Delta T_z$ (%) | $T_{oil}$ |
|---|---|---|---|---|---|
| 600 | 3 | -0,03983 | -0,03840 | 3,59 | 32 |
| 800 | 2,8 | -0,05436 | -0,04822 | 11,28 | 34 |
| 1000 | 2,8 | -0,06294 | -0,05708 | 9,30 | 35 |
| 1200 | 2,8 | -0,07366 | -0,06504 | 11,70 | 36 |
| 1400 | 2,8 | -0,07458 | -0,07219 | 3,20 | 36 |
| 1600 | 2,8 | -0,08153 | -0,08637 | -5,94 | 36 |
| 1800 | 2,8 | -0,08896 | -0,08735 | 1,81 | 37 |
| 2000 | 2,8 | -0,09467 | -0,09360 | 1,13 | 39 |

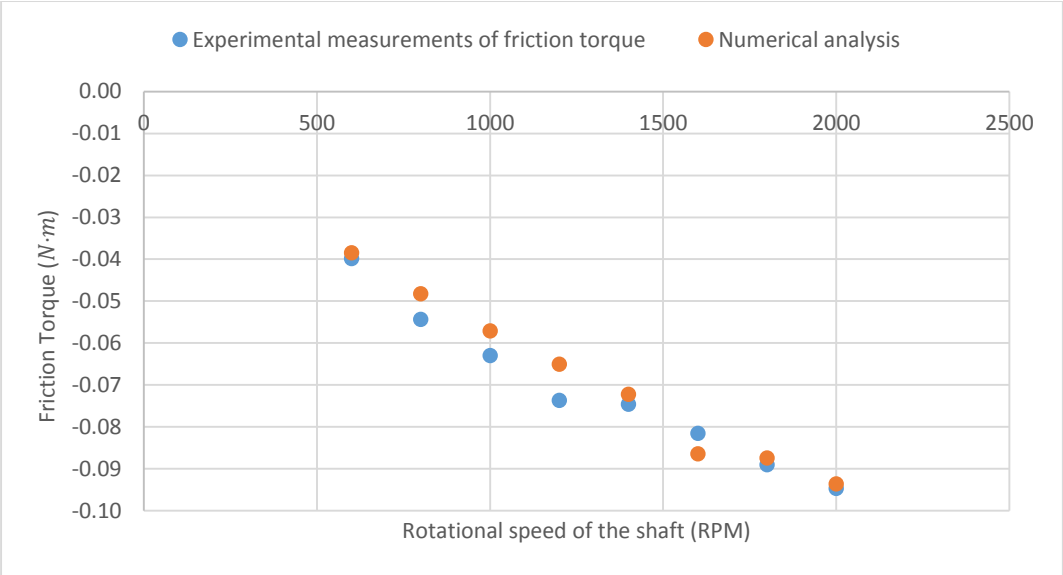


**Figure 66 : Friction torque in a copper bearing: comparison between experimental measurement and numerical simulations.**

Figure 66 shows that experimental and numerical analysis have small difference in their values, especially in high rotational speeds. Table 28 shows the difference percentage for friction torque measurements for both experimental and numerical analysis. The average percentage in difference is 4.5%.

# 6 Conclusions and future work

## 6.1 Conclusions

In the present Diploma Thesis, a computational and experimental study of hydrodynamically lubricated journal bearings has been performed. The aim of the present study was twofold: (a) to investigate the possibility of performance improvement by introduction of artificial surface texturing or hydrophobicity at part of the bearing surface, and (b) to design and construct a test-rig for journal bearing performance measurements.

First, a computational investigation of hydrodynamic lubrication in journal bearings exhibiting different types of surface treatment at part of the bearing surface has been performed. Bearing performance was computed by solution of the Reynolds equation, utilizing an in-house finite difference solver. Five different types of journal bearings were cross-evaluated for operation under different combinations of radial load and rotational speed: (a) a pocket bearing, (b) a bearing with circumferential grooves, (c) a bearing with axial grooves, (d) a bearing with rectangular texturing, and (e) a hydrophobic bearing. The most efficient designs for each bearing type were identified with the aid of a multi-objective optimization approach, based on the Matlab optimization toolbox. The optimization goal was to identify the main bearing design parameters (texture depth, axial/circumferential texture extents, slip length, axial/circumferential hydrophobic extents) which simultaneously minimize friction coefficient and maximize minimum lubricant thickness. In particular, the optimization process was repeated for bearings with different artificial surface texturing designs (T,1,1, T,5,1, T,1,5, T,5,5, see Table 12 for name conventions), and for bearings with hydrophobic surfaces, characterized by different values of slip length (designs H,1, H,0.1, see Table 13 for name conventions). The applied load was varied between 200 N and 1000 N, while the rotational speed of the shaft was set at 500 RPM or 1000 RPM. The results of the numerical analysis have shown that a noteworthy improvement of bearing performance is feasible if artificial surface texturing / hydrophobicity is introduced at appropriate parts of the bearing surface. Maximum performance improvement, in terms of the normalized friction coefficient and the dimensionless eccentricity ratio, were observed for rotational speed of 1000 RPM and applied load of 200 N, both for artificial surface textured and hydrophobic bearings.

Next, an experimental journal bearing test-rig was designed and constructed. The test-rig can either act as a stand-alone setup or it can be connected to an existing UMT Tribometer facility of NTUA, and is capable of measuring different performance parameters of a journal bearing, including eccentricity/attitude angle, friction torque, pressure and temperature of the lubricant film at different bearing locations, as well as shaft/bearing misalignment. Experimental measurements were performed for plain copper journal bearings, and the obtained results were compared with computational results of the present study.

## 6.2 Future work

Future work, in continuation of the present, could include:

- Additional experiments with the experimental test-rig for validating (a) the measurements of the developed pressure and temperature in the lubricating domain, (b) the measurements of eccentricity and attitude angle, and (c) the measurements of the shaft/bearing misalignment angle.
- Additional experiments on journal bearings modified properly with artificial surface texturing or hydrophobicity.
- Experiments on journal bearings made of different materials, and comparison of their performance, under different combinations of applied loads and rotational speeds.
- Connection of the test-rig with the UMT tribometer, and conduction of experimental measurements on bearings under transient load.

# 7 Literature


[1] Stachowiak G. W., "Meaning of Tribology," in Engineering Tribology, University of Western Australia,Department of Mechanical and Materials Engineering, Australia, Butterworth Heinemann, pp. 2-9, 126-140.

[2] Khonsari M. M. and Booser R. E., "Applied Tribology," in Applied Tribology: Bearing Design and Lubrication, Second Edition, John Wiley & Sons, Ltd, 2008, p. chapter 8: Journal Bearings.

[3] Brito F. P., Miranda A. S., Claro J. C. P. and Fillon M., "Experimental comparison of the performance of a journal bearing with a single and a twin axial groove configuration".

[4] Adatepe H., Biyiklioglu A. and Sofuoglu H., «An experimental investigation on frictional behaviour of statically loaded micro-grooved journal bearing,» *Tribology International 44,* pp. 1942-1948, 2011.

[5] Dadouche and Conlon M. J., "Operational performance of textured journal bearings lubricated with a contaminated fluid".

[6] Tala-Ighil N., Fillon M. and Maspeyrot P., "Effect of textured area on the performances of a hydrodynamic journal bearing," Tribology International 44, pp. 211-219, 2011.

[7] Ibatan T., Uddin M.S., Chowdhury M.A.K., “Recent development on surface texturing in enhancing tribological performance of bearing sliders, ” Elsevier, January 2015, p. 102-120

[8] Mingfeng Q., Minson B. R. and Raeymaekers B., "The effect of texture shape on the friction coefficient and stiffness of gas-lubricated parallel slider bearings," Tribology International 67, pp. 278-288, 2013.

[9] Meng F. M., Zhang L., Liu Y. and Li T. T., "Effect of compound dimple on tribological performances of journal bearing," Tribology International 91, pp. 99-110, 2015.

[10] Ahmada M. A., Kasolang S. and Dwyer-Joyce R., "The effects of oil supply pressure at different groove position on frictional force and torque in journal bearing lubrication," Procedia Engineering 68, pp. 70-76, 2013.

[11] "Test rig for journal bearings," Gdansk Univesristy of Technology Faculty of Mechanical Engineering Machine Design and Maintenace Department, pp. PG-II 1L.

[12] Durak E., Kurbanogˇlu C., Bıyıklıogˇlu A. and Kaleli H., "Measurement of friction force and effects of oil fortifier in engine journal bearings under dynamic loading conditions," Tribology International 36, pp. 599-607, 2003.

[13] Sander D. E., Allmaier H., Priebsch H. H., Reich F. M., Witt M., Füllenbach T., Skiadas A., Brouwer L. and Schwarze H., "Impact of high pressure and shear thinning on journal bearing friction," Triobology International 81, pp. 29-37, 2015.

[14] Zhang H., Hua M., Dong G.-n., Zhang D.-y. and Chin K.-s., "Boundary slip surface design for high speed water lubricated journal bearings," Tribology International 79, pp. 32-41, 2014.

[15] Pochylý, Fialová S. and Kozubková M., "Journal bearings with hydrophobic surface," Procedia Engineering 39, pp. 76-83, 2012.

[16] Rao T. V. V. L. N., Rani A. M. A., Nagarajan T. and Hashim F. M., "Analysis of slider and journal bearing using partially textured slip surface," Tribology International 56, pp. 121-128, 2012.

[17] Κωστόπουλος Θ. Ν., "Οδοντώσεις και Μειωτήρες Στροφών," Αθήνα, Εκδόσεις Συμεών, 2010, pp. 429-458.

[18] Koukoulopoulos E., “Software development for the solution of hydrodynamic lubrication problems in piston rings of two-stroke marine Diesel engines,” Athens: NTUA, 2014.

[19] Zouzoulas V., “Thermodynamic analysis of tilting pad thrust bearings with artificial surface texturing,” Athens: NTUA, 2014.

[20] Raptis L., “Software development for the solution of hydrodynamic lubrication problems in main bearings of marine Diesel engines,” Athens: NTUA, 2014.

[21] Rahmani R., Shirvani A. and Shirvani H., "Optimized textured surfaces with application in piston-ring/cylinder liner contact," in Tribology and dynamics of engine and powertrain: Fundamentals, applications and future trends, Cambridge, Woodhead Puplishing, 2010, pp. 470-517.

[22] Ajith, Lakhmi J. and Goldberg R., in Evolutionary multiobjective optimization, London, Springer, 2005, pp. 1-6.

[23] Bodenhofer U., "Genetic Algorithms: Theory and Applications," Fuzzy.Logic.Lab.Linz, 2004, pp. 12-24.

[24] Marseguerra M. and Zio E., "Genetic algorithms: Theory and applications in the safety domain," Trieste, 200, pp. 657-670.

[25] Papadopoulos C. I., Nikolakopoulos P. G. and Kaiktsis L., "Evolutionary optimization of micro-thrust bearings with periodic partial trapezoidal surface texturing," Journal of Engineering for Gas Turbines and Power, vol. 133, 2011.

[26] Papadopoulos C. I., Nikolakopoulos P. G. and Kaiktsis L., "Elastohydrodynamic analysis and Pareto optimization of intact, worn and misaligned journal bearings," Meccanica, vol. 46, pp. 577-588, 2011.

[27] Papadopoulos C. I., Efstathiou E. E., Nikolakopoulos P. G. and Kaiktsis L., "Geometry optimization of textured three-dimensional micro-thrust bearings," Journal of Tribology, vol. 133, 2011.

[28] Pavlioglou S. K., Mastrokalos M. E., Papadopoulos C. I. and Kaiktsis L., "Tribological optimization of thrust bearings operated with lubricants of spatially varying viscosity," Journal of Engineering for Gas Turbines and Power, vol. 137, 2015.

[29] Σταματελόπουλος Δ., “Πειραματική μελέτη υδροδυναμικής λίπανσης σε ακτινικά έδρανα,” Athens: NTUA, 2013

[30] Brian Griffiths, “Manufacturing engineering modular series: Engineering drawing for manufacture,” Kogan Page Science, 2003, p. 1-21.

[31] Rahmani R., Mirzaee I., Shirvani A., Shirvani H., “ An analytical approach for analysis and optimization of slider bearings with infinite width parallel textures,”, Tribology International 2010, vol. 43, p. 1551-1565

# Appendix A

## Principles of drawings

According to Brian Griffiths [30] the main purpose of engineering drawings is to communicate information by providing a specification. Therefore engineering drawings need to meet the following requirements:

- They should be unambiguous and clear. So for there has to be only one interpretation for any part of a component.
- They should provide all the information needed, thus engineering drawings need to be complete. However, a drawing may rely to other drawings to provide all the necessary information for a component.
- The drawing should be suitable for duplication, without any information being loss through the process.
- Drawings should communicate their content, without the use of any language, meaning they should be language-independent. The only case for using language is the title of the drawing or where information of non-graphical form should be given.
- Engineering drawings need to conform to standards, with the highest standard being the ISO ones, which are applied worldwide.

## Layout of drawings

The blank sheet of a drawing should contain the following things. It has to be noted that the first three things are mandatory and have to be included in every blank sheet, where the last four are optional.

1. Title block
2. Frame for limiting the drawing space
3. Centring marks
4. Orientation marks
5. Metric reference graduation
6. Grid reference system
7. Trimming marks

The title block is usually located in the bottom right-hand corner of the drawing and contains information, from very simple to very complex that help identification of the drawing.

The frame for limiting the drawing space is called border. It shows the drawing region, by defining its edges.

Centring marks take the form of dashes and are found on the center of each of the four sides of the border. They are used to help with the positioning of the drawing.

Orientation marks are consisted of arrows that coincide with the centring marks and are positioned on two of the four sides of the border, with one of them pointing toward the position of the draughtsman.

A metric reference graduation scale uses a minimum length of 100 mm with 10 mm intervals. It is used in order to enable the scaling of the drawing when the scale is different than the original.

A grid reference system should be used in every drawing as it enables the easy finding of details, additions and modifications.

Trimming marks are positioned at the four corners of the drawing sheet, one in each corner. They are used in order to help with the trimming of the paper.

All of the above layout parts are shown in Figure 67.

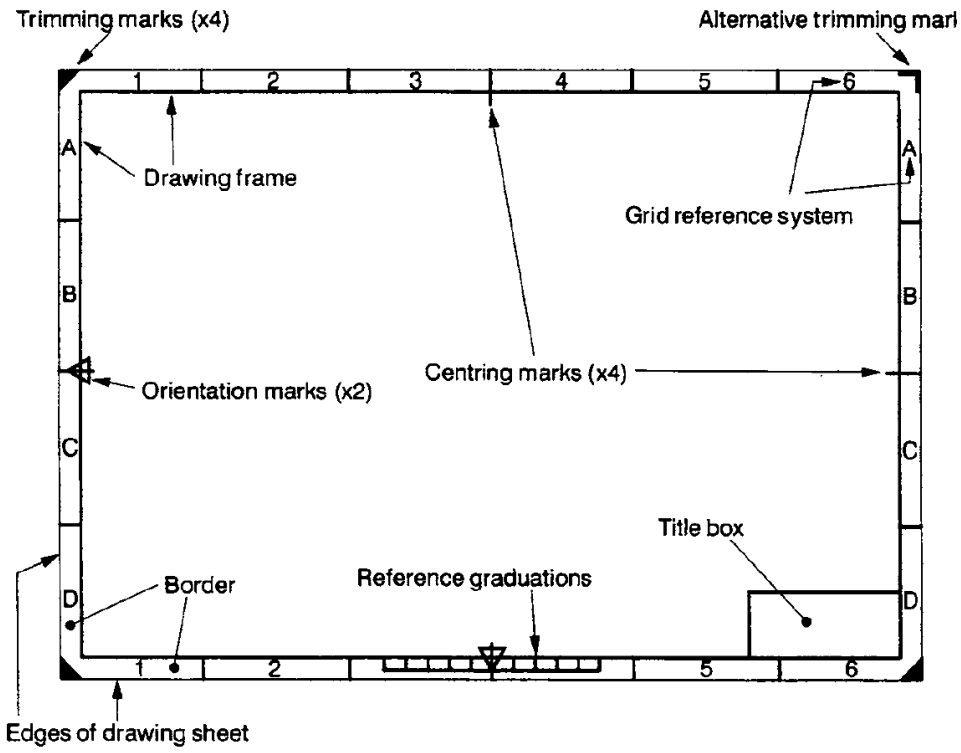


**Figure 67: Layout of drawing sheets**

The type of drawings that were used to show the test rig parts are the following:

- Detail drawings that show the details of a single component, including all the necessary information required for its manufacture.
- Assembly drawings that show how the individual parts are combined together in order to make the assembly.

Also it should be mentioned that all drawings are created using the European ISO for their presentation.